

Hydrodynamic Investigations of Rapidly Stretched Liquid Bridges

Vom Fachbereich Maschinenbau
an der Technischen Universität Darmstadt
zur
Erlangung des Grades eines Doktor-Ingenieurs (Dr.-Ing.)
genehmigte

Dissertation

vorgelegt von

Sebastian Brulin, M.Sc.

aus Bad Soden-Salmünster

Berichterstatter: Apl. Prof. Dr.-Ing. Ilia V. Roisman
Mitberichterstatter: Prof. Dr.-Ing. Jeanette Hussong
 Prof. Dr.-Ing. Edgar Dörsam

Tag der Einreichung: 13.10.2020
Tag der mündlichen Prüfung: 16.12.2020

Darmstadt 2020
D17 (Diss. Darmstadt)

Sebastian Brulin:
Hydrodynamic Investigations of Rapidly Stretched Liquid Bridges
Darmstadt, Technische Universität Darmstadt

Jahr der Veröffentlichung der Dissertation auf TUpriints: 2021
URN: <https://tuprints.ulb.tu-darmstadt.de/id/eprint/17537>
Tag der mündlichen Prüfung: 16.12.2020
Veröffentlicht unter CC BY-SA 4.0 International



Hiermit versichere ich, die vorliegende Doktorarbeit unter der Betreuung von Apl. Prof. Dr.-Ing. I.V. Roisman und Prof. Dr.-Ing. J. Hussong nur mit den angegebenen Hilfsmitteln selbständig angefertigt zu haben.



Darmstadt, den 08. Oktober 2020

Abstract

Liquid bridges have become an integral part of many industrial processes relevant to consumer production. For example, the coating technology often includes dip-coating, printing, or spraying of liquid materials. Liquid bridge or liquid jet fast stretching is an essential element of such processes. Bridge stretching determines the outcome of liquid atomization and the agglomeration of wet particles. Moreover, liquid bridge stretching is used for the rheological characterization of complex liquids.

This thesis deals with the investigation of fast stretched Newtonian fluid bridges. The unique feature of this study is the investigation of particularly high stretching rates for very small liquid bridge heights. A system consisting of two parallel substrates was developed. One substrate can be moved with a constant, controllable acceleration while the other substrate remains stationary. It allows performing parameter studies with accelerations of up to 180 m/s^2 and initial bridge heights starting from $50 \mu\text{m}$.

Extensive experimental and theoretical studies were carried out to identify the most influencing parameters and, therefore, to understand the physical mechanisms of the observed phenomena better. The characterization includes a description of the kinematics of the liquid bridge stretching and different outcomes like liquid cavitation, finger formation during stretching, and bridge pinch-off.

The evolution of the main geometrical properties of the stretching liquid bridge is characterized. These properties include the curvature and shape of the meniscus, length, and diameter of the liquid bridge. Two main regimes of a fast stretching are identified: viscous regime, determined by the Reynolds number, and capillary regime for low viscosity liquids, governed by the Weber number. The knowledge of the kinematics of the bridge allows us to determine the appropriate scales for a description of the stretching outcomes.

The cavitation phenomena are described using the estimation of the

distribution of the viscous pressure in the gap. This pressure determines the evolution of the cavity radius. A bubble growth model has been developed, which allows the prediction of the instant of the maximum bubble diameter as a function of the cavitation inception rather well. Next, the stability analysis of the bridge free interface is performed, which accounts for the viscous effects and inertia. The predicted condition for the appearance of the fingers and the number of these fingers agree well with the experimental data. Finally, the model for the pinch-off time of the stretching bridge is developed. The scales for the pinch-off time have been determined for viscous and for the capillary stretching regimes.

The experimental and theoretical results can be potentially useful for optimizing the operational conditions during printing and modeling atomization, accretion, and agglomeration phenomena.

Kurzfassung

Flüssigkeitsbrücken sind zu einem integralen Bestandteil vieler industrieller Prozesse in der Konsumgüterproduktion geworden. So umfasst zum Beispiel die Beschichtungstechnologie oftmals die Prozesse des Tauchbeschichtens, des Druckens oder des Zerstäubens von flüssigen Materialien. Die schnelle Dehnung von Flüssigkeitsbrücken oder Flüssigkeitsstrahlen sind zentrale Mechanismen dieser Prozesse. Die Flüssigkeitsbrückendehnung bestimmt dabei das Ergebnis der Flüssigkeitszerstäubung und der Agglomeration von feuchten Partikeln. Darüber hinaus wird die Flüssigkeitsbrückendehnung für die Charakterisierung rheologisch komplexer Flüssigkeiten verwendet.

Diese Arbeit befasst sich mit der Untersuchung schnell gestreckter Newtonscher Flüssigkeitsbrücken. Die Besonderheit dieser Studie ist die Untersuchung sehr hoher Dehnungsraten bei sehr kleinen Flüssigkeitsbrücken. Ein Substrat kann mit einer konstanten, kontrollierbaren Beschleunigung bewegt werden, während das andere Substrat stationär bleibt. Damit wird die Durchführung von Parameterstudien mit Substratbeschleunigungen von bis zu 180 m/s^2 und initialen Brückenhöhen ab $50 \mu\text{m}$ ermöglicht.

Es wurden umfangreiche experimentelle und theoretische Studien durchgeführt, um die wichtigsten Einflussparameter zu identifizieren und somit die physikalischen Mechanismen der beobachteten Phänomene besser zu verstehen. Die Charakterisierung umfasst die Beschreibung der Kinetik der Flüssigkeitsbrückendehnung und weiterer auftretender Phänomene wie: Kavitation, Fingerbildung und Aufbruch der Flüssigkeitsbrücke.

Die Entwicklung der wichtigsten geometrischen Eigenschaften während der Flüssigkeitsbrückendehnung wird charakterisiert. Zu diesen Eigenschaften gehören die Krümmung und Form des Meniskus, sowie die Länge und der Durchmesser der Flüssigkeitsbrücke. Es werden zwei Hauptregime einer schnellen Dehnung identifiziert: das viskose Regime, das durch die Reynolds-Zahl bestimmt wird, und das Kapillarregime für niedrigviskose Flüssigkeiten, das durch die Weber-Zahl bestimmt wird. Die Kenntnis

der Brückenkinematik erlaubt es, die geeigneten Skalen zur Beschreibung der Dehnungsergebnisse zu identifizieren.

Die Kavitationsereignisse werden durch die Schätzung der viskosen Druckverteilung zwischen den Substraten beschrieben. Dieser Druck bestimmt die Entwicklung des Hohlraumradius. Es wurde ein Modell für das Blasenwachstum entwickelt, das es erlaubt, den Zeitpunkt des maximalen Blasendurchmessers in Abhängigkeit des Kavitationsbeginns vorherzusagen. Dazu wurde eine Stabilitätsanalyse der brückenfreien Grenzfläche durchgeführt, die die viskosen Effekte und die Trägheit berücksichtigt. Die vorhergesagte Bedingung für das Erscheinen und die Anzahl der Finger stimmen gut mit den experimentellen Daten überein. Es wurde außerdem ein Modell für die Aufbruchzeit der Flüssigkeitsbrücke entwickelt. Dabei wurden die Skalen für die Aufbruchzeit für die viskosen und für die kapillaren Dehnungsregime bestimmt.

Die experimentellen und theoretischen Ergebnisse können potenziell nützlich für die Optimierung der Betriebsbedingungen während des Druckens, aber auch für die Modellierung von Zerstäubungs-, Akkretions- und Agglomerationsphänomenen sein.

Acknowledgements

My sincere gratitude goes first and foremost to my supervisor Professor Dr.-Ing. Ilia V. Roisman, and his mentoring during the last almost four years. As an extremely competent, supportive, and positive doctoral supervisor, his professional and human supervision was the most important support for my doctoral thesis. Additionally, I would like to thank the head of the institute Professor Dr.-Ing. Jeanette Hussong and her predecessor Professor Dr.-Ing. Cameron Tropea for the confidence, the ongoing support, and the opportunity to conduct my research at the Institute for Fluid Dynamics and Aerodynamics (Fachgebiet für Strömungslehre und Aerodynamik) of the Technische Universität Darmstadt. I am very grateful for all of the inspiring discussions, which always highly motivated me. Working in this group enabled me to gain scientific and also personal experience in mastering complex problems. The unique facilities and equipment contributed in large part to this study. Furthermore, I would like to thank Professor Dr.-Ing. Edgar Dörsam for refereeing my thesis.

The financial support from the German Research Foundation (Deutsche Forschungsgemeinschaft) under grant CRC 1194 is gratefully acknowledged. Within the framework of my project, I had the opportunity to meet many interesting people in places all over the world, which inspired me and my work. In particular, I want to mention my colleagues from the CRC 1194, especially Michael Heinz, Maximilian Hartmann, and Julian Schäfer, and from the Institute for Fluid Dynamics and Aerodynamics of the Technische Universität Darmstadt, especially Hannah Kittel, Johannes Feldmann, Fabian Tenzer, and Felix Gerlach, for many fruitful discussions and sharing of unforgettable experiences, personally and also professionally.

Special thanks go to my former study colleagues and work colleagues Hartmut Niemann, Maximilian van Eyk, Johannes Hinrichs, and Felix Zimmermann from the Technische Universität Darmstadt for all the coffee breaks, discussions during lunch, and the support that made my work-

place a second home. I would also like to thank all the students who were a great help to me, especially Tim Weber, Patrick Feifel and Sabrina Jegust.

I want to thank the administrative team, consisting of Birgit Neuthe, Corinna Neumann, and Monika Medina, and the workshop team under the direction of Ilona Kaufhold. They helped me in countless situations, and their support has made a significant contribution to this study's success.

Finally, I would like to thank my parents Monika and Josef Brulin, my brother Benedikt Brulin and my friends for their continuous support, care, and encouragement. An exceptional thank goes to Karina Druschel for the continuous positive motivation during stressful phases, the emotional support, the needed distraction, and much more during the last years.

Contents

Abstract	i
Kurzfassung	iii
Acknowledgements	v
1 Introduction	1
1.1 Motivation	1
1.2 Hydrodynamic Phenomena in a Liquid Bridge	4
1.2.1 Cavitation Phenomena	5
1.2.2 Fingering Instability of the Liquid Interfaces	7
1.2.3 Pinch-Off of a Liquid Jet	9
1.3 Thesis Outline	11
2 Experimental Methods and Procedures	13
2.1 Experimental Set-up	13
2.1.1 Stretching Apparatus	14
2.1.2 Fluid and Substrate Preparation	19
2.1.3 Observation System	27
2.2 Image Processing	30
2.2.1 Processing of Side-View Images	30
2.2.2 Processing of Top-View Images	33
3 Hydrodynamics of a Stretched Liquid Bridge	37
3.1 Phenomenological Description	37
3.2 Profile Investigation	41
3.2.1 Curvature	41
3.2.2 Centreline Profile	43
3.2.3 Meniscus Profile	45
3.3 Pressure Distribution	59
3.3.1 Pressure Field in a Creeping Flow in a Thin Gap	62
3.3.2 Pressure Distribution Accounting for the Inertia	63
3.4 Conclusion	64

4	Cavitation Phenomena During Liquid Bridge Stretching	67
4.1	Phenomenological Description	67
4.2	Discussion of the Cavitation Dynamics	71
4.2.1	Effect of the Pressure in the Gap on Cavitation	71
4.2.2	Bubble Growth	74
4.2.3	Dynamics of the Cylindrical Bubble Expansion	78
4.3	Conclusion	82
5	Fingering Instability of the Stretching Bridge	85
5.1	Phenomenological Description	85
5.2	Stability Analysis of the Bridge Interface	88
5.2.1	Long-Wave Approximation of Small Flow Perturbations on a Planar Interface	89
5.2.2	Approximation for Small Capillary Numbers	92
5.3	Results and Discussion	94
5.4	Conclusion	102
6	Pinch-Off Time	105
6.1	Dynamics of a Stretched Liquid Bridge - Short times	105
6.1.1	Governing Dimensionless Parameters	105
6.2	Dynamics of a Long Liquid Bridge and Jet - Long Times	107
6.3	Modelling the Pinch-Off Time	111
6.4	Conclusion	114
7	Conclusion and Outlook	117
	Bibliography	134
	List of Figures	143
	List of Tables	145

1 Introduction

In this chapter, the motivation for investigating liquid bridge stretching phenomena in different applicational contexts is demonstrated. A thorough review of the present state of the art on liquid stretching and associated phenomena such as cavitation, finger instability, and bridge pinch-off is given after that.

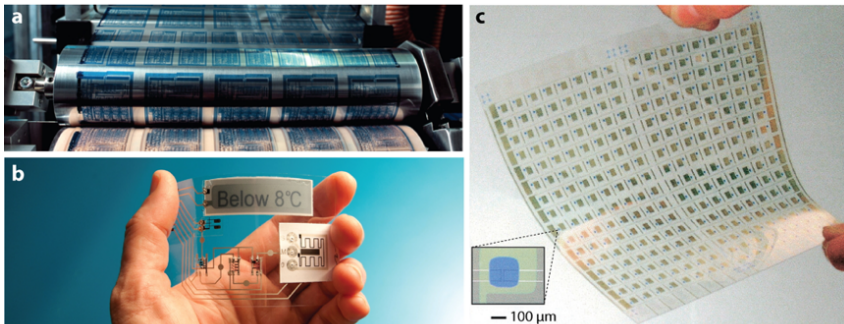
1.1 Motivation

Liquid jet or liquid bridge stretching is a phenomenon that is relevant to many applications like atomization, crystallization, car soiling, oil recovery, coating, fiber spinning, rheological measurements, and typical industrial printing processes, to name a few [1–6].

One of the most widespread and oldest production processes is industrial printing. Printing applications have become an integral part of everyday life. Almost every commercially available product has features that are printed in some form or another. Even though the printing process was invented more than 1000 years ago, we have seen new developments in recent years. The application field is no longer limited to visually perceptible information imprints on media such as newspapers, magazines, cardboard packaging, or consumer products. In the recent past, researchers have also been working on integrating electrical component properties on silicon wafers, textiles, or flexible plastics [7, 8], as illustrated in figure 1.1. Such printing processes make it possible, for example, to produce printed circuit boards more cost-efficient than with conventional silicon-based electronics [9, 10]. It also makes it easier to integrate functions such as data transfer or lighting to consumer products.

However, the development of accurate control methods of these technologies is still in its childhood. For example, much higher demands are placed on print resolution than before when producing printable electronics. Printing processes must be safely controlled on length scales of about

1 Introduction




 Kumar S. 2015.
Annu. Rev. Fluid Mech. 47:67–94

Figure 1.1: Examples of printed electronics. (a) A roll-to-roll manufacturing process PolyIC, Germany. (b) A temperature sensor Thin Film Electronics ASA, Norway. (c) An active matrix backplane circuit; the inset is an optical micrograph of a typical transistor. Reprinted from [15] with permission of Annual Reviews, Inc.

120 nm [11] to produce printed electronics reliably with high accuracy. The current technological know-how is not sufficient to achieve such resolutions for a wide scale of products. Besides optimized printing substrates [12], precise process control is needed, which requires an understanding of the physical mechanisms involved. A central problem that is not yet fully understood is how the fluid is transferred from one surface to another [13]. The complexity arises from the short lengths scales and time scales in which the process takes place in combination with a variety of complex flow phenomena that may occur, such as finger instabilities [14]. The elongation behavior of individual liquid bridges and the interaction of the bridges play an essential role in drop transport and, thus, in the quality of the print result [15].

Another motivation example for the investigation of liquid bridges lies in the safety of flight operations and modeling of the ice accretion. The liquid bridges are involved in the rebound effects of impacting ice particles on wet engine surfaces and leading to the agglomeration of ice patches on engine surfaces. The phenomenon is also known as ice crystal icing.

The undesirable phenomenon of ice crystal icing in aircraft engines has led to various engine failures and damages in the past [16]. The term ice crystal icing describes ice building up on engine surfaces when an aircraft flies through a cloud of supercooled liquid droplets. Although ice crystals do not adhere well to cold airframe surfaces, such particles can adhere to the inner engine surfaces due to the crystals' partial melting in a hot engine environment or impact with a hot substrate. Other droplets that freeze on impact or shortly after can accumulate in areas with already melted particles, see figure 1.2. The ice aggregates to ice patches until the adhesion forces are overcome, and the patches come loose from the engine surface. They do not only represent a constriction and thus a flow change in the inflowing air and lead to unwanted changes in performance, but loosening ice pieces can also cause damage to turbine components if they suddenly detach from the surface and strike components inside the engine at high-speed [17, 18].

Ice build-up in jet engines is a problem that, although it occurs frequently, cannot be prevented until today. Efforts to gain a complete understanding of the processes involved are very complex due to a large number of relevant physical parameters, such as high flow and circulation speeds, high-temperature gradients, and multiphase systems. Thus, it is necessary to characterize a threshold impact velocity for particle adherence/rebound, which depends on the thickness of the liquid film, wall temperature, particle size, and shape. The rebound velocity is influenced by the dynamics of a stretching liquid bridge between the ice particle and the wetted substrate.

In both examples, a generic liquid bridge expansion represents the physical core process. A good understanding of the hydrodynamics of the bridge stretching can help to improve the accuracy of industrial printing processes or to understand better under which circumstances ice crystal icing can occur. They show the bandwidth at which the phenomena need to be understood, ranging from higher viscous printing processes with several mPas to icing problems with a typical viscosity of about 1 mPas for water in ice crystal icing phenomena. Investigating the liquid bridges' behavior with different viscous properties in the course of fast expansion rates gives a good insight into the relevant time and length scales at play. Consequently, this work investigates highly accelerated liquid bridges with minimal heights to gain new insights into expanding liquid bridges. Therefore, the flow in a thin liquid bridge between two substrates, generated by an accelerating downward motion of the lower substrate, is studied

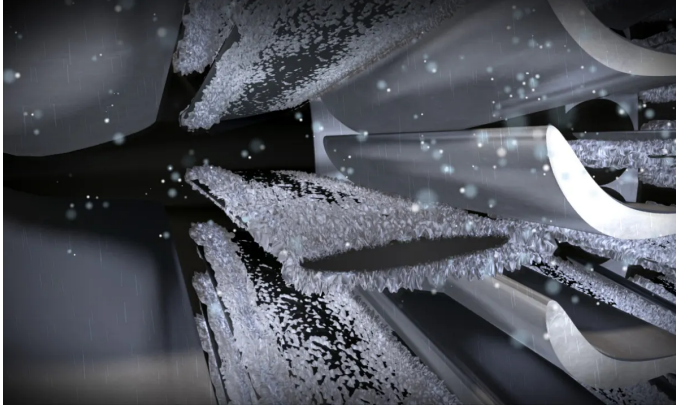


Figure 1.2: Ice accretion on a stator blade. Due to elevated temperatures inside the jet engine, a thin film of liquid water can form, allowing the accumulation of additional ice crystals. Reprinted from [19] according to the NASA Media Guidelines [20].

experimentally and modeled theoretically. The novel feature of this study is that one substrate can be moved with very high accelerations and that bridges with small heights can be investigated. In the conducted parameter studies, accelerations up to 180 m/s^2 and initial bridge heights of $50 \mu\text{m}$ are presented.

1.2 Hydrodynamic Phenomena in a Liquid Bridge

In this section, the state-of-the-art research for the topics cavitation, finger instability, and pinch-off in the context of the liquid bridge stretching is presented. Parts of this section have been published in [21, 22].

A generic fluid bridge stretching has been investigated first in [23–25] more than a hundred years ago. The dynamics of liquid jets and bridges have been studied broadly since then. Numerous extensive reviews of this field demonstrate state-of-the-art modelling approaches [26–30]. Currently the topic of liquid bridge stretching is of great relevance for different industrial applications like coating, fibre spinning, gravure printing and

1.2 Hydrodynamic Phenomena in a Liquid Bridge

atomization [1–4, 30, 31]. Liquid bridge stretching and its pinch-off govern the phenomena agglomeration of wet particles [32–34]. Furthermore, understanding and predicting the pinch-off of liquid bridges are highly relevant in drug delivery and micro-dispersion applications for controlled and efficient dispensing of liquid volumes [35], for instance, with double emulsion droplets in shear flow [36]. Stretching of non-Newtonian jets is also used for the rheological characterization of these complex liquids [37–39]. Comprehensive studies about jet dynamics and, particularly, on liquid bridge stretching can be found in the review papers and books [26–29]. Detailed studies on the effects of the material properties of the Newtonian and non-Newtonian liquids can be found in [40, 41].

Most studies in this field were conducted for relatively low stretching rates at which the contour evolution of the liquid bridge [31, 42, 43], or the dynamics of liquid bridges were investigated. From these studies, it is known that different phenomena can be observed for pinned and unpinned contact lines during the stretching process [44].

In the present study, pinned liquid bridge stretching dynamics and pinch-off time scales are investigated for the first time at stretching rates up to 180 m/s^2 at viscosities down to 1 mPas and at initial liquid bridge heights down to $50 \mu\text{m}$. At these velocities and initial heights, fingering and additional phenomena such as cavitation with and without fingering occur, which are studied here in detail.

1.2.1 Cavitation Phenomena

Cavitation can be recognized by the sudden formation of a cavity within a liquid or soft materials, usually due to a dynamic pressure drop. In technical applications, the occurrence of cavitation in liquids can lead to constricted flow cross-sections, mechanical vibrations, and cavitation erosion. Liquid cavitation and the surrounding pressure distribution were first investigated extensively by Rayleigh [25, 45]. The dynamics of a spherical bubble in an infinite body of incompressible fluid are described through the Rayleigh-Plesset equation in (1.1). From different studies, it is well known that the pressure resulting from a collapsing bubble in the vicinity of a wall can exceed several GPa [46, 47], which illustrates the order of magnitude of the forces released during cavitation.

1 Introduction

$$R \frac{d^2 R}{dt^2} + \frac{3}{2} \left(\frac{dR}{dt} \right)^2 + \frac{4\mu}{\rho R} \frac{dR}{dt} + \frac{2\sigma}{\rho R} + \frac{\Delta P(t)}{\rho} = 0 \quad (1.1)$$

In equation (1.1) R represents the radius of the cavitation bubble, and $\Delta P(t)$ the difference between the internal and external pressure. The remaining variables describe the surrounding liquid properties, introduced in table 2.2.

Besides cavitation in liquids, this phenomenon has also been observed within soft materials such as rubber or adhesives or within liquid phases in solids such as swellable materials [48]. Here cavitation usually leads beside the material damage close to the surface also to a damaged carrier material and therefore shows altered material properties as a direct consequence. The cavitation of soft materials has been observed for quite some time [49, 50]. Many studies investigating cavitation in solid or soft materials use methods known from liquid cavitation studies, such as critical pressure. For soft materials, the critical onset pressure was derived via an approach using material properties as modulus of elasticity [51] and later extended with a component for interfacial tension [52]. More refined models are still based on this approach nowadays [53, 54].

It is already known from the preceding studies that dynamic force fluctuation can be measured during tensile strength tests of soft materials. Similar force curves were measured in tensile investigations with liquid bridges [55]. Those forces indicate highly non-stationary pressure dynamics inside the bridge during the elongation process. Studies have shown that due to the high dynamics, cavitation events are not occurring at the vapor pressure level but below a characteristic threshold pressure [46, 56]. The onset of nucleation and bubble growth behavior during expansion experiments have already been investigated for a long time [49, 52], initially starting with soft materials. Nevertheless, especially the physics of cavitation events during liquid bridge stretching is not fully understood until today. The existing models for stretching experiments refer mainly to growth behavior after bubbles have already formed or required an initial bubble size. Those models are based on material properties, mostly on surface tension, and use energy balances to describe a cavitation threshold for soft materials [57–59]. In this study, the cavitation shall be investigated with an estimated pressure inside the liquid bridge. Experimental studies have observed cavitation during liquid bridge expansion [55], but no applicable theories are available for describing the flow behavior and

defining a cavitation threshold.

The combined occurrence of cavitation and finger instabilities is known from different studies [46, 56, 60]. Thereby bridge elongation tests are performed to investigate the effect of the elongation speed on the mutual influence of finger instabilities and cavitation events. In contrast to the present study, these phenomena are only observed in substrate elongation tests with highly viscous fluids ($> 5 \text{ Pa s}$) and low velocities ($< 10 \text{ mm/s}$). In these studies, the force development during strain is measured, and the occurrence of a force plateau is correlated with the cavitation events. It was found that the cavitation events influence the finger instabilities because the cavitation bubbles grow much faster and prevent the growth of the finger patterns inside the bridge. It is found that the main factors leading to cavitation events are the initial bridge height, the elongation speed, and the viscosity of the used liquid. Also, a threshold force is derived, allowing the conception of a cavitation onset map [56, 60].

1.2.2 Fingering Instability of the Liquid Interfaces

If the bridge expansion is investigated for particularly thin gaps, finger patterns can be formed at the free liquid interfaces. Especially for small bridges with large diameters, the retraction velocity of the surface during strain is very high and supports the occurrence of finger instabilities.

If the initial height of a liquid bridge H_0 is much smaller than its initial diameter D_0 , the dimensionless height is $\lambda \ll 1$ with $\lambda = H_0/D_0$. For such cases, the surface of the liquid bridge can become unstable because of the high interface retraction rates and small initial liquid bridge heights. Due to the small initial heights and large initial diameter, the conditions are similar to those in Hele-Shaw flow cells. Those instabilities occur due to low viscous liquid displacing a higher viscous liquid [61].

Frequently observed phenomena are finger patterns formed from growing instabilities in fixed-height Hele-Shaw cells for transverse [61] or radial [62–65] flows. The study [66] compares modified wave number theories based on the fastest growing mode from [67, 68] to experiments in radial flows. In the study [69], the predictive model for the number of fingers formed at a radially expanding interface of the liquid spreading between two fixed substrates is derived from the stability analysis.

The problem is different if the flow is caused by the substrates' motion

1 Introduction

and, therefore, a changing gap thickness. For example, the displacement rate of a liquid bridge under a defined pulling force is investigated in [70]. The measurements from [71] were conducted at very low stretching speeds of $20 - 50 \mu\text{m/s}$, high viscosities of 30 Pas and large initial heights. For a lifting Hele-Shaw cell, [55] developed a model for the interfacial stability of the liquid bridge, leading to a prediction of the maximum number of fingers. In [71–75] stretching liquid bridges in lifted Hele-Shaw set-ups were investigated. In most of these cases, the stretching speed is constant and is relatively small, such that inertial effects are comparably small, and the acceleration is relatively low [76].

The analysis of finger instability has been further generalized, where the influence of radial viscous stresses at the meniscus has been taken into account [72]. For identifying the most unstable mode, the maximum amplitude has to be considered instead of the usual approach of selecting the fastest growing modes [72]. This approach accounts for the non-stationary effects in the flow, even if the substrate velocity is constant. The amplitude growth due to the disturbances is not exponential since the parameters of the problem, mainly the thickness of the gap, change in time. More recently, [77] showed in an analytical and numerical study that inertia has a significant impact on finger formation at higher velocities, especially on dendritic-like structures on the fingertips.

Nevertheless, it is important to note that the physical mechanism of instability in all these problems is the same. Even the often quoted Saffman-Taylor Instability [61, 78], can be derived using a straightforward algorithm for linear stability analysis. In all problems, the pressure gradient causes instability in the liquid at the interface. In this study, we claim that the fingering instability is analogous to the Rayleigh-Taylor instability [79, 80] associated with the pressure gradient caused by the liquid acceleration or gravity.

The onset of instability is caused by the initial smallest natural disturbances and shows up at the beginning only by small perturbation amplitudes of different wavelengths. In this early phase, the equations of motion can be linearized. Therefore, the beginning of the Rayleigh-Taylor instability can be described using a linear stability analysis. In the original study, the wavelength of the instability is derived by the fastest growing mode approach but newer studies show that an approach using the fastest growing modes instead is more accurate [72].

Since in the problem of the separation experiment, the fingers develop

1.2 Hydrodynamic Phenomena in a Liquid Bridge

on the edge of the bridge and then advance from there into the center, the wavenumber for patterns is determined at the beginning in the initial phase of instability. Therefore a linear stability analysis can be used to make a statement about the final number of fingers in the outer area. An estimation of the number of fingers in the center are of the liquid bridge would not be correct because the amplitudes are already too large.

Linear stability analysis of the liquid bridge accounts for the inertial term, the viscous stresses, and capillary forces in the fluid flow. It allows the prediction of the maximum number of fingers. This number is obtained using the mode exhibiting the highest amplification rate to interface perturbations. The second criterion for the finger threshold is associated with a limiting value of the analytically derived dimensionless amplitude at which finger patterns are observable. Both requirements lead to the same scaling of the threshold parameter for finger formation and agree well with the experimental observations.

In this work, the number of fingers is predicted as a function of the substrate acceleration in a lifted Hele-Shaw cell. In contrast, previous studies were based on experiments in fixed or lifting Hele-Shaw cells with significantly lower lifting velocities. Those predictions (e.g. [66], [67], [68], [61], [81]) deviate significantly from the present measurement results due to physical differences among the experiments. In other words, since no characteristic velocity exists in this presented study (only acceleration a), the main dimensionless numbers, like the capillary number Ca , are defined entirely differently.

1.2.3 Pinch-Off of a Liquid Jet

Lastly, the different studies for predicting the pinch-off of liquid bridges are summarized. The focus is on liquid bridges that are too large for cavitation and finger instability to occur. Therefore, the investigated bridges do not split up into smaller bridges and develop a single jet.

The pinch-off of liquid bridges has been investigated both experimentally [82] and analytically [25] for over a hundred years. It was found that the maximum ratio of the stable length to the diameter of a breaking jet can be derived by linear stability analysis. Later investigations followed, which theoretically estimated and experimentally determined the maximum bridge height before the pinch-off of a quasi-stationary liquid bridge [83–87]. Only with improved measurement technology could the dynamic

1 Introduction

bridge expansion be recorded to provide experimental data to validate analytical theories [31, 88, 89].

The bridge expansion can be divided into different phases. The characteristic parameter is the capillary number. For slower strains, a uniform bridge elongation can be observed, where the capillary forces dominate and determine the shape of the bridge until the pinch-off [90]. Only with increasing the capillary number the frictional forces increase and determine the bridge pinch-off process. The viscous and inertial forces delay the breaking up of the bridge, and a typical constant curvature of the bridge profile is no longer visible. Due to the dominating viscous and inertial forces, the liquid bridge has the form of a cylindrical jet. This behavior typically occurs at higher expansion rates.

The influence of viscosity on bridge pinch-off behavior was further investigated in [91]. It was observed that an asymmetric unilateral pinch-off occurs at one side of the bridge, while at high viscosity, pinch-off occurs simultaneously on both substrates. This seems due to the viscosity stabilizing the bridge during the elongation process and therefore prolonging the pinch-off. A similar effect can be observed with increasing stretching velocity. Numerical investigations were added [91], which allow simulating the experiments for lower stretching rates. More recent studies have provided new insights into the influence of surfactants [92] pinned liquid bridges [93].

One of the objectives of the liquid bridge investigation is to determine the liquid volume after a pinch-off. This is particularly relevant for optimizing industrial printing processes. Investigations of the wettability effect, as in [94, 95], show that a higher contact angle on a substrate leads to a better liquid transfer to a substrate with a lower contact angle. This effect is further enhanced at lower elongation rates. With similar wettability conditions on both substrates, symmetrical liquid distributions are obtained after a pinch-off. Furthermore, the effect of non-cylindrical liquid bridge elongation was investigated in [15]. It is shown that a vertical liquid bridge elongation combined with a rotational movement leads to more liquid being transported by the capillary forces towards the stationary liquid. This leads to a lower transfer rate towards the moving substrate, due to the dominating capillary forces.

Of particular importance is the study [96], in which the pinch-off behavior at higher dynamic strain rates of up to 180 m/s^2 was investigated. Those observations cannot be explained with existing models, since they

were designed for lower speeds. For this highly relevant dynamic range, a model for estimating the time to pinch-off based on bridge geometry, bridge acceleration, and material properties could be derived for bridge heights $\lambda > 0.5$.

1.3 Thesis Outline

This thesis aims to improve the understanding of fluid bridge stretching at high accelerations with low viscous fluids to develop and validate reliable physical predictions for the occurring phenomena.

Before presenting the main parts of the following investigations, the fundamental hydrodynamics at play during the fast bridge stretching are introduced. For the thesis structure, the initial height of the liquid bridge is used as a guiding outline. For example, cavitation and finger patterns rise during the bridge stretching at minimal liquid bridge initial heights. As the bridge height and the form ratio of the bridge λ increase, the cavitation effects disappear, and only finger patterns are apparent. As the form ratio increases further, both of these phenomena disappear. A singular liquid bridge expansion with pinch-off can be recognized. In this order, the central topics are presented in the following.

In **Chapter 2**, a detailed description of the configurations of the experimental set-up and procedures is presented. Subsequently, the applied characterization techniques and imaging methods are presented.

In **Chapter 3**, the bridge curvature, the centerline profile, and the meniscus profile during fluid bridge expansion are presented. Subsequently, the pressure distributions at the substrate surface and the centerline of the circumferential surface are derived based on the previously gained knowledge.

In **Chapter 4**, the cavitation that forms on the substrate surfaces during bridge expansion is investigated. Next, a prediction of the cavitation bubble diameters is produced based on the previously proposed theoretical model. This prediction is then validated with the help of the available measurement data.

In **Chapter 5**, the formation of finger patterns during rapid bridge expansion is investigated. First, the observations are analyzed, and then a linear stability theory, based on the pressure distribution at the centerline

1 Introduction

of the circumferential surface, is developed. The results will be used to provide and validate a threshold value for predicting finger formation and an estimate of the number of fingers.

In **Chapter 6**, the pinch-off time of rapidly stretched liquid bridges is investigated. First, a theory for the pinch-off time is derived and validated with the available measurements' help. It will also be validated in the context of existing predictions.

In the final **Chapter 7**, the last conclusions of the study and an outlook on possible future research are presented.

2 Experimental Methods and Procedures

In this chapter, the main components of the experimental setup, methods of post-processing, and the method of error analysis are described. The description of the setup includes the design of the stretching apparatus and the configuration of the observation system. Also, the preparation of the working liquids and substrates is described in detail.

2.1 Experimental Set-up

All investigations performed for this study are based on a rapidly stretched liquid bridge formed between two horizontally aligned substrates. The stretching motion is induced by the translatory motion of the lower substrate while the upper substrate remaining fixed.

An overview of the experimental setup is shown in figure 2.1. The main component of the stretching apparatus is the linear drive, which is regulated by a servo controller. The servo controller receives its commands from the central control unit (CCU). The observation system consists of two high-speed video systems. The first camera (camera 1) records the side profile using a telecentric lens and a telecentric white light LED, the recordings of this cameras are hereafter referred to as side view. The second high-speed video system (camera 2) records the liquid bridge from above through the backside of the fixed upper substrate with coaxial illumination, implemented with a beam splitter. The images of the camera 2 are referred to as top view in the following. The CCU controls both camera systems. Furthermore, for each measurement, the following parameters are recorded by the CCU: the ambient lab conditions humidity, temperature, and pressure. The CCU can centrally manage the measurement procedure with the help of a LabVIEW user interface.

2 Experimental Methods and Procedures

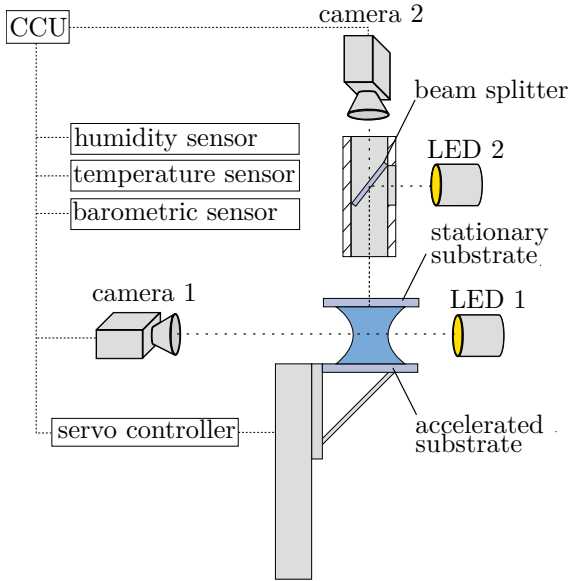


Figure 2.1: Sketch of the measurement set-up with data connections and the sensor system used.

2.1.1 Stretching Apparatus

The linear drive is the main module of the setup, allowing to investigate highly dynamic stretching motions. As already described, only the lower substrate is connected to the carriage of the linear drive and is subjected to the induced motion. A constant acceleration motion was chosen over a constant velocity mode for the operational mode of the linear drive. Mainly for the following two reasons: Firstly, a constant substrate velocity requires a preceding acceleration phase to produce a constant velocity state. Therefore, the constant velocity criteria would not be satisfied during the starting phase, making an analysis of the active forces more complex. Secondly, a constant acceleration allows a more direct estimation of inertial forces, directly proportional to the modeling sections' acceleration later.

Specification of the linear drive In order to investigate phenomena occurring during industrial applications like gravure printing, as described

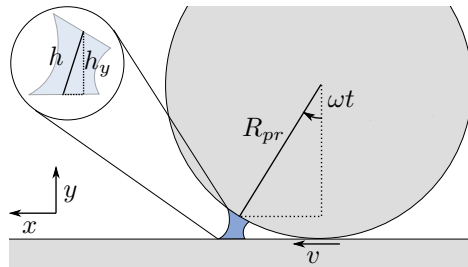


Figure 2.2: Sketch of the kinematics of a printing cylinder.

earlier, the set-up should be able to provide accelerations of the same order. The required acceleration for the stretching apparatus was derived from typical industrial gravure printing machines e.g. *Hsing Wei* with printing speeds of 200 m/min and a cylinder diameter of 135-285 mm. In order to translate the rotational speeds to a translational acceleration, the stretching acceleration \dot{h}_y has to be determined, see figure 2.2. The liquid bridge length is represented by h . Due to the wheel constraints and a non-slip condition between the rolling cylinder and the printing substrate

$$v = \omega R_{pr} \quad (2.1)$$

and with the help of the kinematic relations from figure 2.2 the vertical component of the bridge can be estimated to:

$$h_y = R_{pr}(1 - \cos(\omega t)). \quad (2.2)$$

Based on the height the vertical bridge acceleration \ddot{h} is defined as

$$\ddot{h}_y = \omega^2 R_{pr} \cos(\omega t). \quad (2.3)$$

Due to the bridge pinch-off occurring shortly after the printing cylinder and substrate had direct contact, the angle ωt can be approximated to be small. Therefore, $h_y \approx h$, leads to

$$\ddot{h} = v^2 / R_{pr}. \quad (2.4)$$

According to the introduced variables, the required stretching acceleration should be at least 165 m/s^2 . The stretching apparatus has to maintain accelerations of this magnitude to investigate stretching under

2 Experimental Methods and Procedures

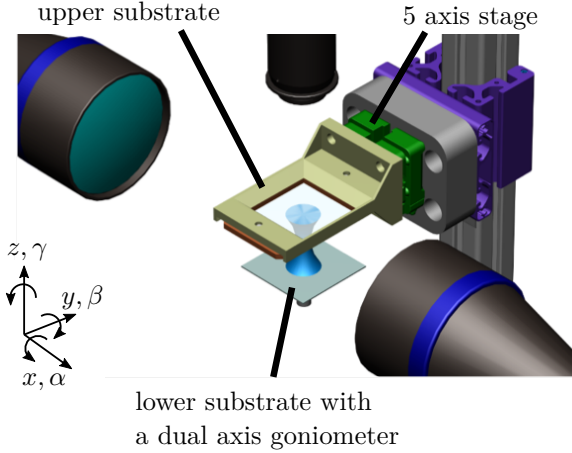


Figure 2.3: Sketch of the measurement set-up including the alignment systems in isometric view.

similar conditions. The small-angle approximation is satisfied due to the time scale of typical bridge pinch-off events being of the order of several ms. Therefore, $h \approx h_y$ and the rotational effects are neglected.

A linear drive able to perform the derived accelerations is available from Akribis, type SGL100-AUM3. The necessary servo controller is from the company Metronix and of the type ARS2108. Both were already available at the institute from previous studies [96]. The linear drive had to be parameterized anew to provide accelerations up to 180 m/s^2 reliably. The servo controller is connected via the communication protocol CANOpen with the help of the module EtherCAT to the CCU. This setup allows sending the process parameters directly to the servo controller, monitoring the performance of the linear drive. The linear unit has a peak force of 900 N and a positioning accuracy of $5 \mu\text{m}$ [97].

Measuring Section The measuring section consists of two substrates orientated horizontally. The lower substrate is mounted on the carriage of the linear drive, whereas the upper one is fixed to the stationary setup structure. To ensure concurrency between the two substrates on the scale of $\mathcal{O}(50 \mu\text{m})$ and easily adjust the orientation of the substrates, a five-axis

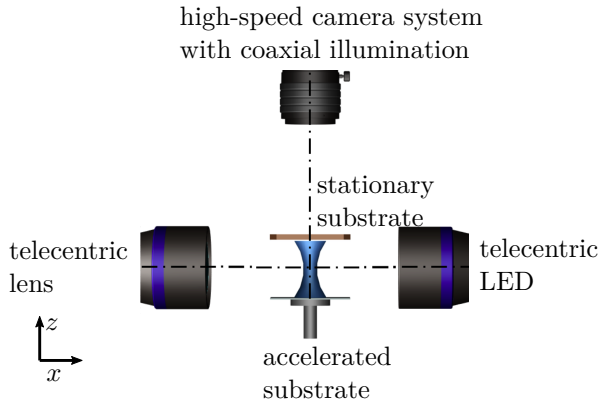


Figure 2.4: Sketch of the measurement set-up including optical paths in side view. Adapted from [21] under CC BY 4.0.

stage and a goniometer are used, figure 2.3.

Due to the small bridge heights, the degree of concurrency of the two substrates significantly affects the hydrodynamics of the bridge [94]. Therefore, it is necessary to precisely adjust and control the orientation of both substrates to each other. Orientation control at the upper substrate holder is made possible by implementing a five-axis stage. This allows one to change the translation position in the directions x , y , and z and rotation orientation in β and γ . The accuracy of the angle setting for the pitch is $\gamma = 0.17^\circ$ and for yaw $\beta = 0.36^\circ$. A dual-axis goniometer type stage is used on the lower substrate holder, which has two degrees of rotational freedom and allows the orientation of the substrate to be set in α and β with an accuracy of 0.17° .

After the position of the two substrates is set and the orientation is aligned precisely according to the alignment procedure introduced later in section , a validation of the aligned system is performed. The substrate distance is measured at defined positions using an interferometric point sensor CHRcodile 2 SE from *Precitec*. The current setup allows thickness measurements between $2\ \mu\text{m}$ and $250\ \mu\text{m}$ [97]. After aligning the substrate, according to the later introduced measurement protocol, the validation results are based on twelve measurements with a readjustment done after every third measurement to take systematic measurement errors into account. For the validation measurement, the distance between

2 Experimental Methods and Procedures

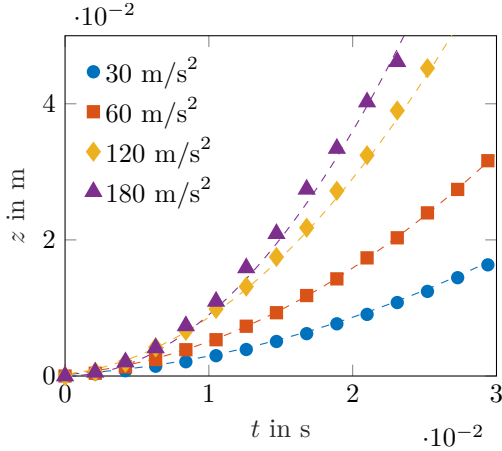


Figure 2.5: Validation of the linear drives stretching rate. Comparing the position of the linear drive carriage with the ideal position for each acceleration.

the two substrates was recorded at distinguished positions. The alignment measurement was performed four times. Each consists of three experiments, giving an accuracy of substrate parallelism of $1.29 \pm 0.25 \mu\text{m}/\text{mm}$. The alignment procedure is described in the next section.

Another parameter that was validated is the acceleration of the linear drive and its control accuracy. The Metronix linear drive controller provides the current carriage position over a serial RS232 port. This data stream is used and compared to the ideal position the carriage should have for the requested acceleration. A comparison of the signals and the ideal position over time is shown in figure 2.5. In figure 2.6, the respective accelerations derived from the measured positions of the linear drive are shown. They are calculated by polynomial fitting to the function $f(x) = ax^2$. The dashed lines show the 95% confidence interval for each acceleration. The confidence interval for larger accelerations up to $\pm 2.5 \text{ m/s}^2$ for 180 m/s^2 . The experimentally determined accelerations agree well with the ideal ones. Therefore, the control accuracy can be assumed to be good.

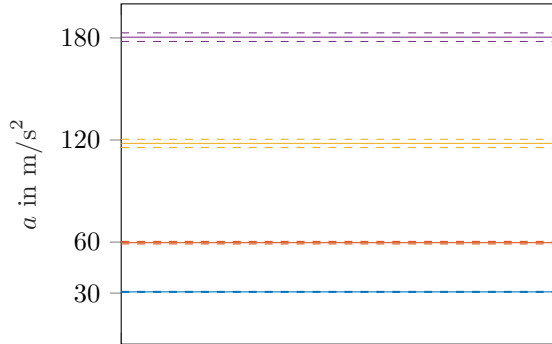


Figure 2.6: Validation of the linear drives stretching rate. Comparing the accelerations determined from each position curve through a polynomial fit and their respective 95% confidence intervals.

2.1.2 Fluid and Substrate Preparation

The material parameters: viscosity, surface tension, and density are varied for the investigation of the liquid bridge stretching. When selecting the liquids, the focus for this study was set on Newtonian liquids. Furthermore, the test liquid should have a low vapor pressure because the experiments are carried out in an open test environment.

The mass decrease during preparation time should be as low as possible. For this reason, investigations were carried out with water-glycerol solutions with different viscosities and surface tensions. Glycerol was purchased with a degree of purity above 97%, and the used water was deionized (*Milipore, Mili-Q Type 1*) to avoid influences of impurities in the liquids affecting the hydrodynamics. The material properties were partly determined experimentally and validated with available data from the literature.

Temperature dependent material properties The temperature dependency of the liquid properties such as the density, dynamic viscosity, and surface tension has to be included in the post-processing of the experimental data due to temperature changes in the unconditioned lab room of $\Delta T = 20^\circ$ during the year. Therefore, the ambient temperature is recorded with a thermocouple of type K (Class 1 DIN EN 60 584-3), and

2 Experimental Methods and Procedures

the corresponding liquid properties are determined based on numerical evaluations. Those different approaches are summarized in the following paragraphs.

Density An experimentally determined density function for glycerol-water solutions in the temperature range between $17 - 83^\circ$ is proposed by [98, 99]. The study is based on measurements using a pycnometer method and a circulation thermostat. A pycnometer is a vessel with a precisely determined volume that characterizes the weight per volume and reveals the density of the liquid. The temperature-dependent glycerol density ρ_g is calculated accordingly as

$$\rho_g = 1277 - 0.654T. \quad (2.5)$$

The temperature dependent water density ρ_w is represented by

$$\rho_w = 1000(1 - \left| \frac{T - 4}{622} x \right|^{1.7}). \quad (2.6)$$

The prediction of the density of water is accurate with an error less than 2% [98, 100]. With help of the glycerol concentration in mass-% (C_m) the density of the mixture can be calculated as

$$\rho = \rho_g C_m + \rho_w (1 - C_m). \quad (2.7)$$

The proposed empirical equation (2.7) is accurate within $\pm 0.8\%$ based on the observations from [99], despite neglecting the interactions of the two components. More detailed liquid properties for several temperatures can be found in table 2.2. The equations above are of empirical type and despite the missing unit consistency they agree rather well with glycerol or water density values.

Dynamic Viscosity The measurement of the dynamic viscosity is performed with a DV-III Ultra Rheometer from *Brookfield*. The rheometer measures the shear stress at a defined shear rate using a torsion spring. Shear stress is applied to the liquid via a rotating plate. The resistance of the liquid is determined indirectly via the torsion of the spring. A temperature control unit from *Huber* is used to measure the dynamic viscosity as a function of temperature. The measurements are repeated ten times per sample, and three samples per liquid are examined. A total of $n = 30$

measurements are performed for each temperature setting and liquid. The results are compared to the prediction of a viscosity solution from [98], which claims to be accurate within 5%. An exponential function for the dynamic viscosity of water is derived in [98] to be

$$\eta_w = 1.79 \exp \frac{(-1230 - T)T}{36100 + 360T}, \quad (2.8)$$

and for glycerol in the form of

$$\eta_g = 12100 \exp \frac{(-1233 + T)T}{9900 + 70T}. \quad (2.9)$$

By following the assumptions of [98], the dynamic viscosity of the glycerol-water solution can be calculated as

$$\eta = \eta_w^\alpha \eta_g^{1-\alpha}, \quad (2.10)$$

with α being a temperature and saturation dependent function

$$\alpha = -C_m + 1 + \frac{(1 - C_m)C_m(0.036T + 4.9)(0.705 - 0.0017T)^{3.5}}{(1 - C_m)(0.036T + 4.9)(0.705 - 0.0017T)^{2.5} + C_m(0.705 - 0.0017T)}. \quad (2.11)$$

The experimentally derived dynamic viscosity is compared to the theoretical values from equation (2.10) based on [98] in figure 2.7. The overall error is below 2% between the experimentally and predicted viscosity values. More detailed liquid properties for several temperatures can be found in table 2.2.

Surface Tension The surface tensions of the different liquids are determined with help of temperature and solution dependent predictions from [101, 102]. The surface tension is characterized with the pendant drop method using a DSA100E by *Krüss*. The contour of a pendant drop is analysed using the Young-Laplace equation. The surface tension can be determined by the hydrostatic pressure and optical evaluation of the radii of the curvature. To determine the temperature influence, the drop and the ambient air were heated in a closed atmosphere. To calculate the

2 Experimental Methods and Procedures

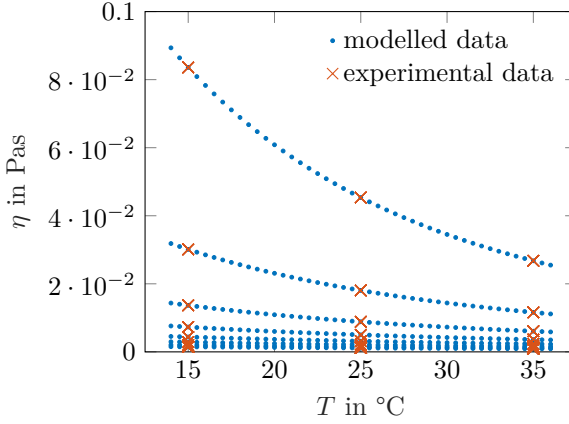


Figure 2.7: Comparing the experimentally determined dynamic viscosity with the prediction based on [98] for *Gly*10 up to *Gly*80.

surface tension of the glycerol-water solution, first the surface tension has to be calculated for both liquids independently. For the surface tension of the water the following equation applies

$$\sigma_w = 235.87 \left(1 - 0.625 \left(\frac{1}{647} (-T - 273.15) + 1 \right) \right) \left(\frac{1}{647} (-T - 273.15) + 1 \right)^{1.256}, \quad (2.12)$$

and then the surface tension of glycerol can be calculated as

$$\sigma_g = 0.0878 \left(1 + \frac{1}{850} (-273.15 - T) \right)^{0.755}. \quad (2.13)$$

With both a temperature and solution dependent prediction for the surface tension follows in the form of

$$\sigma = (\sigma_g C_m + \sigma_w (1 - C_m)) \times 10^3. \quad (2.14)$$

The surface tension values for various temperatures and solutions can be found in table 2.2.

Contact Angle The contact angle gives insight into the equilibrium state between the solid (S), gas (G), and liquid (L) phase (see an example in



Figure 2.8: Contact angle measurement of distilled water applied to aluminium substrate.

figure 2.8). Balancing the surface forces allows classifying the wetting regime of an ideal surface. The balance point is reached when the Gibbs free energy is minimal. Young [103] derived the components of net force for a planar geometry for a static contact angle θ as

$$\sigma_{SG} = \sigma_{SL} + \sigma \cos \theta. \quad (2.15)$$

Where σ_{SG} represents the interfacial tension between the solid and gas phase and σ_{SL} the interfacial tension between the solid and liquid phase. σ represents the previously introduced surface tension between the gas and liquid phase. Under real-world conditions, the surface of the substrate is usually not ideal, and inhomogeneities, surface roughness' and liquid contaminations lead to different contact angles. The order of the deviation from an ideal wetting state is expressed with the dynamic contact angles. Those are the advancing (θ_{adv}) or the receding contact angle (θ_{rec}). The difference of both is defined as the contact angle hysteresis $\theta_{hyst} = \theta_{adv} - \theta_{rec}$. With increasing θ_{hyst} , the advancing and receding angles distance each other further from one another. On rough substrates, the static contact angle can also increase [104, 105].

In this study, precautionary measures were introduced in the form of cleaning protocols to reproduce measurements with similar contact angles. The static contact angle is used as a parameter to verify the surface cleanliness, as explained later. Due to the available telecentric lens setup, the cleanness of the substrate can quickly be verified, measuring the contact angles. Additionally, the contact angles are confirmed with an industrial

2 Experimental Methods and Procedures

Table 2.1: Experimentally determined contact angles on quartz glass, sapphire glass and polished aluminium substrates with their 95% confidence interval.

liquid	quartz glass θ in $^{\circ}$	sapphire glass θ in $^{\circ}$	aluminium θ in $^{\circ}$	silanised θ in $^{\circ}$
DW	35.4 ± 2.1	47.1 ± 2.8	56.9 ± 5.3	109.2 ± 3.1
Gly80	37.9 ± 1.5	44.5 ± 1.6	46.13 ± 4.3	110.1 ± 4.2

system from the Optical Contact Angle system from *DataPhysics*, which also uses a telecentric imaging system to measure the contour of the drop. In the industrial contact angle measuring device, the contact angle is determined with an image post-processing script identifying the curvature of the drop. The contact angle is measured for the liquids distilled water (*DW*) and a 80% glycerol-water solution (*Gly80*) on the substrates quartz glass, sapphire glass, polished aluminum and silanized wafer [106].

Testing Substrates Another parameter modified during the study is the substrate surface to investigate different effects of hydrophobic, hydrophilic, smooth, and rough surfaces. Even though it is known that no wettability and roughness effects are observable during the investigated phenomena' main phase on such a small time scale as investigated in this study. For further explanation, see chapter 3. The main part of the measurements was performed on glass substrates with a mean roughness of $R_a = 21$ nm, see figure 2.9. For bridge pinch-off investigations in chapter 6, polished aluminium substrates are used with a roughness of $R_a = 2.7$ μm . The roughness is determined with a monochromatic interferometer from *Sensofar* of type PLu Neox.

Three different types of glass substrates are used: First is a quartz glass with a contact angle of 35.4° , second a sapphire glass with a contact angle of 47.1° , and third a silanized glass wafer with a contact angle of 110° , as shown in table 2.1. In figure 2.8, an example measurement of the contact angle of a distilled water drop on an aluminum substrate is shown.

Alignment, Measurement and Cleaning Procedure Before forming the liquid bridge, a definite amount of liquid is placed on the lower substrate

$T = 15^\circ$	σ in N/m ²	η in Pas	ρ in kg/m ³
<i>DW</i>	0.0735	0.00114	998
<i>Gly10</i>	0.0725	0.00148	1025
<i>Gly20</i>	0.0716	0.00200	1052
<i>Gly30</i>	0.0707	0.00286	1079
<i>Gly40</i>	0.0697	0.00438	1106
<i>Gly50</i>	0.0688	0.00730	1133
<i>Gly60</i>	0.0679	0.01367	1159
<i>Gly70</i>	0.0670	0.03011	1186
<i>Gly80</i>	0.0660	0.08359	1213
<i>Gly</i>	0.0642	2.28122	1267

$T = 25^\circ$	σ in N/m ²	η in Pas	ρ in kg/m ³
<i>DW</i>	0.0719	0.00089	996
<i>Gly10</i>	0.0711	0.00114	1023
<i>Gly20</i>	0.0702	0.00152	1049
<i>Gly30</i>	0.0694	0.00212	1075
<i>Gly40</i>	0.0685	0.00313	1102
<i>Gly50</i>	0.0676	0.00500	1128
<i>Gly60</i>	0.0668	0.00884	1155
<i>Gly70</i>	0.0659	0.01805	1181
<i>Gly80</i>	0.0650	0.04535	1207
<i>Gly</i>	0.0633	0.90568	1260

$T = 35^\circ$	σ in N/m ²	η in Pas	ρ in kg/m ³
<i>DW</i>	0.0704	0.00072	993
<i>Gly10</i>	0.0696	0.00091	1019
<i>Gly20</i>	0.0688	0.00119	1045
<i>Gly30</i>	0.0680	0.00163	1071
<i>Gly40</i>	0.0672	0.00234	1097
<i>Gly50</i>	0.0664	0.00360	1124
<i>Gly60</i>	0.0656	0.00607	1150
<i>Gly70</i>	0.0648	0.01161	1176
<i>Gly80</i>	0.0640	0.02676	1202
<i>Gly</i>	0.0624	0.40578	1254

Table 2.2: Evaluated liquid properties for $T = 15^\circ$, $T = 25^\circ$ and $T = 35^\circ$ according to the methods described in §2.1.2.

2 Experimental Methods and Procedures

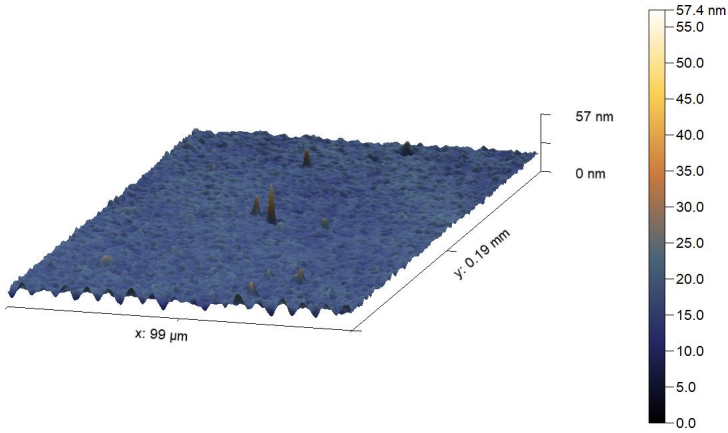


Figure 2.9: Interferometric measurement of a glass substrates surface after several measurement series.

with a gastight precision glass syringe 7105 N from *Hamilton*. For each type of liquid, a separate syringe is used to avoid contamination. After depositing the liquid volume of the lower substrate, the linear drive moves the substrate towards the upper one until a liquid bridge is formed. The height of the liquid bridge is adjusted by positioning the lower carriage with the help of the linear drive. The size of the liquid bridge is implicitly estimated by the profile recorded from the top video system. The syringes error was tested to be within $\pm 1\%$ of nominal volume [107], depending on the viscosity of the liquid.

The linear drive position is controllable over the CCU using a *LabView* interface. The interface acts as a central monitoring and control hub to manage the data in- and output. After the measurement recording is finished, the substrate has to be cleaned. Depending on the used testing liquid, acetone, isopropanol, or *Tickopur R33* are used. Afterwards, disposable lab wipes are used to dry the surface again. The lint and fibers residues from the wipes are removed with nitrogen from a pressure cylinder. The wipes have to be used carefully to avoid scratching the surface. An interferometric surface measurement was performed to validate the surface roughness, as shown in figure 2.9. The roughness is $R_a \approx 21$ nm but without any visible anisotropic contours originating from cleaning procedures. Before starting the next measurement, the contact angle is

checked to ensure a reproducible wettability state, as shown in figure 2.8.

The alignment of the substrates represents a sensible parameter for the symmetry of the liquid bridge during stretching. An unaligned substrate configuration leads to strong asymmetrical effects and can influence the bridge stretching behavior [108]. Therefore, the alignment is controlled after changing one of the substrates' height according to the following behavior. As a first approximation, three steel spheres with a diameter of $d_{sphere} = 1$ mm are put on the lower substrate and are evenly distributed across the surface. The lower substrate is then moved towards the upper substrate until at least one of the spheres touches both substrates. After that, the five-axis stage and goniometer are adjusted to have all three spheres in contact with both substrates.

For more precise alignment, the top-view camera is required. First, a drop of distilled water is deposited on the lower substrate. The lower substrate is then positioned close to the fixed substrate so that both substrates are wetted. Due to the lower viscosity and high surface tension, the shape of the liquid bridge is sensible to small asymmetries in the arrangement of the two substrates. A non-parallel substrate orientation leads to a moving liquid bridge due to the capillary effects. The substrate orientation can be adjusted with high precision with the five-axis stage and goniometer, as described in §2.1.1.

If both substrates are not arranged thoroughly, the capillary forces push the bridge from the side with the wider gap towards the narrower gap, due to a larger capillary pressure at the surface. This leads to effects shown in figure 2.10. A measurement from the top onto the liquid bridge profile is shown with two unaligned substrates in a) and two aligned substrates in b). In figure 2.10a), the liquid is pushed towards the upper left corner due to a lower pressure gradient inside the bridge. After increasing the gap width at the upper left corner by changing the orientation with the five-axis stage and the dual axis goniometer, the bridge profile is now symmetric, as shown in figure 2.10b).

2.1.3 Observation System

For the observation system, two different types of CMOS cameras are used. Both are utilizing the shadowgraphy image technique to visualize the bridge stretching [109, Chapter 6]. For the top-view visualization, a Photron SA-X2 [110] is used. The top camera is mounted on a roller

2 Experimental Methods and Procedures

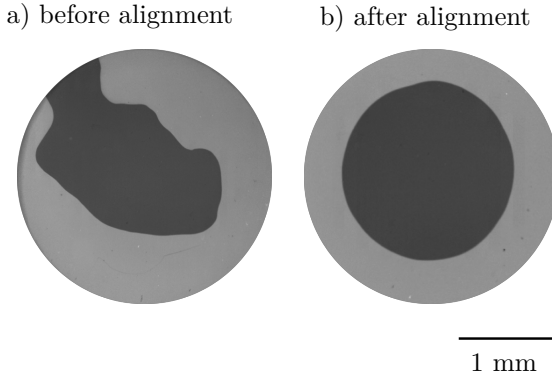


Figure 2.10: Showing a liquid bridge profile from top. The measurements are performed with $5 \mu\text{l}$ of deionised water before a) and after alignment b).

bearing system to move in all three directions freely. A modular setup allows an easy mounting of other optical measuring systems and good optical access from the top with an adaptive positioning system, ensuring that the optical target remains inside the focus area.

For the side-view, a high-speed camera or a high-resolution camera is used, depending on the main experimental requirements.

The two high-speed cameras (Photron SA X2) are applied with a frame rate of 12500 fps and a resolution of 1024×1024 . The pixel size is $20 \times 20 \mu\text{m}$. The alternatively used camera, a pco.edge 5.5 [111], has a resolution of 2560×2160 pixel and a pixel size of $6.5 \times 6.5 \mu\text{m}$. Both cameras can be mounted on rail systems to adjust to different focus planes.

The top-view camera, side-view camera, and the linear drive are triggered through the CCU as the measurement recording is started. The cameras are equipped with different lens systems. The side-view camera is operated with a telecentric imaging system, consisting of a lens and a white light LED. Lens systems with different magnifications were used from 0.19 (TC16M192 from *Opto Engineering* [113]) up to 4 (TC16M009 from *Opto Engineering* [114]). The telecentric lens system allows recording edges, especially curved ones, at high contrast, reducing the uncertainty in finding edge positions.

Perspective effects caused by object displacement can be avoided due to

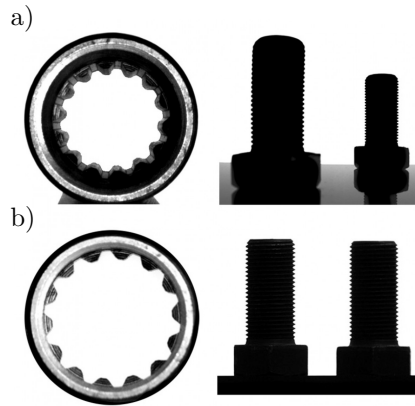


Figure 2.11: Comparison of the lenses: a), two images are shown taken by a standard entocentric optical system. On the left, the inside of a tube is apparent, revealing the typical entocentric perspective errors. On the right side, the screw thread is not resolved properly and is partially blurry; b), two images from a telecentric lens system from *Opto Engineering Srl.* are used. On the left side, only the frontal profile of the tube is visible without any inner features due to the parallel ray beams. On the right side, the screw threads are resolved properly and can easily be tracked without any perspective distortions. Reprinted from [112] with permission of *Opto Engineering Srl.*

the parallel view of a telecentric lens. Objects are recorded with the same size independent of their distance. The advantages of higher contrasts provided from a telecentric optical system are apparent from figure 2.11. In figure 2.11a), an image from an entocentric lens system is shown. This is apparent from the inner features of the tube on the left side. Due to the beam diverging, objects close to the lens appear larger than objects far away from the lens. Therefore, one can see the inner features of the tube in figure 2.11a). Another characteristic of telecentric lenses is apparent on the screw on the right side of the image. The screw thread features are blurry and cannot be recognized across the full height of the screw. In figure 2.11b), the same objects are portrayed but with a telecentric lens and telecentric white light LED setup. On the left side, no perspective

2 Experimental Methods and Procedures

errors are apparent. And at the right side, the distinct features of the screws thread are visual. The distortions of the telecentric lens systems are controlled with the method described by [115] but are in a sub-pixel range and can be neglected. The camera used for the top view is mainly operated with a 12x zoom lens offering a variable magnification of 0.58 up to 7 [116]. The illumination is directed into the lens system using a beam splitter to allow coaxial illumination, as shown in figure 2.1. For both methods, distortion and a size reference calibration is performed and applied in the post-processing steps.

2.2 Image Processing

Self-programmed algorithms have been created with Matlab and Python to efficiently extract processable information from the numerous images captured using several high-speed cameras. The programs are built from modular subfunctions for image and data processing. The main function manages all modules' information centrally for different measurement series and stores them together with the metadata in a structured library. The stored metadata includes all sensor data acquired besides the processed image information as temperature, humidity, acceleration, substrates, lens configuration, height, volume, measurement identification number. From those, it automatically calculates the corresponding liquid properties, as explained in §2.1.2.

2.2.1 Processing of Side-View Images

When evaluating the image data recorded from the side view, images with strong contrasts and a uniform background are available due to the telecentric optical system, see figure 2.12. Therefore, no background subtraction and contrast enhancement are necessary.

First, the lower substrates' acceleration is controlled. For this purpose, the two substrate surfaces must be detected and tracked. This can be quickly estimated by summing the gray levels per line due to the liquid bridge being much smaller than the substrate radius. Lines with the largest number of pixels with gray levels should be detected with a similar number in two image areas, each over several lines. In this way, the respective substrate surfaces are recognized, and the movement of the

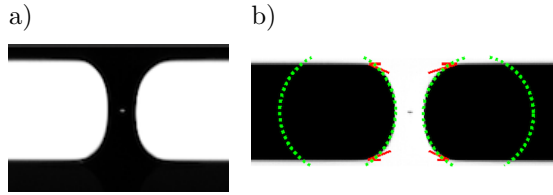


Figure 2.12: Side image taken from a bridge stretching measurement. In a) the image is shown before any post processing is performed. In b) the tracked contact angles and contour of the liquid bridge are used to display the contact angles and the best fitting curvature to the bridge contour.

lower substrate can be recorded.

Next, the contact line of the liquid bridge is tracked. For this purpose, a region of interest (ROI) is defined with the previously determined substrate surfaces, within which the full liquid bridge is located at all times. The height of the ROI is defined by the distance between the substrate surfaces and the width by the initial diameter of the liquid bridge. With knowledge of the substrate surface position, the bridge contour is easily extractable by subtracting the substrates and tracking the outer contours. Therefore, the primary bridge geometries: the upper bridge diameter D_U , the bridge diameter at the centerline D_M , and the bridge height H are tracked, as later shown in figure .

Within the ROI, the contact angles, inspired by the secant method [117], are determined with the help of two secants. The first secant is placed through the three-phase contact line and a second point on the contour of the liquid bridge. A second secant is positioned at the surface of the substrate. The inner angle between the two secants represents the contact angle. A comparison in [117] yields that the secant method is the most efficient and accurate compared to the polynomial edge fitting, local contour analysis, and intensity gradient statistic method.

To determine the contour of the bridge and curvature, an edge detection algorithm, Canny edge detection [118], and a line by line search are used. Based on the found profile, a curve with a constant curvature is defined, deviating least from the existing profile. The measured shape, the curvature, and the error are stored.

Figure 2.12 shows a stretching measurement with deionised water at

2 Experimental Methods and Procedures

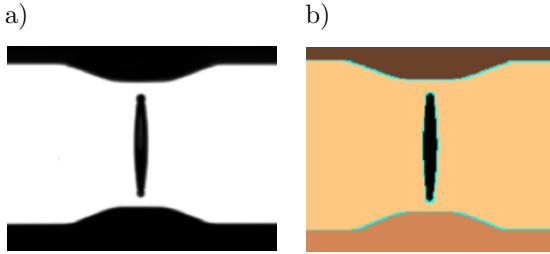


Figure 2.13: Side view image of bridge stretching after pinch-off at both sides. In a) the ROI of a raw image is shown, in b) the four different labels for top, middle, bottom and background are apparent.

an acceleration of 95 m/s^2 on glass substrates. In a), the ROI of the raw measurement image is shown before any post-processing is performed. The same image is shown in b) after the contact angles and contour of the liquid bridge are determined as described. Each contact angle is marked in red, and two green circles display the best fitting curvature to the bridge contour. The image is shown in b) is saved at every time step to verify the correct tracking.

The phenomenon of the bridge pinch-off is shown exemplarily in figure 2.13. To characterize the bridge breakup, every segment found by the edge detection algorithm within the ROI is labeled with a unique identifier. As soon as the bridge pinches-off at one point, the number of labels increases. This criterion is used to identify the event of the pinch-off. The pinch-off position can then be determined by finding the minimum distance between the newly emerged labels.

This method can also be extended to determine the filament length. To do this, the bridge pinch-off must have occurred at both substrates. Afterwards, the location of the pinch-off and the filament geometry can be determined. In figure 2.13a), the raw image and in b) the post-processed label image is shown. From figure 2.13b), it is easy to understand that four different labels are apparent for each enclosed segment, a new label. The four labels are the top substrate with the remaining liquid, the filament at the middle, the bottom substrate with the remaining liquid, and the background. It is easy to understand that the pinch-off instant is thereby obtainable by finding the time step when the number of labels gets larger

than two.

2.2.2 Processing of Top-View Images

The image data taken from top-view is not recorded with a telecentric optical system. Therefore, the contrasts are not that distinct as before and have to be enhanced. More efforts have to be placed into edge detection. Moreover, the bridge reaches different gray stages during the stretching, so the algorithm must be robust enough to detect the edges.

Finger Tracking and Effective Radius When investigating the effective radius for the pressure estimate in chapter 4, the reflection conditions change due to the moving lower substrate and, therefore, change the greyscale level of the contour on the fixed substrate. This makes the task of tracking the shape more difficult compared to the side view. For this purpose, the Lucas-Kanade optical flow method is used, which assumes that the movement between each time step is nearly constant in a local neighborhood and finds the relevant pixels using the least-squares method. This algorithm automatically selects the suitable pixels and tracks them independently using several consecutive images [119], [120]. The algorithm is implemented with Python, utilizing provided algorithms located in the OpenCV library. This method works well due to the contact line staying pinned and only the inner contour moving, as visible from figure 2.14 b).

Next, the effective radius is determined. Therefore, the center of mass of the inner contour is determined from the inner finger area. The retrieved midpoint is used as a reference point P_{CM} . With the fingers' contour and the midpoint P_{CM} , a minimal distance between those two can be obtained. This minimum distance is defined as the effective radius R_{eff} . In figure 2.14 a) the ROI of the raw image is shown. In b), the obtained R_{eff} in the form of a red circle and the contour obtained through the Lucas-Kanade algorithm is apparent.

Quantitative Characterization of the Finger Patterns The optical flow method, described above, allows to identify the finger patterns' contour. For further analysis, the images are post-processed with Python using the scikit-image library. The finger width is reduced to a line with 1 px width at the midline to quantify the number of fingers quickly. This process

2 Experimental Methods and Procedures

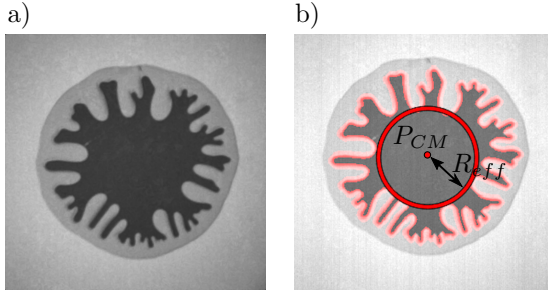


Figure 2.14: Top-view during finger formation of a *Gly80* during liquid bridge stretching. In a) the ROI of a raw image is shown in b) the tracked finger contour and effective radius R_{eff} are highlighted.

is called skeletonization. Different implementations of this method exist in the scikit-image library. For a 2D case, Zhangs [121] method is used, which allows to remove the outer pixels on the border of the object step by step. This is repeated until no further pixels can be removed, and only the skeleton of the image is left. In figure 2.15a), the ROI of the raw image and in 2.15b) the segmented finger pattern and the skeletonized image are shown.

Based on the received skeletonized pattern, the number of fingers in the border area can be quantified, counting the skeleton branches' ends. Critical cases are finger ends lying further inside the pattern. Only the finger ends in a range of 90% of the initial diameter are valid counts, whereas others are excluded from counting. This is done because the fingers start to emerge in the outer part. Therefore, the inner tips are not formed simultaneously and do not allow a conclusion about the instability formation of the outer tip emergence.

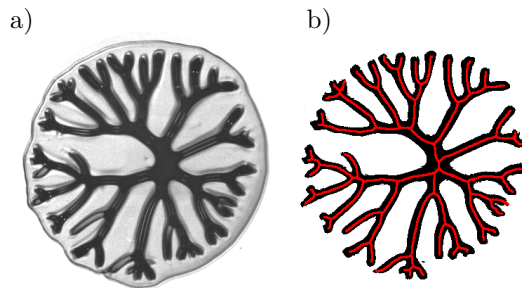


Figure 2.15: Top-view of finger formation of *Gly80* after pinch-off. In a) the ROI of a raw image is depicted and in b) the segmented finger pattern with its respective skeletonized structure is shown. Reprinted from [21] under CC BY 4.0.

3 Hydrodynamics of a Stretched Liquid Bridge

This chapter deals with the analysis of the kinematics of the bridge stretching. First, a phenomenological description during bridge stretching from the side view measurements is given. In the second part certain geometrical parameters as curvature, bridge diameter at the center and close to the substrate are investigated. The last part is based on the previous observations and introduces pressure estimations inside the liquid bridge at the center and the surface. Parts of the following sections have already been published [21, 22, 122, 123].

3.1 Phenomenological Description

The previously described experimental set-up allows shadowgraph images of the liquid bridge to be taken during the dynamic stretching process. A sample measurement series of 5 μl deionised water with substrate accelerations of 10, 90 and 180 m/s^2 is shown in figure 3.1. The liquid bridge deformation for low accelerations (10 m/s^2) is visible in the image sequence in the first row of the series: the bridge contour stretches vertically and constricts horizontally. This necking behavior can be analyzed through the curvature at the bridge surface. The necking continues until the bridge pinch-off sets in, and a small thread forms between the remaining volumes residing on the two substrates.

Comparing the different image sequences from figure 3.1, it becomes evident that with increasing acceleration, the liquid bridge is stretched for a longer distance before the first pinch-off occurs. After the pinch-off from both the upper and lower substrates, a liquid filament is formed between the two residual liquid drops. The length and width of the filament grow with increasing substrate acceleration, as apparent when comparing the first, second, and third row.

3 Hydrodynamics of a Stretched Liquid Bridge

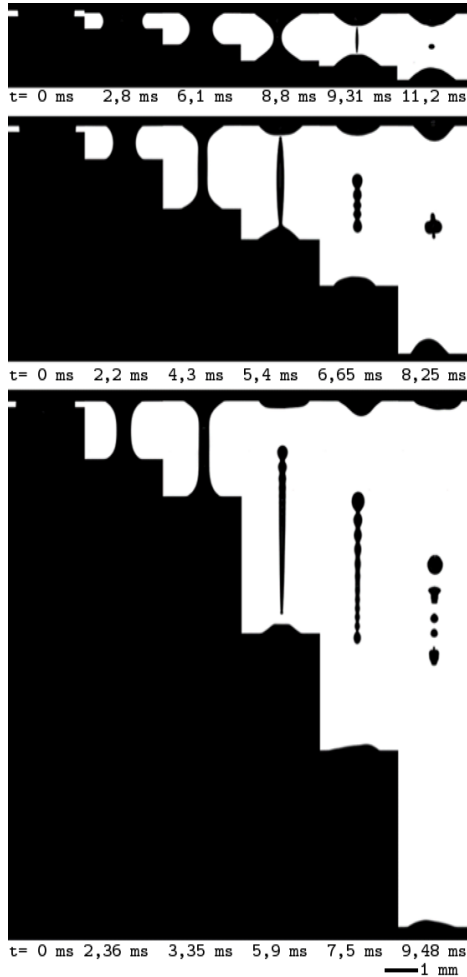


Figure 3.1: Stretching of liquid bridges consisting of $5 \mu\text{l}$ of deionized water with an acceleration of 10 m/s^2 in the first row, 90 m/s^2 in the second row and 180 m/s^2 in the third row. Reprinted from [22] under CC BY 4.0.

3.1 Phenomenological Description

Another occurrence in the higher acceleration sequence is the asymmetric deformation of the ligament heads. While the instants for the upper and lower pinch-off are nearly identical for 10 m/s^2 , they deviate in time from each other with increasing acceleration. For 90 m/s^2 , the ligament pinches-off at the top and bottom at nearly the same time and shows an almost synchronous formation of ligament heads with a pointed form. Shortly after the pinch-off time, the head forms to a drop-shaped head and starts to move towards the ligament center, reducing its length. At 6.55 ms , an instability begins to develop due to the slenderness of the free jet but does not lead to single drop formation. At 8.25 ms both, the top and bottom ligament head crash into each other and form a single drop.

Experiments of liquid bridges with accelerations of 180 m/s^2 start to pinch-off asynchronously at the top and bottom substrate. The first pinch-off happens at the stationary top substrate, and the vertical contraction starts from then onwards. Therefore, the described phases of the ligament formation start earlier at the top head and already shows the unstable profile at 5.9 ms , while the lower head is still showing a pointed silhouette. At 7.5 ms , the instability leads to distinguished cusps forming and first drops starting to pinch-off from the ligament. The drops at the top are larger than the ones forming at the bottom of the former ligament. The beginning of the sphere formation is similar to rim formation at the edge of a liquid sheet [27, 96]. For long ligaments, the cylindrical filament disintegrates into further spheres, as shown in the third row of figure 3.1, according to the Plateau-Rayleigh instability [124].

Experiments with the same experimental conditions except a more viscous liquid being used, a *Gly50* mixture, are shown in figure 3.2 with substrate accelerations of 10 , 90 and 180 m/s^2 in the first, second and third row. Compared to the experiments in figure 3.1, the liquid bridge height for similar accelerations becomes larger before the pinch-off starts. For 90 m/s^2 at 7.83 ms , in the second row, it becomes evident that the ligament is not showing any instabilities at all, compared to the measurements with water. No disintegration into single drops is occurring. Only a vertical contraction with spherical ligament heads at top and bottom can be observed. Therefore, the ligament has enough time to contract into a single drop, as long as the contraction is symmetric, and both heads bounce into each other. For 180 m/s^2 at 7.9 ms , the previously described asymmetry between the top and bottom head is also apparent for *Gly50*.

3 Hydrodynamics of a Stretched Liquid Bridge

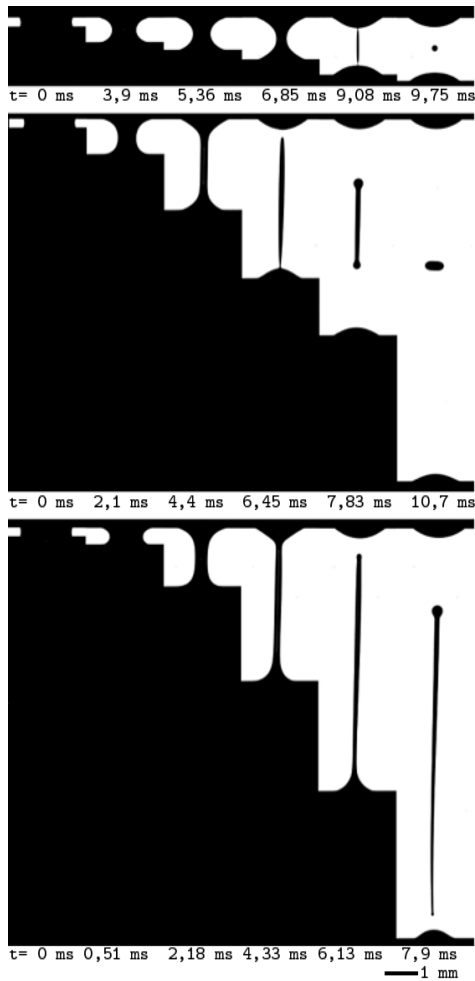


Figure 3.2: Stretching of liquid bridges consisting of 5 μl of *Gly50* mixture with an acceleration of 10 m/s^2 in the first row, 90 m/s^2 in the second row and 180 m/s^2 in the third row. Reprinted from [22] under CC BY 4.0.

3.2 Profile Investigation

In the following, the behavior of the curvature and distinguished bridge diameters are investigated.

3.2.1 Curvature

When investigating the entire side profile of the liquid bridge, a constant curvature is recognizable but only in the very early phase of the stretching process. This curvature, also seen in figures 3.1 and 3.2, is examined in greater detail below.

At the beginning of the stretching process, a constant radius of the vertical liquid bridge curvature can be observed over the full height on both sides. Therefore, the curvature $\kappa = 1/r_c$ is introduced with a radius of the curvature r_c , which is determined experimentally from the measured profile, as shown in figure 3.4. The measured mean curvature radius for different accelerations is shown in figure 3.3 for *Gly80*, $\lambda = 0.3$ and for different accelerations. This graph is to be read from right to left, due to the initial height being small and the abscissa being defined as $2/H$. The dispensed fluid initially shows a high contact angle state due to the compression. After dispensing the liquid onto the substrate and bringing the substrate to the initial bridge height, the liquid is pressed axially and moves freely in the radial direction. The radial movement leads to an advancing contact angle θ . Therefore, a larger contact angle is observable than the liquid-substrate combination would show in a static contact angle experiment. This results in curvatures of $\kappa = 600$ at the beginning. Due to the contraction phase, the curvature starts to increase (decreasing curvature radius) until reaching up to $\kappa = 1500$. A linear decline can be observed after this point, showing a constant curvature with increasing bridge height. The first phase of curvature growth occurs due to the earlier applied compression during the application of the liquid and the accompanying advancing contact angle. Until the initial conditions are overcome, a non-linear curvature growth is visible. After reaching the maximum curvature, the bridge seems to be in balance and follows equation (3.1), represented as a diagonal line in figure 3.3 .

$$\kappa = 2/H. \tag{3.1}$$

3 Hydrodynamics of a Stretched Liquid Bridge

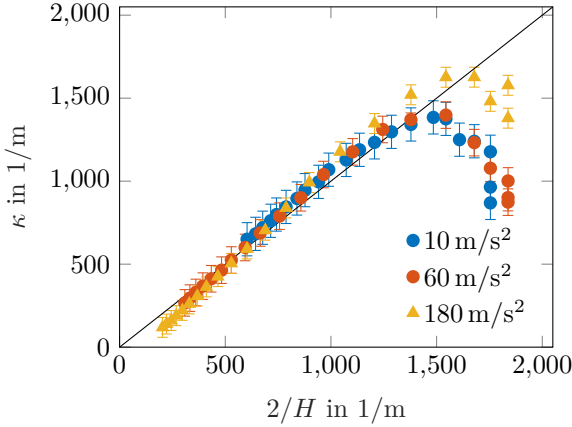


Figure 3.3: Evolution of the curvature and reciprocal height ratio for Gly80, $\lambda = 0.3$ and different accelerations. The data points are from the constant curvature section. Reprinted from [123] under CC BY 4.0.

After a certain period, the bridge loses its constant curvature over the bridge height and is no longer considered in figure 3.3. At the end of the measured data points, the profile could not be represented by a constant curvature anymore due to the shape deviating too much from a uniform curvature pattern. The effect of acceleration seems to be negligible concerning the curvature of the bridge. Only at the beginning, higher accelerations show a higher maximum value of the curvature.

The sketch figure 3.4 illustrates the three stages of curvature growth. In the first stage, the bridge curvature is smaller due to the initial compressed conditions of the bridge and the resulting advancing contact angle, as shown for t_1 . The curvature is increasing, starting from the initial ($2/H = 1750 \text{ 1/m}$) to the compressed state ($2/H = 1500 \text{ 1/m}$) with an increasing curvature from $\kappa = 1000 \text{ 1/m}$ to $\kappa = 1500 \text{ 1/m}$, indicated through the smaller radius r_c in figure 3.4 for t_2 . After reaching the maximum curvature, the curvature starts to follow the relation described in equation (3.1), shown for t_3 . The proportionality remains valid during further stretching until the necking no longer grows at the same rate as the bridge height. The radius of curvature begins slowly to deviate from equation (3.1) when stretched further. The evolution of these three stages

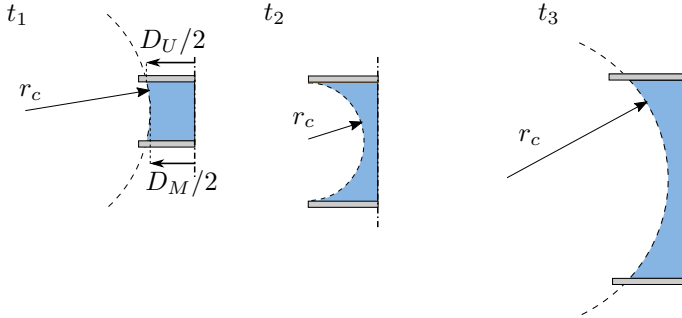


Figure 3.4: Evolution of the liquid bridge curvature radius r_c during expansion. Showing a larger curvature radius at the beginning for t_1 an decreasing curvature radius due to necking for t_2 and increasing curvature radius as a result of the increasing vertical substrate distance for t_3 . This is only valid during the first phase of the liquid bridge stretching.

can also be found in figure 3.3. The midpoint diameters and curvatures' proportionality coincide for the three different accelerations, as visible from figure 3.3. Only the relative height of the deviation onset is reached earlier for 10 m/s^2 than for 180 m/s^2 , apparent through the position of the last markers. After leaving the first phase of constant curvature, the surface force is no longer dominating the profile formation. The bridge midsection is starting to form a cylindrical jet with not clear curvature observable.

3.2.2 Centreline Profile

During liquid bridge expansion, two distinctive diameters are easy to describe and reproduce. Firstly the diameter D_M , which is located at the midline between the upper and lower substrate. The other one is the upper diameter of D_U close to the upper substrate. The position of both diameters can be viewed in figure 3.4.

The midpoint diameter evolution with varying viscosities μ , accelerations a and a fixed dimensionless height $\lambda = 0.09$ is shown in figure 3.5. The presented curves end with the bridge pinch-off. The dimensionless height λ is a geometric parameter depending on the initial liquid bridge

3 Hydrodynamics of a Stretched Liquid Bridge

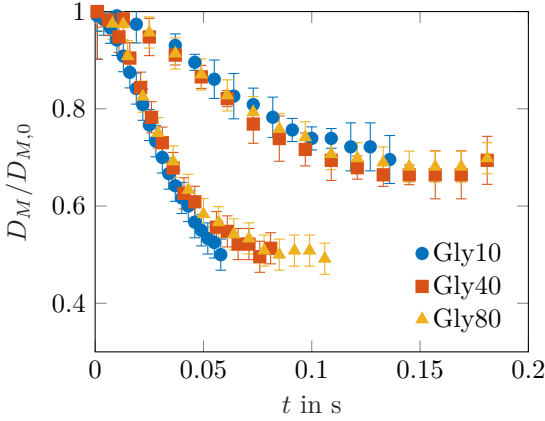


Figure 3.5: Evolution of the midpoint diameter comparing different viscosities and $\lambda = 0.09$ with an acceleration 180 m/s^2 in the lower curve array and for 10 m/s^2 in the upper curve array. Reprinted from [22] under CC BY 4.0.

height H_0 and the initial midpoint diameter D_0 . Two array of curves are apparent, the upper one is showing measurements for $a = 10 \text{ m/s}^2$ and the lower one for $a = 180 \text{ m/s}^2$. Initially, both arrays start at $D_M/D_{M,0} = 1$, and decrease over time. For the upper curve array with lower accelerations, the evolution of the midpoint diameter becomes flatter, but they exist longer in time. The more viscous the liquids are, the longer it takes until the bridge pinches-off, apparent through the shown data points for *Gly40* and *Gly80* for $t > 0.15 \text{ s}$. With higher substrate acceleration, the midpoint diameter decreases faster, and the pinch-off is occurring earlier in comparison. Within the investigated viscosity range ($1 \text{ mPas} < \mu < 40 \text{ mPas}$) in the form of *Gly10*, *Gly40*, and *Gly80*, the influence of viscosity on the midpoint diameter appears to be negligible. The evolution of the midpoint diameter can be considered as equal, as apparent from figure. 3.5. The acceleration is the dominant parameter compared to viscosity.

In figure 3.6 a comparison of different dimensionless heights and the same acceleration of $a = 180 \text{ m/s}^2$ are presented. Two array of curves are apparent, the upper one shows measurements with smaller heights and wider diameters with $\lambda = 0.09$ and the lower one with larger heights and

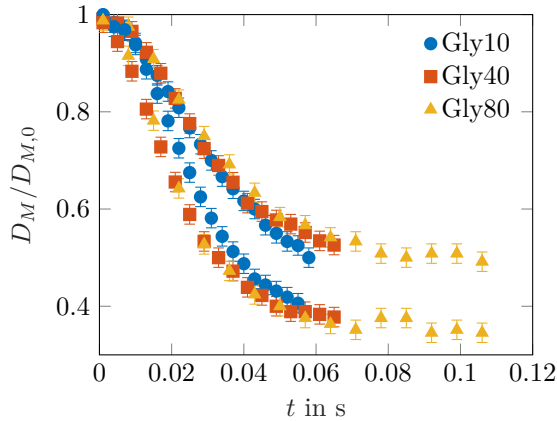


Figure 3.6: Evolution of the midpoint diameter comparing non-dimensional initial bridge geometries $\lambda = 0.3$ in the lower curve array and for $\lambda = 0.09$ in the upper curve array for substrate accelerations 180 m/s^2 and different viscosities. Reprinted from [22] under CC BY 4.0.

smaller diameters with $\lambda = 0.3$. Again measurements for three different liquids: *Gly10*, *Gly40* and *Gly80* are added in order to get a comparison of viscosity effects and the dimensionless height λ regarding the diameter evolution. Both curve arrays develop rather similar, only the curves for the larger bridge heights $\lambda = 0.3$ shows a steeper decline for $D_M/D_{M,0}$. This occurs due to the initial distribution of the volume: larger starting height and smaller diameter of the bridge. This allows a faster contraction to the upper and lower areas and therefore, less volume at the middle line. Different dimensionless heights show a noticeable difference in the diameter evolution, but behave comparable in each evolution to some degree.

3.2.3 Meniscus Profile

When studying the side profile of the liquid bridge during stretching, a deformation of the meniscus is apparent. During the stretching process, the meniscus profile and, therefore, the bridge diameter changes. The side macroscopic profile is analyzed first in the following section based on

3 Hydrodynamics of a Stretched Liquid Bridge

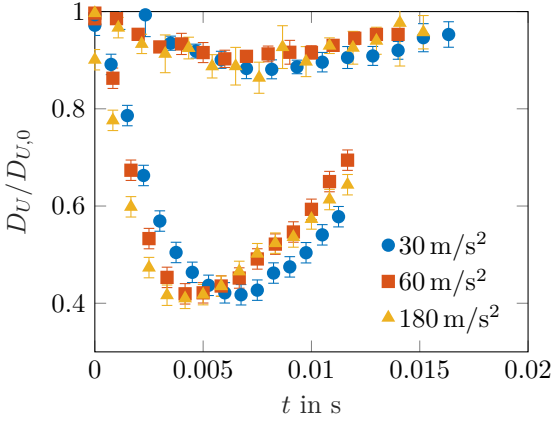


Figure 3.7: Evolution of contact line diameter of *Gly80* comparing substrate accelerations 30, 60 and for 180 m/s² for $\lambda = 0.3$ in the upper curve array and $\lambda = 0.09$ in the lower curve array. Reprinted from [123] under CC BY 4.0.

side view experiments. In the second part, the three-phase contact line is discussed based mainly on top-view measurements.

Macroscopic Lateral Meniscus Profile The following discussions use side bridge profiles measured during the stretching process, as shown in figure 3.1 and 3.2. The diameter close to the upper substrate is analyzed during the deformation of the meniscus profile. In figure 3.7, six different measurement series are grouped into two curve arrays. The upper curve array represents measurements with a dimensionless height of $\lambda = 0.3$ and the lower one at $\lambda = 0.09$. The measurements are shown for different accelerations $a = 30, 60$ and 180 m/s^2 with the same liquid *Gly80*.

The evolution of the ratio $D_U/D_{U,0}$ shows the simultaneous movement of the upper diameter D_U as soon as the lower substrate begins its downward motion ($t = 0 \text{ ms}$). It is apparent from figure 3.7 that the ratio $D_U/D_{U,0}$ decreases faster for smaller values of λ down to 40%. Due to the increased diameter contraction speed, the dimensionless minimum upper diameter $D_{U,\min}/D_{U,0}$ exhibits an overall difference in the decline by 50% only through smaller λ values. For the larger bridges, only retractions down to 90% of the initial diameter are observable. The measurements

with different accelerations but constant λ differ little, due to the different substrate accelerations. The $D_{U,\min}/D_{U,0}$ ratio is independent of the substrate acceleration. The effect of the liquid viscosity is similar on $D_U/D_{U,0}$ as shown for the midpoint diameter in figure 3.5. After reaching a minimum value, both curve arrays have in common that the ratio of $D_U/D_{U,0}$ starts to increase again. This occurs after the bridge pinches-off, and the drop dynamics lead to deformations effects until a new stationary form is found. After the stationary position is reached, the absolute drop diameters D_U of both curve arrays are similar for the investigated parameters [125].

The ratio of the contracting diameter D_U to middle line diameter D_M is shown in figure 3.8 as a function of the stretching motion as H/D_0 . D_0 is the initial diameter at $t=0$, which is the same at both positions $D_M(t=0) = D_U(t=0) = D_0$, due to an advancing contact angle. The advancing contact angle occurs during the initialization of the liquid bridge height, where the two substrates are moved towards each other after the liquid is applied. As already explained for the curvature description, the contact angle is larger due to the initial compressed state leading to an advancing contact angle. The measurements in figure 3.8 were performed with *Gly80*, an acceleration of 180 m/s^2 and data points are shown until pinch-off occurs. The initial ratio of D_U/D_M starts at 1 for different dimensionless heights shown $\lambda = 0.018, 0.134$ and 0.19 . With further stretching, the values of D_U and D_M deviate up to a ratio $D_U/D_M \approx 2.1$ for the smallest investigated bridges. The initial bridge geometry leads to a steeper inclination for smaller bridges and an increasing diameter ratio at pinch-off. It is also apparent that for larger λ , the bridge stretches longer until it pinches-off.

The evolution of the diameter at the center line and the height of the liquid bridge are investigated. With the constant mass condition, the relation is shown in equation (3.2) is approximated. The liquid bridge volume is compared with the evolution of D_M and H scaled by their initial values $D_{M,0}$ and H_0 . In figure 3.9 the dashed line represents the relation of equation (3.2). Measurements with different dimensionless heights λ are plotted and indicate a good representation down to $H_0/H = 4$ for different λ . The midpoint diameter starts to deviate, beginning with larger initial bridge geometries $\lambda = 0.19$ from the described proportionality. One reason for the deviation occurring only for larger λ is that the flow regime is altered entirely. For larger λ , only a small radial contraction is apparent, and therefore the radial flow is only minimal compared to the smaller

3 Hydrodynamics of a Stretched Liquid Bridge

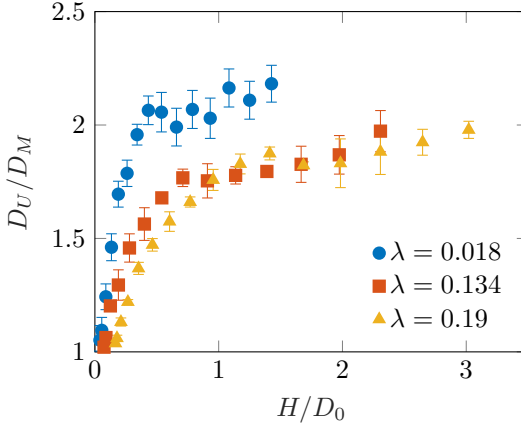


Figure 3.8: Evolution of the contact line diameter to midpoint diameter ratio up to pinch-off of the liquid bridge. The measurements were performed with Gly80 and 180 m/s^2 for different λ values. Adapted from [123] under CC BY 4.0.

λ , see figure 3.7. The liquid bridge pinch off length also affects the midpoint diameter, due to the bridge being longer for larger λ . Therefore the timescale for the mass compensation between the midpoint and meniscus area is longer. Consequently, the curves deviate from the ideal correlation further as the expansion progresses. The approximation is more accurate for smaller dimensionless heights λ , as apparent from measurements with $\lambda = 0.018$.

$$D_M/D_{M,0} = \sqrt{H_0/H}. \quad (3.2)$$

The effect of the viscosity on the evolution of the scaled bridge diameter D_M/D_0 is shown in figure 3.10. The reference measurement series is performed with $a = 180 \text{ m/s}^2$ and an initial gap ratio of $\lambda = 0.05$. Up to around $H/H_0 = 7.5$, the estimated behavior coincides well with the experimentally determined data. From there on after a deviation for the *Gly80* measurement series is observable. A good agreement with the predicted equation (3.2) can be confirmed, and the effect of viscosity is negligible for small bridges with high accelerations, as shown by [126].

In figure 3.11, the effect of accelerations on the evolution of the scaled

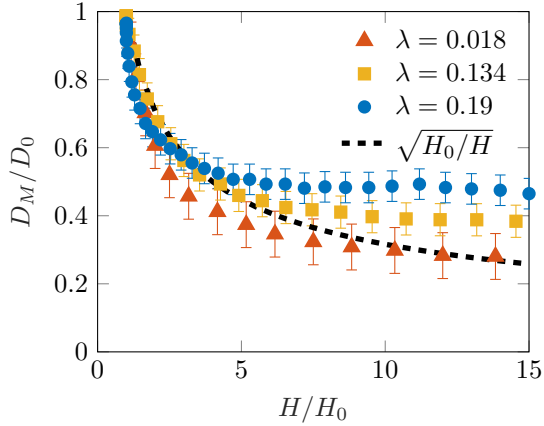


Figure 3.9: Evolution of the midpoint diameter and the inverse height derived from mass continuity, see equation (3.2). Measurements were performed with Gly80, 180 m/s^2 for different parameters of λ . Adapted from [123] under CC BY 4.0.

bridge diameter during stretching is shown as a function of the dimensionless gap width. The diameter follows the expected development described in equation (3.2). For a lower acceleration, the pinch-off occurs much earlier compared to measurements with higher accelerations. The prediction in the equation (3.2) is universal, and it does not depend on liquid properties or the substrate acceleration, as shown before. The evolution of the bridge diameter can be approximated when $H \ll D_M$.

Three Phase Contact Line When observing the diameter contraction close to the substrate surface, a contracting diameter can be noticed close to the substrate, previously introduced as D_U . However, when comparing the time scale of the contraction speed of D_U and literature values of typical dewetting phenomena with similar liquid properties, it is noticeable that the dewetting time scales are several magnitudes larger compared to the measured contraction time scale [104]. Therefore it is evident that the contracting diameter D_U is different from the contact line diameter D_{CL} . To investigate this further, measurements were performed with an additional second high-speed system providing a top view of the liquid bridge to record the three-phase contact line. The transition from moving

3 Hydrodynamics of a Stretched Liquid Bridge

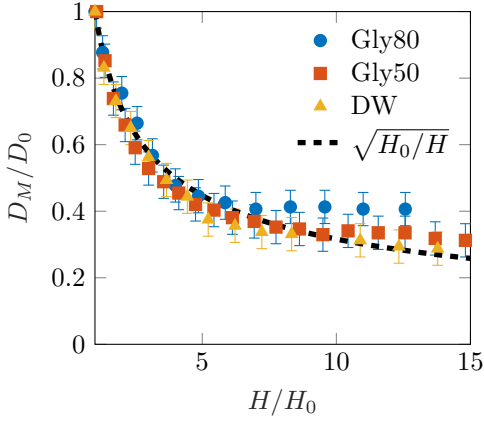


Figure 3.10: Initial jet stretching. The diameter ratio as a function the height ratio H/H_0 for a substrate acceleration of $a = 180 \text{ m/s}^2$ and initial gap thickness $\lambda = 0.05$ for different viscosities. The experimental data are compared with the theoretical predictions from eq. 6.1. Adapted from [123] under CC BY 4.0.

to pinned contact lines with higher stretching rates is known from other studies [127, 127, 128], but was not investigated for accelerations of this magnitude.

Figure 3.12 shows an image series of liquid bridge expansion from top with a dimensionless height $\lambda = 0.0151$, a liquid *Gly80* and an acceleration of 180 m/s^2 . It is apparent that the three-phase contact line stays pinned at the initial position during the stretching process from 0 ms to the end at 11 ms. Additionally, a further distinctive feature can be observed beginning from 2.1 ms, two distinct areas are formed, recognizable by different grey tones. The dark cylindrically shaped area contracts up to 3.7 ms and start to expand again from 7.3 ms onwards. After 11 ms, the two grey tones are almost similar again, as they were at the beginning. In combination with the results presented before, a comparison of the contraction of the dark cylindrical area is in the same order of size and speed as the diameter D_U . The shape measurements of D_U from the side and top perspectives are hard to compare due to the transition area in the top view showing a low contrast (11 ms). Therefore a quantitative measure-

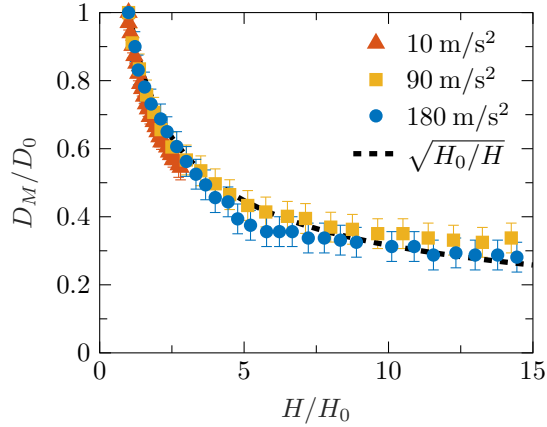


Figure 3.11: Evolution of the diameter of a liquid bridge. The scaled bridge middle diameter D_M/D_0 as a function of the dimensionless gap width H/H_0 for various substrate accelerations. The curve corresponds to the predictions based on (3.4). Adapted from [21] under CC BY 4.0.

ment of the diameter is not possible from the top perspective. From this observation, it is apparent that the diameter D_U does not correspond to the three-phase contact line. The previously observed diameter D_U is an apparent receding meniscus moving on a thin residual film. Further, it is apparent that an inner ring at 7.3 ms is visible; this is the result of a total internal reflection of the coaxial illumination from the inside of the liquid bridge.

The behavior of the three-phase contact line and the thin film are sketched in the figure 3.13 for a better understanding of three chronological points in time $t_1 < t_2 < t_3$. At the beginning at t_1 , the three-phase contact line is in its initial state $D_{CL} = D_U$. In this phase, the three-phase contact line coincides with the visible meniscus in the side profile. At t_2 , the lower substrate started to move, therefore, the stretching of the bridge has begun. The movement leads to a contraction of the bridge apparent in the form of D_U . Here D_U does not capture the three-phase contact line itself, but the contour of the meniscus profile nearby. The contact line remains pinned at the initial position D_{CL} . It is also recognizable in t_2 that the apparent meniscus angle is formed on a thin residual film.

3 Hydrodynamics of a Stretched Liquid Bridge

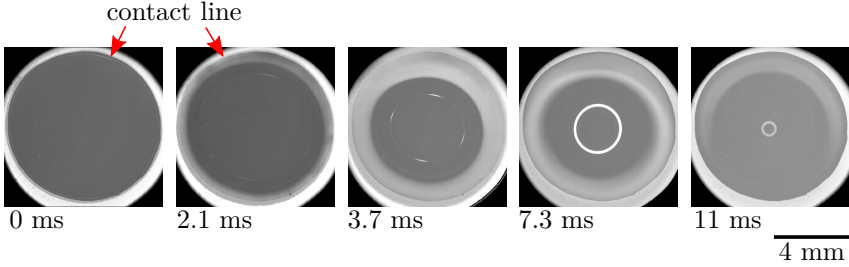


Figure 3.12: Top-view of the liquid bridge stretching shown pinned contact line, residual film, and moving inner meniscus. The measurement was performed with a dimensionless height of $\lambda = 0.0151$, with *Gly80* and an acceleration of 180 m/s^2 .

Therefore it is not comparable to a typical contact angle configuration. At the time t_3 , the bridge contraction has progressed, and the residual layer is distinguished. Following on from figure 3.12, the residual layer is recognizable as a bright area, and the apparent meniscus angle is formed in the transition area between the bright and dark area with $D_{CL} > D_U$. After a long time, $t_4 \gg t_3$ when the bridge has pinched-off, and the dewetting process has finished, the remaining liquid volume shows a drop formed shaped due to the surface forces. The contact line had enough time to recede, and the residual layer vanishes so that again $D_{CL} = D_U$.

The reason for the clear distinction of the two grey tones in figure 3.12 results from the almost parallel free surface of the residual layer, as shown in figure 3.13. In the outer section, the incident rays are reflected partially back and appear brighter. In the inner bridges section, the rays are deflected in different directions due to the curvature, and therefore, only some light rays are reflected onto the sensor of the camera. Consequently, the inner section appears darker. After liquid bridge pinch-off, the residual liquid takes a drop-shaped form with an even curvature. There the brightness curve is equalized, and no different contours can be observed anymore.

Different attempts to display the thin film experimentally in side view were performed, one of them is shown in figure 3.14 with $\lambda = 0.0171$, 180 m/s^2 and *Gly80*. In this case, the meniscus is examined with a telecentric lens system and a magnification factor of four. Due to the

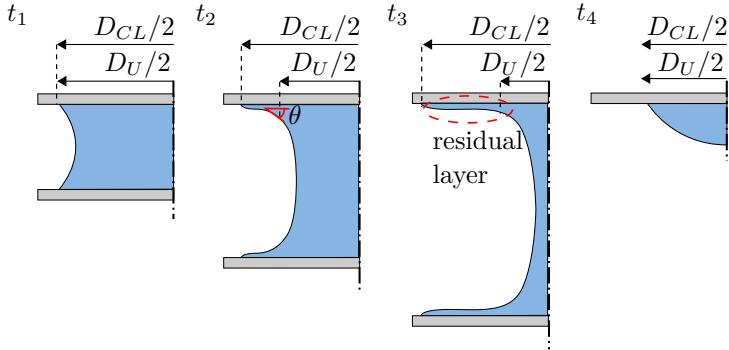


Figure 3.13: Sketch of the residual layer evolution at four time steps $t_1 < t_2 < t_3 \ll t_4$. The contact line stays pinned up to t_3 and starts move until t_4 . An apparent meniscus angle forms at the contracting residual layer.

smallness of the gap, the bridge is only recordable after 2.4 ms, when the residual layer already has been formed. The residual layer itself could not be detected from the beginning due to geometrical constrictions. The image series also gives information about how the apparent meniscus angle is deforming during the late phase of the stretching phase. At 5.6 ms, a clear distinction of the uneven profile contour is visible from the meniscus to the residual layer. Shortly after the pinch-off of the liquid bridge at 9.9 ms, a drop is formed at the middle part and is spreading over the residual layer. Based on the resolution of the lens, it can be estimated that the height of the residual layer is of the order of a few μm . Measurements using commercially available point interferometers and chromatic wave line sensors could not validate the film thickness due to the small length and short time scale requirements.

From previous measurement series in figure 3.12, it was already evident that the three-phase contact line remains pinned during bridge expansion and has no influence on bridge expansion itself. Additionally, the measurement series are shown in figure 3.15 illustrates the different time scales of bridge elongation and dewetting, capturing the movement of the three-phase contact line. It shows a measurement series performed with *Gly80*, $\lambda = 0.0134$ and an acceleration of $a = 180 \text{ m/s}^2$ on a hydrophobic silanized coating on a glass substrate with a static contact angle of $\theta = 110^\circ$. From 0.2 ms onwards, two different grey tones are visible, which

3 Hydrodynamics of a Stretched Liquid Bridge

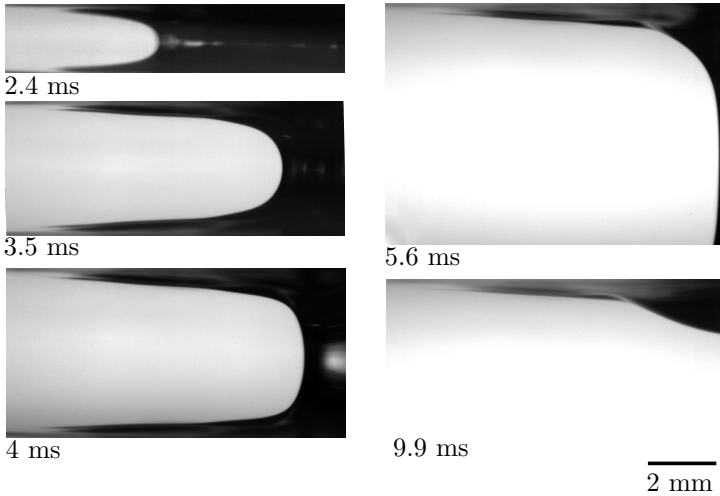


Figure 3.14: Side view of meniscus deformation during liquid bridge stretching performed with telecentric optical system. The shown stretching measurement was performed with $\lambda = 0.0171$, *Gly80* and an acceleration of 180 m/s^2 .

divide the bridge into a three-phase contact line and the inner part of the bridge. This measurement series additionally shows the occurrence of finger formation, discussed in greater detail in chapter 5. The residual layer is also visible between the formed fingers, suggesting that the finger formation forms on top of the residual layer. At 9.04 ms, it is apparent that the surface begins to homogenize again due to the surface forces. At 11.06 ms, it is recognizable that the grey tones are adapting to each other. After 21.04 ms, the beginning of the dewetting can be seen. In the series' last image at 457 ms, the liquid reached an equilibrium state, and the dewetting process is finished for the moment. It is obvious from the timestamps that the pinch-off has been completed well before the dewetting starts, compare to figures 3.1 and 3.2. Consequently, the dewetting process appears on a time scale two orders of magnitude larger than the finger formation.

The contact line diameter evolution D_{CL} during a liquid bridge stretching experiments is shown for two different wettability states in figure 3.16. The reference measurements were executed on hydrophobic silanized glass

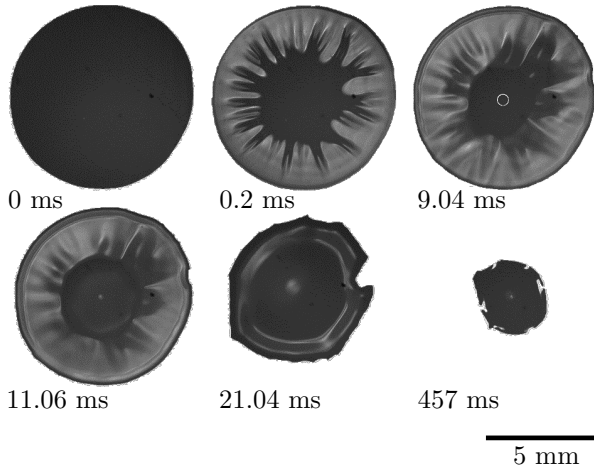


Figure 3.15: Sequence of the bottom views of the liquid bridge. The time associated with the finger formation (approximately 10^{-1} milliseconds) is two order of magnitude smaller than the time at which the dewetting process becomes notable, at approximately 20 milliseconds. Contact angles for the hydrophobic substrates are $\theta \approx 110^\circ$ for *Gly50* and *Gly80*. Reprinted from [21] under CC BY 4.0.

substrates with static contact angles of $\theta = 110^\circ$. The previous and most of the following measurements were conducted on quartz glass substrates with a static contact angle of 40° , also shown in figure 3.16. A reference measurement with a high contact angle was chosen to investigate the effect of a hydrophobic substrate on the liquid bridge stretching process. A higher contact angle directly results in a higher contact line speed following [129–132] a notable dewetting effect during the stretching process is more likely. From the measurement shown in figure 3.16, it can be concluded that the speed at which the contact line moves on the hydrophobic substrate is 12.1 ± 0.1 mm/s and on the glass substrate, it is 2.6 ± 0.1 mm/s with the same liquids. Both three-phase contact lines show a constant speed during the first phase until they lock at their respective final positions. The measurements were performed with two different $\lambda = 0.0164$ for 110° and $\lambda = 0.0111$ for 40° , as the initial diameter $D_{CL}(t = 0)$ suggests. At $t = 0$ s, the bridge stretching begins, and due to the scaling of

3 Hydrodynamics of a Stretched Liquid Bridge

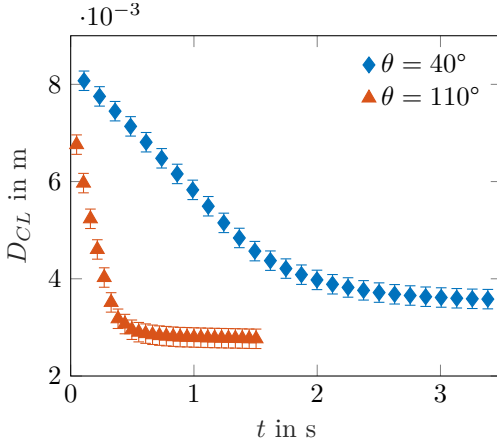


Figure 3.16: Showing the contact line evolution of two dewetting measurements. Measurement with $\theta = 110^\circ$ was performed with $\lambda = 0.0164$ and for $\theta = 40^\circ$ with $\lambda = 0.0111$. Both times *Gly80* was used and the substrate acceleration was 180 m/s^2 .

the x-axis, it seems that the dewetting starts simultaneously. For the hydrophobic substrate, the dewetting process is finished after 0.3 s, while for the glass substrate and a slightly larger bridge, the dewetting is finished after 1.5 s. Those agree with the observations from figure 3.15.

Apparent Meniscus Angle To better understand the bridge meniscus profile during contraction, the meniscus angle is analyzed in the following and compared to different bridge heights over time. In this study, the term meniscus angle refers to an apparent macroscopic angle moving on a thin residual liquid layer, as introduced before. It refers to the observed angle measured on a residual film and the meniscus of the contracting liquid bridge, as shown in figure 3.13. The three-phase contact line and its corresponding contact angle are not resolvable from the available side view measurements. The three-phase contact line movement is only observable through the top view of the optical system, as shown in the previous section.

Since the contour of the liquid bridge can be assumed to be symmetric, a mean apparent meniscus angle of the left and right side of the profile at the

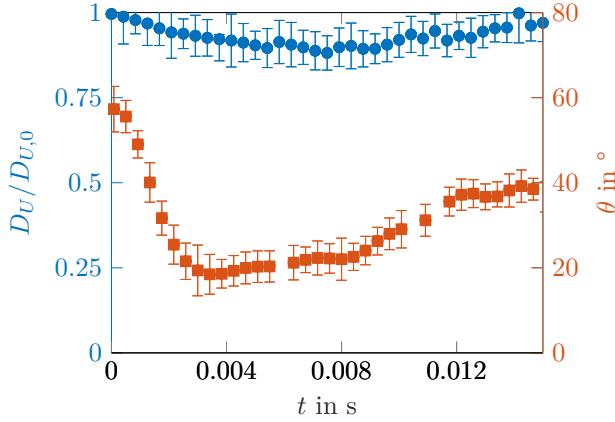


Figure 3.17: Comparison of the evolution of the contact line diameter $D_U/D_{U,0}$ with circle markers on the left scale vs. meniscus angle θ with square markers on the right scale. The experiments were performed with Gly80, 180 m/s^2 and $\lambda = 0.18$. Reprinted from [123] under CC BY 4.0.

upper surface substrate θ is introduced. The data shown in figure 3.17 was measured with *Gly80*, 180 m/s^2 and $\lambda = 0.18$. The left ordinate shows the diameter ratio of $D_U/D_{U,0}$ with the corresponding data points as circles. On the right ordinate, the measured meniscus angle is represented by data points in the form of rectangles. It can be seen that the initial meniscus angle is at $\theta \approx 60^\circ$ and falls below this value at $t = 4 \text{ ms}$ in the course of the bridge expansion. After the initially strong decrease, a relaxation can be seen, leading to a slow increase and finally ends at the static meniscus angle of 40° . Compared to the deformation of the bridge diameter, it is noticeable that the meniscus angle and the bridge decrease simultaneously.

In comparison, in figure 3.18, a series of measurements with smaller bridge heights, $\lambda = 0.09$, but otherwise equal parameters is presented. The liquid used is *Gly80* and the substrate acceleration 180 m/s^2 . The graph has the same abscissa and ordinate as before. For the smaller bridge, it is already known that the bridge diameter contracts further and, after reaching the minimum, does not go back to the initial value on the shown time scale. The initial meniscus angle is difficult to measure for

3 Hydrodynamics of a Stretched Liquid Bridge

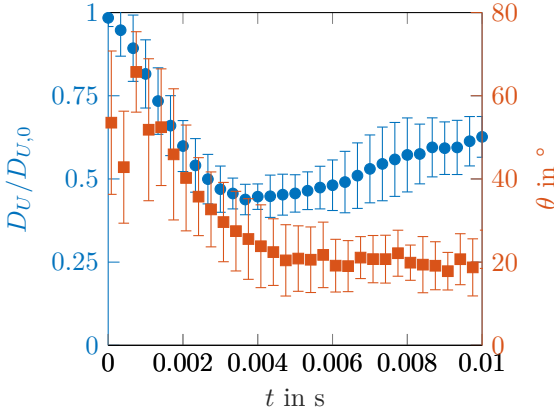


Figure 3.18: Comparison of the evolution of the contact line diameter $D_U/D_{U,0}$ with circle markers on the left scale vs. meniscus angle θ with square markers on the right scale. The experiments were performed with Gly80, 180 m/s^2 and $\lambda = 0.09$. Reprinted from [123] under CC BY 4.0.

smaller bridges due to the small substrate distance, recognizable by the error bars' size but is in the order of $\theta \approx 40 - 60^\circ$. With the beginning of the bridge expansion, the meniscus angle also decreases. After about $t = 5\text{ ms}$ the minimum of $D_U/D_{U,0}$ is reached at $\theta \approx 20^\circ$. In contrast to the behavior observed before, the meniscus angle remains at this level.

It is apparent that in both cases, the meniscus angle decreases to a minimum value of approximately 20° . After reaching θ_{\min} , the meniscus angle starts to increase again as also observable for $D_U/D_{U,0}$. However, the meniscus angle growth starts earlier than the contact line diameter contraction.

The effect of different accelerations and their effect on the meniscus angle evolution θ over time is shown in figure 3.19 for *Gly80*, $\lambda = 0.3$ and accelerations of 10 , 60 and 180 m/s^2 . For all measurements, the meniscus angle is increased at the beginning due to the compressed state, as explained earlier. The evolution of θ exhibits a steeper decline for higher accelerations until the curves reach a minimum θ_{\min} . The minimum meniscus angle is of the order $\theta_{\min} = 19 \pm 1^\circ$. This θ_{\min} agrees with the receding contact angle measured with a *KRÜSS DSA 100* system on the

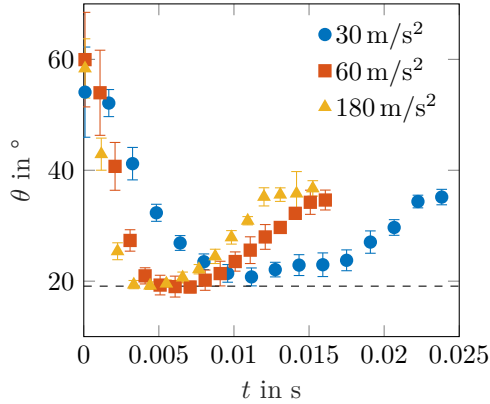


Figure 3.19: Evolution of meniscus angle of Gly80 comparing substrate accelerations 30, 60 and 180 m/s^2 for $\lambda = 0.3$. The dashed line indicates the measured receding meniscus angle. Reprinted from [123] under CC BY 4.0.

fluid/substrate combination. Even though the meniscus angle appears on top of the residual film and, therefore, in a completely different regime. After the θ_{\min} is reached, the meniscus angle increases. The increase continues until shortly before the liquid bridge breaks at the meniscus region.

The meniscus angle evolution is compared with the capillary number $Ca_{CL} = U\mu\sigma^{-1}$, where U is the horizontal contraction speed of the diameter D_U in figure 3.20. The capillary number starts from the initial state $Ca_{CL} = 0$ and decreases down to a meniscus angle of $\theta = 40^\circ$. Depending on the acceleration, a minimum of $Ca_{CL} \approx -0.09$ is reached for 180 m/s^2 . The diameter contraction speed then increases up to $Ca_{CL} = 0$ and even further for some measurements. The meniscus angle does not drop below θ_{\min} , as shown previously.

3.3 Pressure Distribution

To further understand the flow in the liquid bridge, a knowledge of the pressure field is required. The pressure distribution in the gap can not be determined experimentally. Nevertheless, a lubrication approximation

3 Hydrodynamics of a Stretched Liquid Bridge

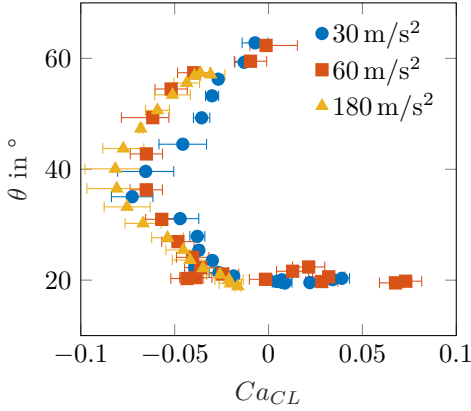


Figure 3.20: Evolution of the capillary number $Ca_{CL} = U\mu\sigma^{-1}$ and the related meniscus angles. Measurements were performed with Gly80 and a dimensionless height $\lambda = 0.1$. Reprinted from [123] under CC BY 4.0.

can be used to estimate the pressure distribution, governed by the viscous effects, surface tension, and inertia.

The flow field in the stretching liquid bridge can be subdivided into two main regions: the meniscus region and the central, inner region, which is not influenced by the meniscus. The solution for an axisymmetric creeping flow between two parallel substrates, one of which moves, is well-known [133]. The axial and the radial components of the velocity field are

$$u_{0,r} = -\frac{3\dot{H}rz}{H^2} \left(1 - \frac{z}{H}\right), \quad u_{0,z} = \frac{3\dot{H}z^2}{H^2} \left(1 - \frac{2z}{3H}\right). \quad (3.3)$$

This velocity field satisfies the equation of continuity, the momentum balance equation, and the kinematic conditions at both substrates. Unfortunately, this solution does not apply to the case when the effect of the substrate acceleration becomes significantly high. Moreover, the expression for the velocity field between two substrates (3.3) is not applicable at the interface of the meniscus. It does not satisfy the conditions for the pressure at the interface, determined by the Young-Laplace equation, and it does not meet the requirements of zero shear stress at this interface. Moreover, this velocity field is not able to accurately predict the rate of

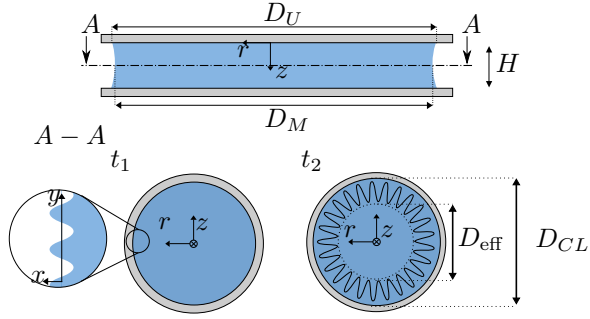


Figure 3.21: A sketch of a liquid bridge from a side view and from top view at two different stages t_1, t_2 . A cylindrical frame of reference is used at the symmetry axis (r, z) . The relevant diameters for the following analysis are: D_U , D_M and the effective diameter D_{eff} . The top view is shown for t_1 at which the finger instability starts to form and t_2 with a pronounced finger pattern. A Cartesian frame of reference is used at the instability front at t_1 (x, y) . Adapted from [21] under CC BY 4.0.

change of the meniscus radius of \dot{R} . Assuming the rate change of the minimum meniscus radius at the middle plane as $\dot{R} = u_{0,r}$ at $z = H/2$, and with the help of (3.3), the solution of the equation for the meniscus propagation becomes $R = R_0(H_0/H)^{3/16}$. This solution does not agree with the experimental data for the evolution of the meniscus radius. Therefore, the flow in the meniscus region has to be treated differently.

An expression for the radius and the height can be derived from the overall mass balance, where the initial thickness is H_0 , the initial radius is R_0 and the lower substrate moves with a constant acceleration a . The radius of the bridge meniscus, R , can be estimated as

$$R = R_0 \left[\frac{H_0}{H} \right]^{1/2}, \quad H = H_0 + \frac{at^2}{2}, \quad (3.4)$$

which gives a valid estimate for the initial times, when $R \gg H$, as demonstrated on the graph in fig. 3.11. As mentioned before, R_0 can be approximated for $t = 0$ as $D_U/2 = D_M/2 = R_0$, for later time steps R corresponds to $D_M/2 = R$, see figure 3.21.

3 Hydrodynamics of a Stretched Liquid Bridge

The flow in the meniscus region has to be treated separately. This flow must satisfy the boundary conditions at the curved meniscus interface and include the corner flows at the meniscus region [134, 135]. The model of the meniscus flow is not trivial and can lead to multiple solutions [136]. However, an accurate solution for the meniscus stability problem must be based on the meniscus velocity field, since the stresses in this region govern the meniscus instability.

3.3.1 Pressure Field in a Creeping Flow in a Thin Gap

A pressure estimate for the inner region close to the surface of the substrate is estimated based on the viscous and surface forces applied to the liquid bridge. For simplicity, the inertial terms are neglected in a first approach.

The velocity profile of the bridge is assumed to be in a parabolic form as used in Darcy's gap-averaged law [71, 73, 137, 138], which is a valid analogy for a two dimensional viscous flow between two substrates assuming a permeability of $k = b^2/12$ [61].

However, this assumption is only valid for the case $\lambda \ll 1$, since the ratio of the axial to radial velocity is comparable to λ . The influence of the axial velocity on the pressure gradient is consequently negligible. A coordinate system, according to figure 3.21 has been chosen. Therefore, u_r is in the form of

$$u_r = r(bz + cz^2), \quad (3.5)$$

where z is the bridge height and r is the radius. With the help of the continuity equation the axial velocity is derived as

$$u_z = -1/r \int_0^z \frac{\partial u_r}{\partial r} dz. \quad (3.6)$$

For z being the liquid bridge height H and the constraints that $u_r(z = H) = 0$, due to the previously observed fixed contact line and $u_z(z = H) = H'(t)$ for the substrate movement. This leads to

$$b = -\frac{3H'}{H^2}, \quad c = \frac{3H'}{H^3}. \quad (3.7)$$

With the previously derived equations (3.5-3.7) the radial velocity can be estimated in the form of

$$u_r = \frac{3rzH'}{H^2} \left(1 - \frac{z}{H}\right). \quad (3.8)$$

With the help of equation (3.8) at $z = 0$ and the Navier-Stokes equation with only the viscous terms in radial direction considered, the pressure gradient can be estimated to be:

$$\frac{\partial p}{\partial r} = \eta \left(\frac{\partial}{\partial r} \frac{1}{r} \frac{\partial u_r}{\partial r} + \frac{\partial^2 u_r}{\partial z^2} \right) = \frac{6\eta r H'}{H^3}. \quad (3.9)$$

Integrating the pressure gradient leads to a pressure estimate. The pressure is evaluated at the midpoint $r = 0$. In which the height change can be expressed with the help of the substrate acceleration

$$H = H_0 + \frac{at^2}{2}, \quad H' = at, \quad (3.10)$$

and R_{eff} , being the effective radii of the liquid bridge, see figure 3.13, gives a pressure estimate of

$$p = -3\mu a \frac{R_{\text{eff}}^2 t}{\left(H_0 + \frac{at^2}{2}\right)^3}. \quad (3.11)$$

Equation (3.11) can be extended by the Laplace pressure as follows, which takes into account the surface forces that counteract with the bridge elongation and lead to a reduction in pressure

$$p_\sigma = -3\mu a \frac{R_{\text{eff}}^2 t}{\left(H_0 + \frac{at^2}{2}\right)^3} - \sigma \frac{2}{H_0}. \quad (3.12)$$

The knowledge on the pressure at the center of the gap $r = 0$ is required to describe the cavitation phenomena in chapter 4.

3.3.2 Pressure Distribution Accounting for the Inertia

At the surface of the bridge, it is assumed that the main reason for the surface instability is the appearance of a normal pressure gradient at the interface. This mechanism is analogous to the Rayleigh-Taylor instability, where the pressure gradient is caused by gravity or by the interface

3 Hydrodynamics of a Stretched Liquid Bridge

acceleration. This approximate solution is valid only for the case of a very small relative gap thickness, $\lambda \ll 1$. Note also that the ratio of the axial and radial components of the liquid velocity is comparable with λ . Therefore, the stresses associated with the axial flow are much smaller than those associated with the radial velocity component.

In the following, a pressure estimate at the liquid bridges interface is derived for the case of a very small relative gap thickness, $\lambda \ll 1$. Note also that during the early phase of the stretching process, the ratio of the axial and radial components of the liquid velocity is comparable with λ . Therefore, the stresses associated with the axial flow are much smaller than those associated with the radial velocity component.

Since only the dominant terms of the pressure gradient at the interface are considered, the pressure gradient includes the viscous stresses and the inertial terms associated with the material acceleration of the meniscus \ddot{R} . The approximation is based on the fact that the radial velocity in the liquid at the interface at the middle plane ($z = H/2$) is equal to \dot{R} . The value of the pressure gradient is then estimated from the Navier-Stokes equations with the help of (3.4) and the previously introduced equation at the surface but at $z = H/2$ in the form

$$p_{0,r} = -b\mu \frac{\dot{R}}{H^2} - \rho \ddot{R} = \mu atb \frac{\sqrt{H_0} R_0}{2H^{7/2}} + \rho a \frac{\sqrt{H_0} R_0}{2H^{5/2}} (H_0 - at^2), \quad (3.13)$$

where b is a dimensionless constant. Its value $b \approx 12$ can be roughly estimated approximating the velocity profile by a parabola, as in the gap-averaged Darcy's law [71, 73, 137, 138].

An approximation (3.13) is valid only for the cases of $\lambda \ll 1$ considered in this study. Since the ratio of the axial to the radial velocity, which can be estimated from (3.4), is comparable with λ , the effect of the axial velocity on the pressure gradient is negligibly small.

The pressure gradient at the liquid interface governs the instability of this surface. This instability is analyzed in chapter 5.

3.4 Conclusion

In this study, the dynamic behavior of meniscus angles and contact lines for different fluid properties, different initial bridge geometries, and accelerations were analyzed. The conducted measurements demonstrate the

relation between stretching acceleration and bridge deformation close to the substrate, at the centerline, and the overall curvature. At the meniscus area, the contact line behavior was further studied, and the distinction between the three-phase contact line, a residual layer, and an apparent contact line is presented. The significance of the apparent meniscus angle and the residual layer is getting more pronounced with smaller initial bridge heights. Even two distinct phenomena, cavitation and finger formation, start to emerge and will be addressed in the following chapters. A proportionality based on the geometry of the liquid bridge during the early stretching process between the curvature and the inverse height was found. Furthermore, a proportionality for the mid-point diameter evolution was developed. With the help of the newly found proportionality, the pressure at the center of the bridge and the surface is estimated, used in chapter 4 and chapter 5.

4 Cavitation Phenomena During Liquid Bridge Stretching

Until now, only a change in meniscus behavior is observed during bridge expansion. However, if the tensile stress at the substrate surfaces increases during the bridge elongation, two different phenomena may occur. Firstly, cavitation starts to emerge at the inner of the bridge, and secondly, fingers form at the radially retracting bridge surface. In this chapter, the phenomenon of cavity formation and its evolution is shown and discussed.

4.1 Phenomenological Description

Different forms of cavitation events are shown in the following from a lateral view in figure 4.3 and from top view in figures 4.1, 4.2 and 4.4. Experiments are performed on glass substrates with contact angles of $\theta \approx 40^\circ$. In the following, the term *transient cavitation* refers to the emergence of bubbles and their collapse with emphasis on the short lifespan. In contrast, *cavitation* refers to bubble emergence with a much longer lifespan, where the bubble collapse is suppressed due to the fast bridge stretching.

In figure 4.1 an observation of a transient cavitation series with a *Gly60* mixture and a geometrical boundary condition $\lambda = 4 \times 10^{-5}$ is shown from a top view. At $t = 0$ ms, the liquid is evenly distributed and has a nearly circular shape. After $t = 0.8$ ms the liquid bridge remains pinned and instabilities start to appear, as explained in §3.2.3. In the lower part of the circular shape, two bubbles emerge. At $t = 1.3$ ms, the finger formation starts to show a clear structure, and the bubbles grow further. The bubble close to the center point of the circular shape is growing at a faster rate. The following image $t = 1.6$ ms shows only one bubble. The smaller one has already disappeared. As the finger length increases, the inner region is decreasing. After $t = 1.9$ ms, both bubbles disappeared, and up to $t = 4.8$ ms finger formation proceeds until the inner region of

4 Cavitation Phenomena During Liquid Bridge Stretching

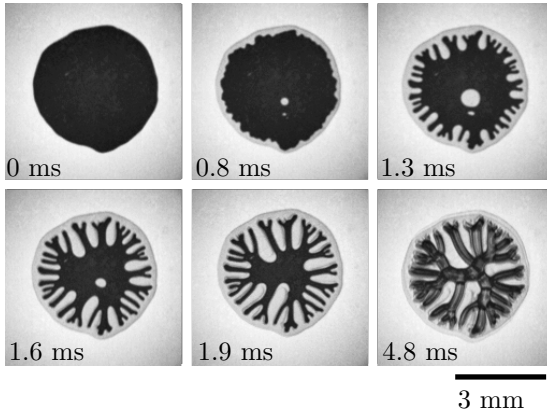


Figure 4.1: Top view on emerging and disappearing cavitation due to bridge stretching. Experiments were performed with *Gly60*, $\lambda = 4.77 \times 10^{-3}$ on glass substrates and a constant stretching rate of 150 m/s^2 .

the liquid bridge is fully bifurcated. In the last image, it is visible that the liquid disintegrates from the formed branches into the surrounding liquid, and the contours start to vanish.

The image sequence in figure 4.2 shows a measurement series of cavitation events with an increased viscosity (*Gly80*) compared to the cases shown in figure 4.1, and geometrical boundary condition $\lambda = 4 \times 10^{-5}$. At $t = 0.5 \text{ ms}$ two bubbles start to emerge and grow strongly at a similar rate, see $t = 1.6 \text{ ms}$. Also, the finger formation starts to get visible at the interface of the liquid bridge. At $t = 2.4 \text{ ms}$ the interface front and the bubbles size increase up to a point where the inner liquid region has disappeared. The cavities are separated only by a small liquid bridge from the contracting interface front. During the growth process they also develop finger formations. At $t = 3.2 \text{ ms}$ the finger and bubble growth has stopped and the liquid bridges appear to be interrupted. The small liquid fingers start to disintegrate already between $t = 3.2 \text{ ms}$ and $t = 4 \text{ ms}$ recognisable by the blurred structures.

The collapse suppression is assumed to be caused due to the axial stretching motion combined with the intruding finger formations at the radial retracting surface. Consequently, a pressure compensation can take

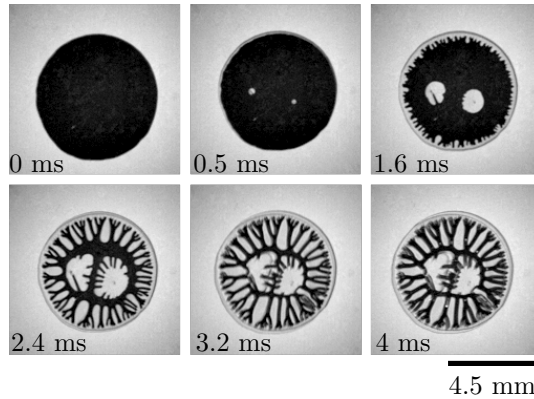


Figure 4.2: Top view on the cavitation events due to bridge stretching. Experiments were performed with *Gly80*, $\lambda = 4 \times 10^{-5}$ on glass substrates and a constant stretching rate of 150 m/s^2 .

place before the bubbles can collapse. In figure 4.3 a side view of this type of cavitation is shown, for a *Gly80* liquid and acceleration of 180 m/s^2 . It is apparent that air is radially invading the liquid bridge and is back cutting the cylindrical-shaped liquid bridge leading to multiple separated bridges and a rippled surface of each filament. The back cutting is assumed to allow for pressure compensation between the surrounding air and the pressure inside the bubble to suppress the bubble collapse. In comparison, the collapse during the transient cavitation has enough time to collapse fully. It hence seems to be a transition phenomenon occurring with experimental parameters between measurements without cavitation events and the described suppressed cavitation.

If λ is decreased and the substrate acceleration increases compared to the previous measurement series, cavitation is even more pronounced. The image sequence in figure 4.4 shows a large initial number of nucleation spots. The measurement series is performed with a *Gly80* solution and geometrical boundary condition $\lambda = 1.3 \times 10^{-4}$. At $t = 0.8 \text{ ms}$, first, bubbles start to form and continuously grow as apparent from $t = 1.6 \text{ ms}$. The disturbed outer surface shows more instabilities than the previous series and a larger number of finger formations. At $t = 2.4 \text{ ms}$, it is apparent that the nucleation onset is unevenly distributed across the profile. The non-symmetrical bubble formation is assumed to be caused by small

4 Cavitation Phenomena During Liquid Bridge Stretching



Figure 4.3: Side view of measurement with pronounced cavitation. Back cutting of finger formation leads to separation of liquid bridges. Measurement was performed with *Gly80*, $\lambda = 4 \times 10^{-5}$ and $a = 180 \text{ m/s}^2$.

deviations from a parallel alignment of the substrates. The small bridge height and the large contact area lead to larger forces during the stretching process. As described in the experimental methods chapter 2, the used method to ensure alignment is reaching its limits for this set of parameters. The emerging fingers show thinner branches compared to the ones shown in figures 4.1 and 4.2. At $t = 3.2 \text{ ms}$, the finger and bubble structure produced show a very chaotic profile of small branches. Due to a large number of bubbles emerged, many small connecting strips separating each bubble are formed. The fingers formed at the external interface were stopped largely at the outer part of the profile and only reached rather small lengths.

It is apparent that the parameters affecting the cavitation formations are: initial dimensionless height λ , liquid viscosity η , and substrate acceleration a . Note however that cavitation can also occur in very thin gaps for substrate accelerations as low as 10 m/s^2 , see figure 5.10. The effect of the acceleration on the cavitation seems to be weaker compared to the effect of viscosity and dimensionless heights on the occurrence of cavitation events. For lower liquid viscosity and larger bridges, as shown in figure 4.1, no cavitation events are present even for relatively high plate accelerations.

With decreasing bridge heights, increasing liquid viscosity, and substrate acceleration, the liquid bridges tend to show an increased number of cavitation events. In the following section, those parameters are used to

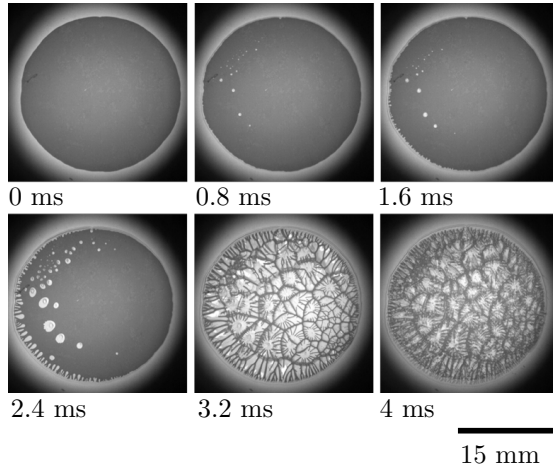


Figure 4.4: Top view on the cavitation due to the bridge stretching. Experimental measurements were performed with *Gly80*, $\lambda = 1.3 \times 10^{-4}$ on glass substrates and a constant stretching rate of 180 m/s^2 .

discuss the implications of the occurrence of cavitation phenomena during transient cavitation.

4.2 Discussion of the Cavitation Dynamics

In the following section, the cavitation dynamics of the transient cavitation events are investigated in greater detail. Firstly, in §4.2.1, the inception of the cavitation is discussed based on the already introduced pressure estimates from §3.3.1. In the second part, the bubble growth is analyzed closer, see §4.2.2. Finally, an analytical solution is presented, based on the experimentally determined radial growth rate, see §4.2.3.

4.2.1 Effect of the Pressure in the Gap on Cavitation

To derive an estimate of the pressure close to the substrate, first, the velocity components in the bridge are determined and used for solving a

4 Cavitation Phenomena During Liquid Bridge Stretching

simplified Navier-Stokes equation. Input parameters are the initial bridge height H_0 , dynamic viscosity η , acceleration a , the time-dependent measured effective bridge radius R_{eff} and the time t . The effective bridge radius corresponds to the inner radius of the wetted area, excluding the finger formation area. Therefore, this area depends on the length of the fingers. According to the previously explained approach the pressure inside the liquid bridge is analytically derived in §3.3.1, leading to equations (3.11) and (3.12). While the derived pressure p includes only the viscous forces, p_σ also takes the surface effects into account. Both pressures estimate p and p_σ have to be compared to identify the more significant source of the pressure change. The derived pressure is only valid in the initial phase of the bridge stretching until the first bubbles start to emerge. The influence of the bubbles on the pressure distribution is not considered in the presented solution. An analysis of the performed measurements shows that the pressure due to viscous forces, represented as p , is of the order of -10^6 Pa and three orders of magnitude greater than the pressure term added to p_σ , due to the surface forces, which is of the order of -10^3 Pa. Even though the surface forces are relatively large due to the initially low bridge height. The viscous forces dominate the emerging pressure, and therefore, it is sufficient to use equation (3.11) in the following section.

The temporal pressure evolution depends on the cavitation type. This is shown in figure 4.5 in which measurements with the same liquid *Gly80*, same acceleration 180 m/s^2 , but different dimensionless heights λ are displayed. Depending on the dimensionless height λ , three different phenomena may occur during the bridge stretching: no cavitation, transient cavitation, and cavitation. It should be emphasized that the stretching motion-induced is pulling the liquid bridge and the fixed substrate into the direction of the forced movement. Therefore, the pressure at both the fixed substrate and at the moving substrate is negative. This is in good agreement with other liquid tensile investigations, showing negative pressure in similar stretching investigation [56, 139]. For measurements with transient cavitation, the absolute pressure extremum is reached after about $t_{p^*} = 0.22 \text{ ms}$. The evolution of the curve is initially dominated by the high substrate speed H' , which leads to a maximum of the absolute pressure shortly after the stretching starts. Due to the high dynamics of the investigated system, bubble growth is delayed, depending on the experimental parameters. This behavior is known from literature [46] and is deducible to reasons as highly non-stationary flow fields and viscous effects. Furthermore, a delay in first observed cavitation events due to

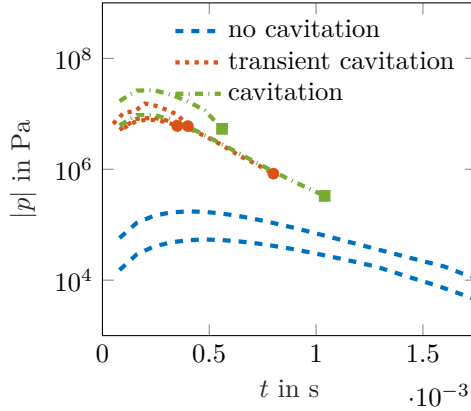


Figure 4.5: Predicted pressure evolution close to the substrate for the fluid *Gly80* with acceleration of 180 m/s^2 and different dimensionless heights of $\lambda = 0.025$ for no cavitation, $\lambda = 0.0012$ for transient cavitation and $\lambda = 0.0010$ with cavitation. The experimentally determined inception point is displayed in the form of a marker.

a limited temporal resolution of $80 \mu\text{s}$ and spatial resolution of $4 \mu\text{m}/\text{px}$ has to be considered.

The arrangement of the curve arrays in figure 4.5 demonstrates that measurements with cavitation events have the highest absolute pressures in the order of 10^7 Pa . They are followed by the measures with transient cavitation in the same pressure range with only slightly lower pressures. Below are only the absolute pressures of the measurements without cavitation, which also show a flatter course and have their extremum in the order of 10^5 Pa .

The curve arrays without cavitation were measured at the larger initial bridge heights H_0 and the smaller initial bridge diameters D_0 corresponding to $\lambda = 0.025$. Measurements in which transient cavitation was observed were performed at $\lambda = 0.0012$ and measurements with cavitation at $\lambda = 0.001$. It can be deduced that the dimensionless bridge height λ has a strong influence on the phenomenological behavior at the substrate surface. Only small changes in the dimensionless height $\Delta\lambda = 0.0002$ can lead to a change between transient cavitation and cavitation with longer

4 Cavitation Phenomena During Liquid Bridge Stretching

remaining bubbles, which cannot collapse under the influence of the bridge stretching motion.

In accordance with the previously mentioned validity range of equation (3.11), the curves for cavitation and transient cavitation are only plotted until the first bubbles are observable. The point at which cavitation bubbles become visible for the first time is highlighted with a marker at the end of each curve.

To better understand the influence of viscosity on the transition point, figure 4.6 shows experiments with a less viscous liquid *Gly50*. The parameters acceleration a and the dimensionless bridge height λ are varied. While the measurements without cavitation and transient cavitation were performed with $\lambda = 0.004$, and measurements with cavitation were performed with $\lambda = 0.001$. For each phenomenon, measurements with three accelerations $a = 90, 150$ and 180 m/s^2 are shown. This means, for example, that of the three blue curves, one with $a = 90$, one with $a = 150$ and one with $a = 180 \text{ m/s}^2$ are displayed. Since the curves are almost on top of each other, the corresponding accelerations are not marked. It can be concluded that the acceleration in the investigated area shows only a minor effect on the occurrence of cavitation bubbles, in contrast to the change of the dimensionless bridge height λ . Only for the experiments with cavitation, a vertical offset is visible for different accelerations, with the most extremum pressure being applied for acceleration $a = 180 \text{ m/s}^2$, and lowest for $a = 90 \text{ m/s}^2$. Following the previously presented measurements, it is apparent that even with varying accelerations and dimensionless heights, the estimated pressure is a useful parameter for classifying the phenomena that occur. In descending order, the measurements with maximum absolute pressures show remaining cavitation patterns. The intermediate pressures arrays show transient cavitation phenomena, and the lower maximum pressures show no cavitation. However, it should be noted that the pressures at which transient cavitation is observable starts for *Gly50* two orders of magnitude below the pressure value compared to the higher viscous liquid *Gly80*. Therefore the perceived pressure threshold is depending on the liquid viscosity.

4.2.2 Bubble Growth

In the following, the properties of bubble growth during transient cavitation will be examined more closely. For this purpose, individual bubble

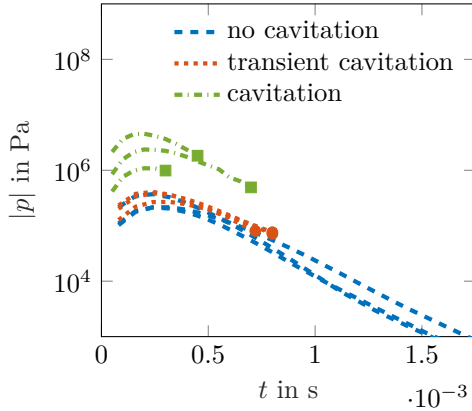


Figure 4.6: Predicted pressure evolution close to the substrate for the fluid *Gly50* with varying accelerations between $90 - 180 \text{ m/s}^2$ and different dimensionless heights $\lambda = 0.004$ for no cavitation, $\lambda = 0.004$ for transient cavitation and $\lambda = 0.001$ with cavitation. The experimentally determined inception point is displayed in the form of a marker.

diameters over time are shown in figure 4.7 with all starting points set to $t = 0 \text{ ms}$. The real-time off-sets for those measurements are shown in figure 4.8. The diameters only provide information about individual bubbles and are not equivalent to the total bubble area, as, in some measurements, multiple bubbles occur during the stretching process. In earlier mentioned events, only the largest bubble is considered. In the presented measurements, the parameters viscosity, *Gly50* and *Gly60* and substrate acceleration, $a = 120, 150, 180 \text{ m/s}^2$ are varied. The dimensionless height $\lambda = 0.004$ is the same for all measurements.

It is noticeable that the same viscosity measurements at higher acceleration show smaller bubble diameters for both *Gly50* and *Gly60*. This seems reasonable due to the higher number of bubble emergence with higher acceleration and individual bubble interaction, as already observed in chapter 4.1. Therefore, the maximum bubble diameters are observable at experiments where fewer bubbles occur and are in the order of several millimeters.

It should also be noted that the growth rate is linear $\dot{D} = 2 \text{ m/s}$ in the

4 Cavitation Phenomena During Liquid Bridge Stretching

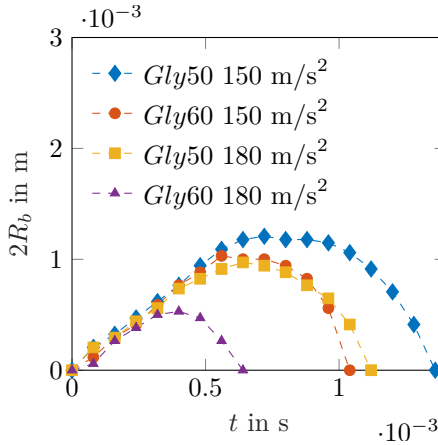


Figure 4.7: Evolution of the largest bubble diameter with transient cavitation events are shown. The shown measurements were performed with different liquids *Gly50* and *Gly60*, different accelerations, 150 and 180 m/s^2 and with the same dimensionless height of $\lambda = 4.5 \times 10^{-4}$. The starting point of each bubble growth event is set to $t = 0$ ms.

beginning for all measurements, see figure 4.7. In contrast, during the retraction phase, the decrease rate no longer follows a similar behavior and increases with time. The linear behavior is uncommon for bubble growth occurring in cavitation events, which follow growth rates typically with an exponent of $1/2$ [46] for spherical bubble cavitation. The divergence is assumed to be caused due to the effects of the forced stretching motion inducing a rapidly changing pressure and flow field leading to a different growth rate. When investigating the retraction phase periods, it is apparent that the time required from the maximum diameter until the bubble collapses is shorter compared to the growth phase and does not show a linear contraction behavior.

Next, the relation between the pressure evolution and bubble growth is investigated. The extremum of the numerical pressure function is reached after $t_{p*} = 0.22 \times 10^{-3}$ s with a standard deviation of 1.8×10^{-5} s for all performed transient cavitation measurements. Therefore, the theoretical maximum pressure is relatively narrowly distributed. Whereas the distribution of the inception times scatter more and are best represented in the

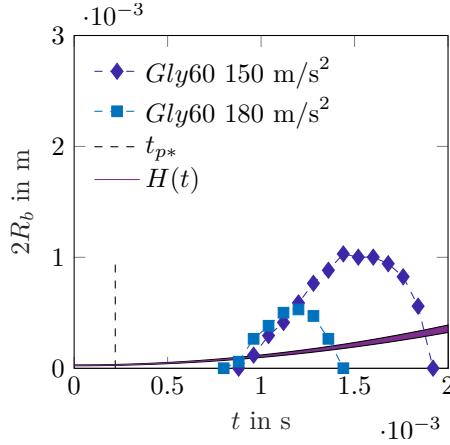


Figure 4.8: Evolution of the largest bubble diameter with transient cavitation events are shown. The shown measurements were performed with the liquids *Gly50* and *Gly60*, accelerations 150 and 180 m/s² and with the same dimensionless height of $\lambda = 4.5 \times 10^{-4}$. Additionally, the bridge height over time is included as area plot for the substrate accelerations 150 – 180 m/s² and the mean extremum pressure time t_{p^*} is shown.

form of a logarithmic normal distribution with a mean of 1.29×10^{-3} s and standard deviation of 9.15×10^{-4} s, see figure 4.9. The need for a logarithmic normal distribution is apparent since the distribution is skewed partly because of exclusively positive values [140, 141]. Reasons for the large scatter in the inception times are the number of parameters affecting the bubble onset leading to inhomogeneities in the liquid and at the surface serving as nuclei. Due to the fluid dynamic conditions, existing bubbles start to grow from inside nuclei and are only visible after reaching a specific size.

When comparing the times between the occurrence of the extremum of the pressure functions t_{p^*} and the maximum bubble diameter, the previously discussed bubble inception times are inevitably included in the measurements. By comparing t_{p^*} from figure 4.5 and 4.6 with the bubble diameter evolution of figure 4.8, it can be observed that the time difference between the maximum pressure and the bubble inception point is of

4 Cavitation Phenomena During Liquid Bridge Stretching

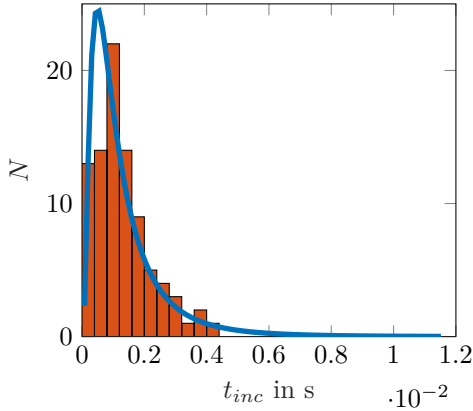


Figure 4.9: Histogram of the bubble inception times of the transient cavitation events. Additionally a logarithmic distribution fit is added with a mean of $\mu = 1.29 \times 10^{-3}$ and standard deviation $s = 9.15 \times 10^{-4}$.

the order of nearly one millisecond. The waiting time between the occurrence of maximum pressure and the formation of bubbles is known from other studies [46], in which equation (1.1) is numerically integrated and then used to calculate the bubble growth depending on the pressure function. Due to the unknown size of the initial bubble radius and the derived pressure equation being only valid until cavitation occurs, an analytical solution commonly based on equation (1.1) is not possible with the introduced equations. But when adjusting the introduced viscous pressure to take the bubble growth into account, a bubble growth estimate is possible, as shown in the following section.

4.2.3 Dynamics of the Cylindrical Bubble Expansion

In this section, the dynamics of a cavitation bubble is modeled. Only cases with a single cavitation bubble are considered in this study. Nevertheless, the conclusions of this study can be potentially applicable also to cases with multiple bubbles.

During the stretching process of the liquid bridge, when cavitation phenomena arise, two opposing movements are present. Due to the expansion

of the bridge, the outer diameter reduces, while on the inside, a radially increasing cavitation bubble emerges. As discussed in the previous section, the rate change of the bubble diameters shows a linear behavior during its growing phase for different parameters. In contrast, during the reducing phase, no precise rate of the decrease can be determined. That and the observation explained earlier that the diameter is much larger compared to the height of the bubble, which led to the assumption that the geometry of the cavitation bubble is cylindrical. A cylindrical bubble geometry could explain the suppressed bubble collapse of the cavitation events of back cutting, due to a cylindrical bubble giving a broader point of attack for a pressure compensation than a half cap sitting close to the surface.

Figure 4.8 shows the bridge height $H(t)$ compared to the diameter of transient cavitation bubbles during their growth and collapse phase. The curve represents accelerations from $150 - 180 \text{ m/s}^2$ and therefore diverges over time. The diameter of the bubble is significantly larger than the distance between the fixed and moving substrate. Therefore, the bubble can not have a spherical or half-cap shape since expansion in the axial direction of the bridge is restricted by the bridge height. Even though it is not possible to get an experimental image of the side bubble profile in the first microseconds with the current setup, the shown bubble diameter and bridge height gives an estimate of the bubble geometry. It is assumed that the side profile is a cylindrical shaped bubble, which is stretched during the bridge deformation.

In order to be able to validate the explained hypothesis a new pressure estimate is required. Therefore, the radial velocity of the outer liquid bridge is derived with help of the continuity equation in the following form:

$$\frac{\partial H}{\partial t} \pi(r^2 - R_b^2) + 2\pi r H u_r - 2\pi R_b H \frac{\partial R_b}{\partial t} = 0. \quad (4.1)$$

The elongation of the liquid bridge represented by the first term of equation (4.1) combined with the radial outward expansion of the cavitation bubble in the second term and the radial inward movement at the external surface in the third term. Here R_b is the bubble radius, u_r is the radial retracting velocity at the surface of the bridge, as shown in figure 4.10. The expression for the average radial velocity in the liquid is obtained in the form

4 Cavitation Phenomena During Liquid Bridge Stretching

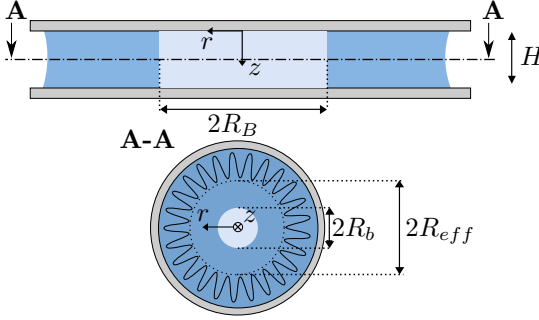


Figure 4.10: Sketch of cylindrical bubble formation during an cavitation event.

$$u_r = \frac{-r^2 \frac{\partial H}{\partial t} + R_b^2 \frac{\partial H}{\partial t} + 2HR_b \frac{\partial R_b}{\partial t}}{2rH}. \quad (4.2)$$

The expressions for H and $\frac{\partial H}{\partial t}$ are given in equation (3.10). With the help of the pressure gradient from the simplified Navier-Stokes equation, introduced in equation (3.9) for viscous stretching, and the new radial velocity u_r of equation (4.2), the expression for the pressure p_b at the surface of the cavitating bubble can be derived in the form:

$$p_b = \int_{R_b}^{R_{\text{eff}}} 12 \frac{u_r \mu}{H^2} dr. \quad (4.3)$$

Thereby R_{eff} is the effective radius without any formed fingers, determined in figure 3.21.

Neglecting the pressure at the surface due to the much larger viscous pressure, it can be assumed that at the surface $p_b|_{r=R_{\text{eff}}}$. The other pressure terms are neglected due to the large magnitude of the viscous pressure term, as explained later in greater detail in chapter 4.2. By solving equation (4.3) the bubbles diameter growth rate can be derived as:

$$\frac{\partial R_b}{\partial t} = \frac{-2R_b^2 \frac{\partial H}{\partial t} \ln\left(\frac{R_{\text{eff}}}{R_b}\right) - R_b^2 \frac{\partial H}{\partial t} + R_{\text{eff}}^2 \frac{\partial H}{\partial t}}{4HR_b \ln\left(\frac{R_{\text{eff}}}{R_b}\right)}. \quad (4.4)$$

4.2 Discussion of the Cavitation Dynamics

In order to get an scalable solution, the dimensionless time for the bubble growth is introduced as τ_b and for the dimensionless bubble amplitude as Λ :

$$\tau_b = t \sqrt{\frac{a}{2H_0}}, \quad \Lambda = \frac{R_b}{R_0} \sqrt{\frac{2H_0}{at^2}}. \quad (4.5)$$

To find and validate the linear growth behaviour of the cavitation bubbles, the amplitude ratio Λ has to be derived next. This can be achieved by differentiating equation (4.5) and applying the already known $\frac{\partial R_b}{\partial t}$ from equation (4.4) as demonstrated hereinafter:

$$\frac{\partial \Lambda}{\partial \tau_b} = - \frac{\tau_b \left[(\tau_b^2 + 1) \Lambda^2 \left(2 \ln \left[\frac{1}{\sqrt{\tau_b^2 + 1} \Lambda} \right] + 1 \right) - 1 \right]}{2 (\tau_b^2 + 1)^2 \Lambda \ln \left[\frac{1}{\sqrt{\tau_b^2 + 1} \Lambda} \right]} \quad (4.6)$$

When solving the differential equation and using only the positive positive solution, Λ can be determined as a function of τ_b . With the initial condition $\tau_b = \tau_{b,\text{inc}}$ known from the experimentally determined time of inception, the estimate for the dimensionless Λ is:

$$\Lambda = \frac{\sqrt{\ln\left(\frac{\tau_b^2 + 1}{1 + \tau_{b,\text{inc}}^2}\right)}}{\sqrt{\tau_b^2 + 1}}. \quad (4.7)$$

The extremum of the dimensionless amplitude ratio Λ is now easily obtainable and gives the point in time of the maximum bubble diameter, also known from the conducted experiments as $t_{b,\text{max}}$. Therefore a validation of the experimentally determined inception and maximum times is available in the form:

$$\tau_{b,\text{max}} = \sqrt{-1 + e^{1 + \tau_{b,\text{inc}}^2}}. \quad (4.8)$$

In figure 4.11 the maximum time $\tau_{b,\text{max}}$ is shown as function of $\tau_{b,\text{inc}}$ together with the ideal relation for cylindrical bubble growth behaviour from $1 + \tau_{b,\text{max}}^2 = e^{1 + \tau_{b,\text{inc}}^2}$. The measured relation between the inception time and the time of the maximum bubble area coincide with the derived

4 Cavitation Phenomena During Liquid Bridge Stretching

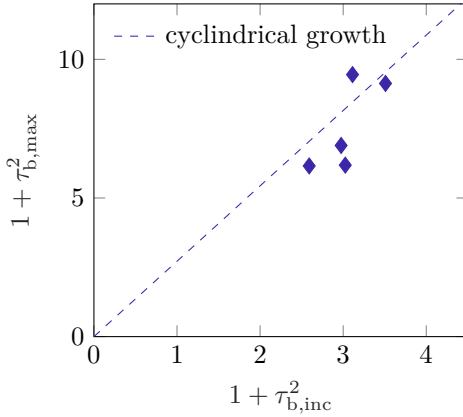


Figure 4.11: Bubble growth of transient cavitation measurements. The dashed line show the ideal growth rate of a cylindrical bubble. Here $\tau_{b,max}$ is the experimentally determined dimensionless time instant of the maximum bubble diameter. $\tau_{b,inc}$ represents the measured dimensionless inception times of the beginning of the bubble growth phase.

analytical solution for the same problem. It validates the earlier introduced hypothesis that the stretching of the liquid bridge and the initial geometry constraint lead do a cylindrical bubble geometry.

4.3 Conclusion

Under certain conditions, the expansion of the liquid bridge can lead to different cavitation forms. The various phenomena are presented, and the most influencing parameters are derived and discussed in this chapter.

Two different forms of cavitation are examined, and, by estimating the pressure close to the substrate, a magnitude for the threshold estimate is presented. The order of appearance of each phenomenon can be explained with the help of the estimated pressure. The transient cavitation phenomenon was already observed in a few other studies, but not seen as a transition phenomenon between the suppressed cavitation events and the experiments without cavitation. The transient cavitation phenomenon is

notably sensitive to parameter changes, especially the liquid bridge height λ and is only observable in a small corridor of parameters. Furthermore, the bubble profile during the cavitation is studied, and linear growth and non-linear contraction are observed. The linear growth rate indicates that the pressure and flow field differs from the known solutions from the domain of cavitation studies.

Additionally, the form of the bubble is thereby assumed to be affected. Hence, the bubble shape can be elongated in the axial direction due to the stretching motion in cylindrical geometry. The deviating bubble behavior is assumed to be based on a combination of the dynamic pressure distributions of the cavitation event and the stretching movement. This hypothesis is validated with a new pressure estimate being valid during the cavitation growth phase. It is shown that with the cavitation inception moment and the instant of the maximum bubble diameter, a cylindrical bubble geometry can be derived.

5 Fingering Instability of the Stretching Bridge

In this section, the formation of the bridge instability, leading to the appearance of the fingers on its surface, is investigated. The surface instabilities leading to finger formation often occur concurrently with cavitation phenomena and emerge only with larger elongation rates, higher viscosities, and small bridge height to diameter ratios. In this section, the onset and the number of finger emerging are discussed, and a theory is derived to estimate both parameters. Parts of this chapter have been published in [21, 142].

5.1 Phenomenological Description

As the available experimental set-up allows top and side view measurements of the stretching process, an example of a side view, high-speed visualization of a stretching *Gly80* bridge is shown in figure 5.1. The difference to the measurements introduced in figure 3.1 and 3.2 is the uneven interface shape visible at 3.7 ms and at 5ms, indicating a finger formation. In this example, the substrate acceleration is 180 m/s^2 and the initial height is $20 \mu\text{m}$. The initial liquid bridge height-to-diameter ratio is $\lambda = 0.02$. A more distinct pattern occurs for even smaller bridge heights, then the bridge separates in single bridges, as shown in the previous chapter in figure 4.3. Which was conducted with an dimensionless height of $\lambda = 4 \times 10^{-5}$ with *Gly80* and an acceleration of 180 m/s^2 .

A more distinct view of the finger formation is available in figure 5.2 from the top view set-up. The diameter relevant for the formation of the finger instability is D_M , as introduced in figure 3.21. Several typical top views of the liquid bridge through the transparent substrate are shown at different instants for various experimental parameters. In some cases, the onset of instability can be seen, leading to finger patterns.

5 Fingering Instability of the Stretching Bridge

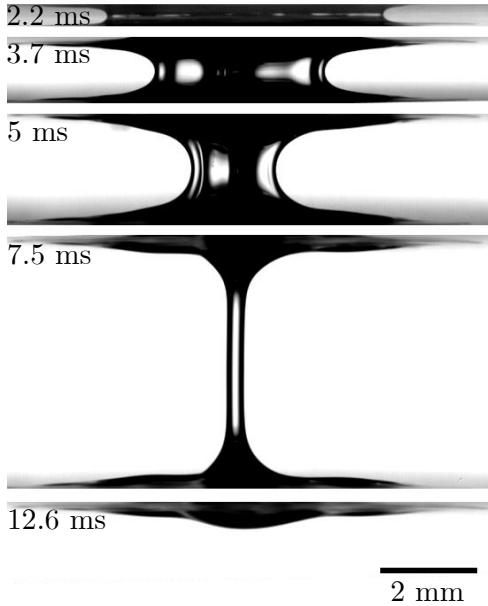


Figure 5.1: Evolution of the diameter of a liquid bridge. Side views of a Gly80 bridge stretched with constant acceleration of 180 m/s^2 . The initial gap is $20 \mu\text{m}$ and the gap-to-diameter ratio is $\lambda = 0.02$. Reprinted from [21] under CC BY 4.0.

The most stable case in figure 5.2 a) is obtained with a relatively wide gap and low acceleration. It is apparent that during the stretching, only the diameter D_M starts to recede beginning at 2.2 ms and is keeping its nearly its cylindrical shape up to 6.6 ms. The most unstable case, associated with the highest number of fingers, corresponds to the highest accelerations and smaller initial gap widths, as shown in the example in figure 5.2 b). After 0.7 ms, distinguished cup forms are recognizable, and after 1.4 ms, the final finger pattern is visible. The finger pattern shows branches that unite towards the midpoint of the cylinder, and at the inner part, an undisturbed area is apparent. After 5.8 ms, the finger pattern is getting blurry, and the deposited liquid is starting to recede into its optimized surface shape. In the example in figure 5.2 c), fingers

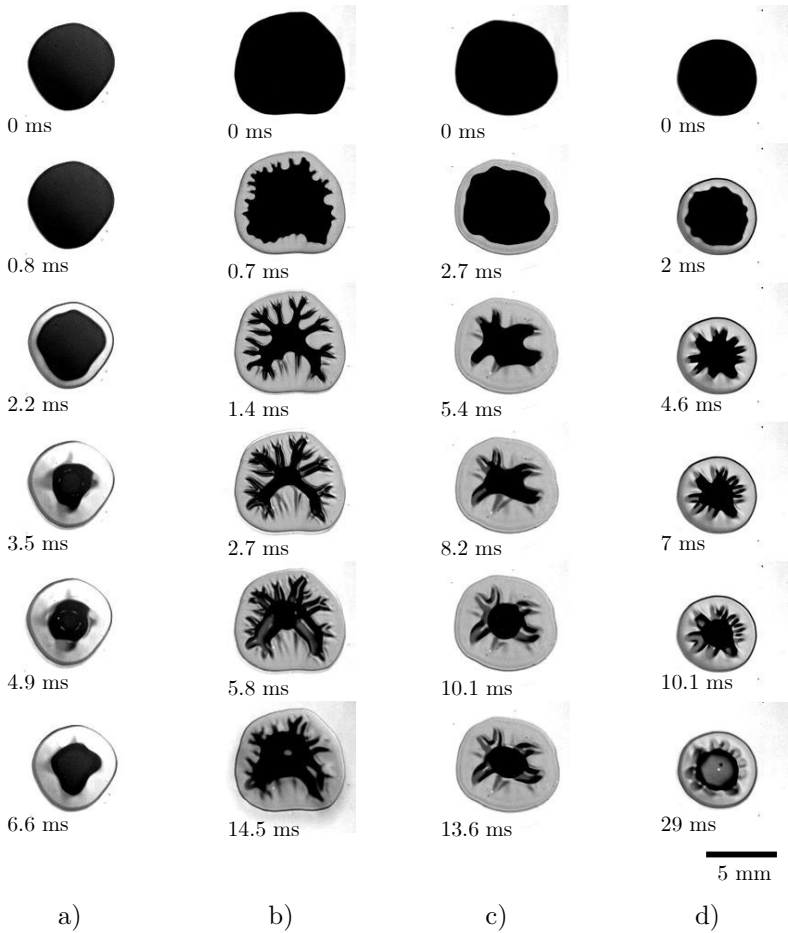


Figure 5.2: Top view of the receding interface due to bridge stretching under various experimental conditions: a) liquid *Gly50*, substrate acceleration $a = 180 \text{ m/s}^2$, relative gap width $\lambda = 0.03$; b) *Gly50*, $a = 180 \text{ m/s}^2$, $\lambda = 0.006$; c) *Gly50*, $a = 10 \text{ m/s}^2$, $\lambda = 0.06$; d) *Gly80*, $a = 10 \text{ m/s}^2$, $\lambda = 0.03$. Contact angles are $\theta \approx 40^\circ$ for *Gly50* and *Gly80* on the glass substrate. Reprinted from [21] under CC BY 4.0.

5 Fingering Instability of the Stretching Bridge

can be observed even with relatively small substrate acceleration, but only for small dimensionless heights λ . The slower stretching rate with the same non-dimensional height, as shown in 5.2 c), leads to a coarser finger pattern with fewer fingers formed. The branches apparent at 5.4 ms do not show side branches up to the final pattern. In figure 5.2 d), the effect of increased liquid viscosity is shown, which leads to a clear finger pattern again. The cusps start to be visible at 2 ms and form more evenly distributed at the receding surface as in 5.2b). The homogeneous deformation can be attributed to the higher viscosity.

Overall it can be concluded that increasing the substrate acceleration or viscosity enhances the finger instability, whereas, with an increasing dimensionless height λ , finger formation is mitigated.

The central part of this study was conducted using quartz glass substrates with a static contact angle of $\theta \approx 40^\circ$. For the measurements shown in this chapter, the outer contour of the bridge also remains pinned during finger formation, due to the time scale of the emerging fingers is relatively short compared to the dewetting time scale, as shown before. To investigate the effect of wettability on the finger instability, a few measurements with different contact angles were also performed and added to the study. Therefore, the silanized substrates with contact angles as high as $\theta \approx 110^\circ$ are used in addition.

Another already introduced phenomenon affecting the finger formation quite significantly is the cavitation during liquid bridge stretching. The constriction of the inner bridge diameter and the pressure dynamics close to the cavitation bubbles substantially change the pressure distribution. The pressure estimate used for the linear stability analysis in this chapter does not consider the pressure fluctuations caused by the cavitation events. This approach was chosen to reduce the complexity of the finger formation problem as a first approach. The effect of the bubble emergence on the finger formation, especially the derived prediction, is analyzed further in the discussion section of this chapter.

5.2 Stability Analysis of the Bridge Interface

In this section, a stability analysis is performed based on experimental measurements of the flow in a thin gap between two substrates. The problem is linearised in the framework of the long-wave approximation.

It is assumed that the main reason for the surface instability at the bridge surface is the appearance of a normal pressure gradient at the interface. This mechanism is analogous to the Rayleigh-Taylor instability, where the pressure gradient is caused by gravity or by the interface acceleration, as already mentioned in chapter 1.

5.2.1 Long-Wave Approximation of Small Flow Perturbations on a Planar Interface

Since the diameter of the liquid bridge is much larger than the gap thickness, $D_M \gg H$, the flow leading to small interface disturbances can be considered in a Cartesian coordinate system x, y , where the x coordinate coincides with the radial direction normal to the meniscus, defined as $x = 0$, and the y direction is tangential to the meniscus, as shown in figure 3.21 for t_1 . The kinematic relation (3.4) allows the evaluation of the necessary condition $D_M \gg H$, which is satisfied at times $t \ll \sqrt{2(D_{M,0}/2 - H_0)/a}$. In all our experiments, this condition is satisfied. To reduce the size of the following equations, R is used instead of $D_M/2$, and the partial derivative is given in the form of $u_{,x}$ instead of $\frac{\partial u}{\partial x}$.

The coordinate system x, y is fixed at the meniscus of the liquid bridge, such that

$$r = R + x. \quad (5.1)$$

The small flow perturbations, in the direction normal to the substrates, are neglected. Liquid flow occupies the semi-infinite space $x \in] - \infty; 0]$. Denote $u'(x, y, t)$; $v'(x, y, t)$ as the velocity vector of the flow perturbations, averaged through the gap width, and $p'(x, y, t)$ is the pressure perturbation. The absolute velocity and the pressure p in the gap can be expressed in the form

$$u = \dot{R}(t) + u'(x, y, t), \quad v = v'(x, y, t), \quad p = p_0(x, t) + p'(x, y, t). \quad (5.2)$$

Therefore, the time derivatives of the components of the velocity field can be written in the form

$$u_{,t} = \ddot{R} + u'_{,t} - \dot{R}u'_{,x}, \quad v_{,t} = v'_{,t} - \dot{R}v'_{,x}. \quad (5.3)$$

The gap thickness H is assumed to be the smallest length scale in the problem. In this case, consideration of only the dominant terms in the

5 Fingering Instability of the Stretching Bridge

Navier-Stokes equation, written in the accelerating coordinate system, yields

$$p_{,x} = \mu \left(-b \frac{\dot{R} + u'}{H^2} + u'_{,xx} + u'_{,yy} \right) - \rho \ddot{R} - \rho u'_{,t}, \quad (5.4a)$$

$$p_{,y} = \mu \left(-b \frac{v'}{H^2} + v'_{,xx} + v'_{,yy} \right) - \rho v'_{,t}. \quad (5.4b)$$

The characteristic value of the leading viscous terms in the pressure gradient expressions (5.4a) and (5.4b) is $\mu b u' / H_0^2$. The characteristic time of the problem is $\sqrt{H_0/a}$. Therefore, the inertial terms of the flow fluctuations are of order $\rho u'_{,t} \sim \rho u' \sqrt{a/H_0}$. The Reynolds number, defined as the ratio of the inertial and viscous terms, is therefore

$$Re = \frac{a^{1/2} H_0^{3/2} \rho}{b \mu}. \quad (5.5)$$

In all experiments, the Reynolds number is of the order of 10^{-2} . The inertial effects associated with the flow fluctuations are therefore negligibly small. The governing equation for the velocity perturbation can then be obtained from (5.4a) and (5.4b), neglecting the terms $\rho u'_{,t}$ and $\rho v'_{,t}$:

$$-b \frac{u'_{,y} - v'_{,x}}{H^2} + u'_{,xxy} + u'_{,yyy} - v'_{,xxx} - v'_{,yyx} = 0. \quad (5.6)$$

The velocity field u', v' has to satisfy (5.6) as well as the continuity equation and the condition of the shear-free meniscus surface:

$$u'_{,x} + v'_{,y} = 0, \quad (5.7a)$$

$$u'_{,y} + v'_{,x} = 0, \quad \text{at } x = 0. \quad (5.7b)$$

Consider the sinusoidal profile of the flow fluctuations along the y direction. This means that both velocity components include the term e^{ik} , where k is the wavenumber. The corresponding velocity field for the velocity of the small flow disturbances satisfying (5.6)-(5.7b) is

$$u' = \left(e^{kx} - \frac{2H^2 k^2}{b + 2H^2 k^2} e^{\frac{\sqrt{b+H^2 k^2}}{H} x} \right) e^{iky} T(t), \quad (5.8a)$$

$$v' = i \left(e^{kx} - \frac{2Hk\sqrt{b+H^2 k^2}}{b + 2H^2 k^2} e^{\frac{\sqrt{b+H^2 k^2}}{H} x} \right) e^{iky} T(t), \quad (5.8b)$$

5.2 Stability Analysis of the Bridge Interface

where $T(t)$ is a function of time.

The small perturbations of the meniscus shape, defined as $x = \delta(y, t)$, are determined by the normal velocity component u at the meniscus $x = 0$. The boundary conditions for the meniscus perturbations, $\delta_{,t} = u$ at $x = 0$, yield

$$\delta = e^{iky}G(t), \quad \text{with} \quad T(t) = \frac{b + 2H^2k^2}{b}\dot{G}(t). \quad (5.9)$$

The pressure increment, associated with the flow perturbations at the interface, p' , is determined by the capillary forces and viscous stress:

$$p'(x, t) = -\sigma\delta_{,yy} - 2\mu u_{,x}, \quad \text{at} \quad x = \delta(y, t). \quad (5.10)$$

The total pressure near the meniscus also depends on the curvature in the plane normal to the substrate. In this study, the dependence of the shape of the meniscus in this plane on $\delta(y, t)$ is neglected, since the capillary pressure associated with this curvature is approximated by $p \sim \sigma/H$. Thus, this pressure does not depend on the y coordinate and does not contribute to flow stability.

The pressure p' at position $x = 0$ can be approximated accounting for the smallness of the shape deformation:

$$p' = -\sigma\delta_{,yy} - \delta p_{0,r} - 2\mu u_{,x}, \quad \text{at} \quad x = 0, \quad (5.11)$$

where $p_{0,r}$ is the pressure gradient at the meniscus of the basic flow, determined in (3.13). The term $\delta p_{0,r}$ appears as a result of linearisation of the pressure terms in the neighbourhood of the liquid bridge interface.

Substituting (5.11) in expression (5.4b) yields, with the help of (5.8a)-(5.9), the following ordinary differential equation for the function $G(t)$:

$$b(k^3\sigma - kp_{0,r})H^2G(t) + \left[4H^3k^3\left(\sqrt{H^2k^2 + b} - Hk\right) + b^2\right]\mu\dot{G}(t) = 0. \quad (5.12)$$

The solution of the ordinary differential equation (5.12) is

$$G(t) = \delta_0 e^{-\frac{b}{\mu} \int_0^t \frac{H^2(k^3\sigma - kp_{0,r})}{4H^3k^3(\sqrt{H^2k^2 + b} - Hk) + b^2} dt}, \quad (5.13)$$

where δ_0 is the initial meniscus perturbation.

5 Fingering Instability of the Stretching Bridge

The function $G(t)$ in (5.13) can be derived using (3.4) and (3.13). It can be expressed in dimensionless as

$$G = \delta_0 e^{\frac{\sqrt{b}}{2\lambda}} \int_0^\tau \Omega(\xi, \tau) d\tau, \quad (5.14)$$

$$\Omega = \frac{\tau \xi (\tau^2 + 1)^{-3/2} - \frac{\xi^3}{Ca} (\tau^2 + 1)^2 + \frac{Re(1-2\tau^2)\xi}{\sqrt{2}\sqrt{\tau^2+1}}}{1 - 4(\tau^2 + 1)^3 \xi^3 \left[\xi(\tau^2 + 1) - \sqrt{(\tau^2 + 1)^2 \xi^2 + 1} \right]}, \quad (5.15)$$

where the dimensionless time τ , the dimensionless wave number ξ and the capillary number Ca are defined as

$$\tau = t \sqrt{\frac{a}{2H_0}}, \quad \xi = \frac{kH_0}{\sqrt{b}}, \quad Ca = \frac{\sqrt{a}\mu R_0}{\sqrt{2H_0}\sigma}. \quad (5.16)$$

The Reynolds number is defined in (5.5) and the geometrical parameter is $\lambda = H_0/2R_0$, as defined in §5.1.

Equations (5.14) and (5.15) allow computation of the evolution of the amplitude of waves for a given wavelength and given parameters of the liquid bridge stretching.

In figure 5.3 the dimensionless amplitude of the perturbations of the bridge radius $\ln(G/\delta_0)$, computed using (5.14), is shown as a function of the dimensionless wavenumber ξ for various times τ . In the cases shown in figure 5.3a) and b), corresponding to a large number of fingers, the absolute amplitude of the perturbation G is two orders of magnitude higher than the amplitude of the initial perturbations δ_0 . In the case of figure 5.3c) close to the finger formation threshold, $G/\delta_0 \sim 10^1$, while in the case shown in figure 5.3d), in which no apparent finger pattern has been observed, the value of G/δ_0 is of order unity. In each of the cases shown in figure 5.3a) the wave number corresponding to the maximum amplitude is only slightly dependent on time but is significantly influenced by the parameters of the bridge stretching.

5.2.2 Approximation for Small Capillary Numbers

In the long-wave approximation, values of ξ are assumed to be small. This assumption can again be examined after the solution for typical values of ξ has been obtained. In this study, only the dominant terms are taken into account, while the terms of $O(\xi^4)$ are neglected. The corresponding

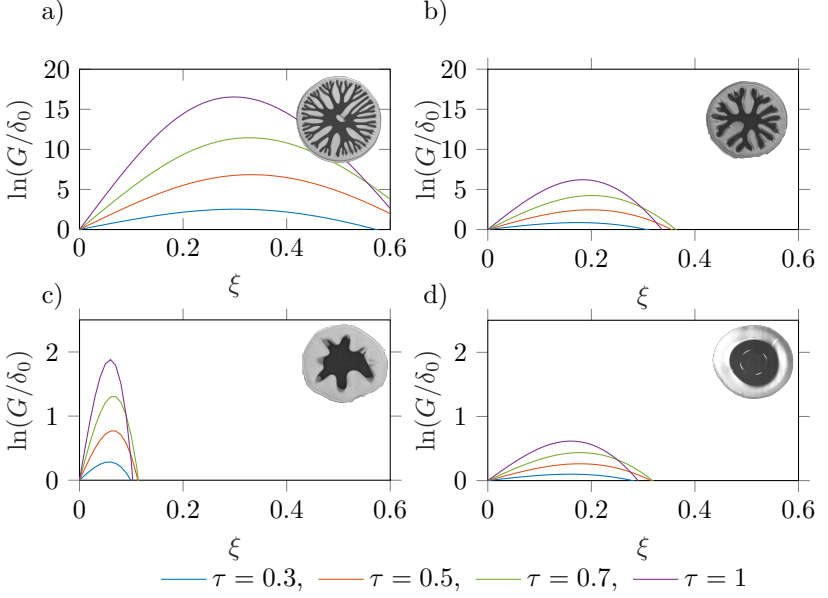


Figure 5.3: Dimensionless amplitude of the radius perturbations $\ln(G/\delta_0)$ as a function of the dimensionless wave numbers ξ for various time instants τ , computed by numerical integration of (5.13). a) $Ca = 2.45, Re = 0.005, \lambda = 0.0059$, b) $Ca = 0.704, Re = 0.0026, \lambda = 0.0099$, c) $Ca = 0.0663, Re = 0.0252, \lambda = 0.0109$ and d) $Ca = 0.5109, Re = 0.034, \lambda = 0.0902$. Reprinted from [21] under CC BY 4.0.

approximate expression for $\int_0^\tau \Omega d\tau$ is derived in the form

$$\int_0^\tau \Omega(\xi, \tau) d\tau = \xi - \frac{\tau(3\tau^4 + 10\tau^2 + 15)\xi^3}{15Ca} - \frac{\xi}{\sqrt{\tau^2 + 1}} - \frac{Re\xi}{\sqrt{2}} \left(\tau\sqrt{\tau^2 + 1} - 2\operatorname{arcsinh}\tau \right) + \mathcal{O}(\xi^4). \quad (5.17)$$

The most unstable mode ξ_* associated with the maximum positive value

5 Fingering Instability of the Stretching Bridge

of the function $\int_0^\tau \Omega d\tau$ is therefore

$$\xi_* = \sqrt{Ca} \left[\frac{1 - \frac{1}{\sqrt{\tau^2+1}} + \frac{Re}{\sqrt{2}} (\tau\sqrt{\tau^2+1} - 2\operatorname{arcsinh}\tau)}{\tau \left(\frac{3}{5}\tau^4 + 2\tau^2 + 3 \right)} \right]^{1/2}. \quad (5.18)$$

The dimensionless time τ is of the order of unity. The value of the dimensionless wave number also has to be small in the framework of the long-wave approximation used in this study. Therefore, the solution (5.18) for the most unstable mode ξ_* is valid only for small capillary numbers.

The wavelength of the most unstable mode is $\ell_* = 2\pi/k$. The number of finger-like jets is therefore

$$N_f = 2\pi R/\ell_* = \frac{\sqrt{b}}{2\lambda} \frac{\xi_*}{\sqrt{1+\tau^2}}. \quad (5.19)$$

The expression for the number of fingers is obtained using (5.18):

$$N_f = \frac{\sqrt{bCa}}{2\lambda} \left[\frac{1 - \frac{1}{\sqrt{\tau^2+1}} + \frac{Re}{\sqrt{2}} (\tau\sqrt{\tau^2+1} - 2\operatorname{arcsinh}\tau)}{\tau(\tau^2+1) \left(\frac{3}{5}\tau^4 + 2\tau^2 + 3 \right)} \right]^{1/2}. \quad (5.20)$$

The predicted number of fingers depends on the dimensionless time τ . Observations confirm such dependence.

5.3 Results and Discussion

The maximum value of the function $N_f(\tau)$ can be computed from (5.20). In the limit $Re = 0$, the maximum,

$$N_{\max} \approx 0.38\sqrt{Ca}/\lambda, \quad Ca \ll 1, \quad Re = 0 \quad (5.21)$$

is reached at the instant $\tau_* \approx 0.49$. The predicted bridge radius R corresponding to the maximum number of jets is therefore $R_* = R_0(1 + \tau_*^2)^{-1/2} \approx 0.9R_0$.

In figure 5.4, the experimentally measured number of fingers at various instants and corresponding radii scaled by R_0 are shown exemplarily for three different values of Ca , but for nearly the same amounts of λ and

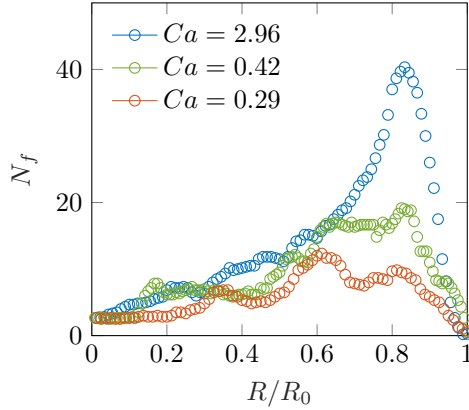


Figure 5.4: The number of fingers N_f as a function of the liquid bridge radius R observed in three different experiments. The measurements were performed with $\lambda \approx 0.01$ and $Re \approx 0.1$. Reprinted from [21] under CC BY 4.0.

Re. The number of fingers reaches the maximum at the radii $R_*/R_0 \approx 0.8 - 0.9$, as predicted by the theory.

For lower radii $R \ll R_*$, corresponding to longer times τ , the flow in the gap is significantly influenced by the nonlinear effects associated with the growth of fingers. Such a nonlinear analysis is out of the scope of this theoretical study. For smaller Ca numbers, the influence of the nonlinear effects becomes larger; for those cases, we have to limit the analysis to a local maximum at $R > R_*$.

The amplitude of the perturbations at the corresponding conditions, $\xi = \xi_*$, $\tau = \tau_*$, can also be estimated for small capillary numbers:

$$G_* \approx \delta_0 e^{0.11Ca^{1/2}\lambda^{-1}}, \quad Ca \ll 1, \quad Re = 0. \quad (5.22)$$

Given the approximate estimation of the number of fingers (5.20), the dimensionless parameter $N_{\max}\lambda/Ca^{1/2}$ is a function of the Reynolds number if the capillary number is small. In figure 5.5 this dependency is compared with theoretical predictions based on the numerical computation of the maximum value of the expression for N_f (5.20). The theoretical predictions do not contradict the experiments. However, the clear dependence of the number of fingers on the value of the Reynolds number is not

5 Fingering Instability of the Stretching Bridge

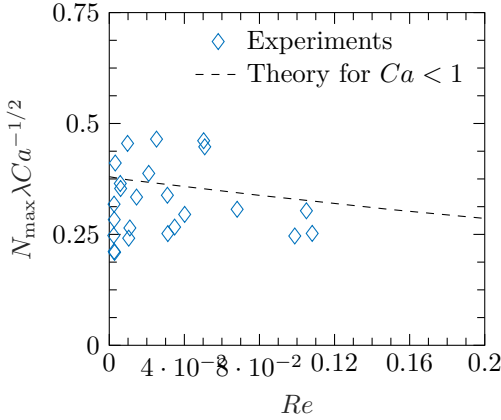


Figure 5.5: Scaled maximum number of the observed fingers $N_{\max} \lambda / Ca^{1/2}$ as a function of the Reynolds number. Reprinted from [21] under CC BY 4.0.

that apparent due to the relatively large scatter of data. This scatter can be explained by the fact that in the cases close to the finger formation threshold, the amplitude of perturbations is relatively small at the time instant corresponding to $N_f = N_{\max}$. Therefore, the fingers can only be recognized by the optical system slightly later, when the amplitude magnification is significant. The conditions near the finger formation threshold (5.24) are discussed later in this section.

The approximate solution (5.18) for the most unstable mode, based on the assumption of the smallness of ξ_* , does not apply to the cases when the capillary number is not very small. In these cases, a complete numerical solution is required. In this solution the values of $\xi_*(\tau)$ for a specific capillary number Ca and Reynolds number are first computed as a point corresponding to the maximum of $\int_0^\tau \Omega d\tau$, where $\Omega(\xi, \tau)$ is defined in (5.15). Then, the maximum number of fingers is computed using (5.19) at the time interval $\tau > 0$. The theoretically predicted values of $N_{\max} \lambda$ are determined only by the capillary number and the Reynolds number. The theoretical predictions of $N_{\max} \lambda$ are shown in figure 5.6. As expected, the influence of inertia becomes significant when both the capillary and Reynolds numbers are relatively large.

The significance of the inertial effects in this problem is rather sur-

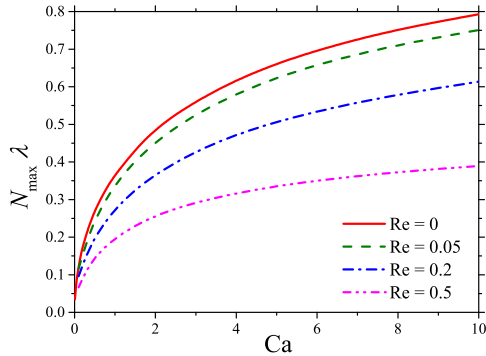


Figure 5.6: Computational results of $N_{\max}\lambda$ as a function of the capillary number Ca for various Reynolds numbers Re . Comparison with theoretical predictions based on the approximate solution. Reprinted from [21] under CC BY 4.0.

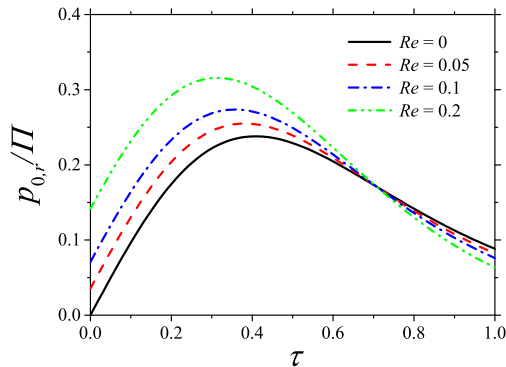


Figure 5.7: The values of the scaled pressure gradient at the meniscus interface $p_{0,r}/\Pi$ as a function of dimensionless time τ for various values of the Reynolds number Re . The scale for the pressure gradient, Π , is defined in (5.23). Reprinted from [21] under CC BY 4.0.

5 Fingering Instability of the Stretching Bridge

prising, noting the very small values of Reynolds numbers considered in this study. The main factor governing the finger formation process is the pressure gradient at the meniscus interface (3.13), obtained from the base solution. The mechanism of instability caused by the positive normal pressure gradient at the liquid interface is analogous to the Rayleigh-Taylor instability [143], where this gradient is caused by gravity or interface acceleration. In the presented case, this term can be written in dimensionless form using (5.5) and (5.16):

$$\frac{p_{0,r}}{\Pi} = \frac{\tau}{(\tau^2 + 1)^{7/2}} + \frac{\text{Re}(1 - 2\tau^2)}{\sqrt{2}(\tau^2 + 1)^{5/2}}, \quad \Pi = \frac{\sqrt{ab}\mu}{2\sqrt{2}H_0^{3/2}\lambda}. \quad (5.23)$$

Function $p_{0,r}(\tau)/\Pi$ is shown in figure 5.7 for various values of the Reynolds number. The inertial effects associated with terms in (5.23), including the Reynolds number, are most pronounced at the very initial stages of the bridge stretching when the substrate velocity (and thus the viscous stresses) is small. This is why, in the case of the liquid bridge stretched by an accelerating substrate, both viscous and inertial effects contribute to the meniscus instability.

For the measurements performed on hydrophobic substrates, the number of fingers was estimated correctly, showing that hydrophobicity does not have a significant effect on the finger instability (see figure 5.8). As shown in figure 3.15, the finger patterns start to emerge before the dewetting begins. Following the previously introduced measurements in §3.2.3 and the consistent estimation from [144], the time scale for the contact line speed is $u_{dewetting} = \sqrt{\sigma/\rho R}$, which is in our experiments of the order of 10^{-2} m/s. The finger formation time scale $\tau = \sqrt{2H_0/a}$ can be estimated using equation (5.16), which yields $\tau \sim 10^{-3} - 10^{-4}$ s. Consequently, the dewetting length for the relevant time scale is of the order $10^{-5} - 10^{-6}$ m and, therefore, too small to affect the finger instability. The difference between the two-time scales provides an approximate validity range of the proposed finger instability theory. Therefore, the introduced prediction of the number of fingers is in good agreement with substrates of different wetting conditions, as shown in figure 5.8, as long as the finger formation and dewetting time scale are not of the same order.

The experimental and theoretically predicted values for N_{\max} are compared in figure 5.8. The agreement is rather good for most of the cases. In some instances, however, the number of fingers is overestimated. Several voids in the liquid bridge have been observed in all these overestimated

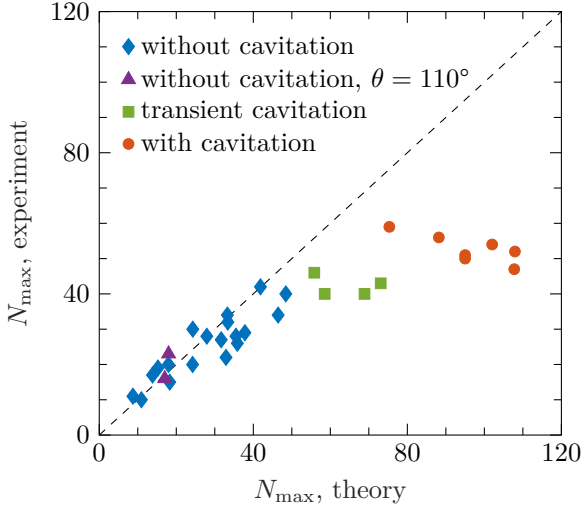


Figure 5.8: Comparison of the measured and theoretically predicted maximum number of fingers N_{\max} . The experiments accompanied by cavitation are marked by circles. The static contact angle of the measurements marked as diamonds, rectangles and circles is $\theta_{\text{static}} = 40^\circ$, while that of the measurements marked as triangle is $\approx \theta = 110^\circ$. The straight dashed line corresponds to perfect agreement between experiment and theory. Reprinted from [21] under CC BY 4.0.

experiments, formed due to cavitation. In some cases, these voids quickly expand, leading to the formation of the structures resembling Voronoi tessellation, as shown in the examples in figure 5.9. These cases are marked as liquid bridge stretching with cavitation.

Several additional cases have also been observed, marked in figure 5.10 as transient cavitation. In these cases, a small number of macroscopic voids emerge far from the interface and then disappear after some time when the stresses are relaxed. It is most probable that, in this transitional case, the flow in the stretched bridge is influenced locally, also near the interface, by the nucleation of microbubbles. Even if the size of the bubbles does not exceed the critical diameter of cavity formation, they can still influence the flow near the moving meniscus.

5 Fingering Instability of the Stretching Bridge

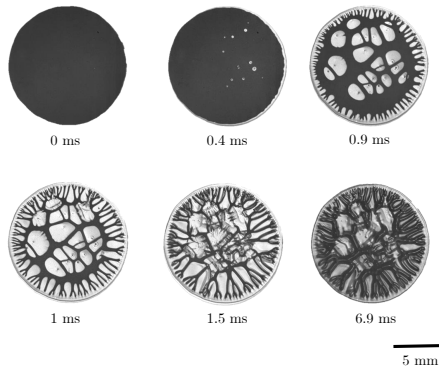


Figure 5.9: Example of the void formation during liquid bridge stretching. The liquid is *Gly80*. The other experimental parameters are: $a = 180 \text{ m/s}^2$, $H_0 = 60 \mu\text{m}$, $\lambda = 0.006$. Reprinted from [21] under CC BY 4.0.

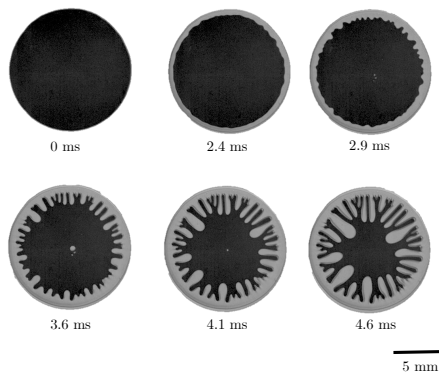


Figure 5.10: Example of the transient cavitation. Several voids are formed in the central part of the liquid bridge and then disappear. The liquid is *Gly80*. The other experimental parameters are: $a = 10 \text{ m/s}^2$, $H_0 = 53 \mu\text{m}$, $\lambda = 0.006$. Reprinted from [21] under CC BY 4.0.

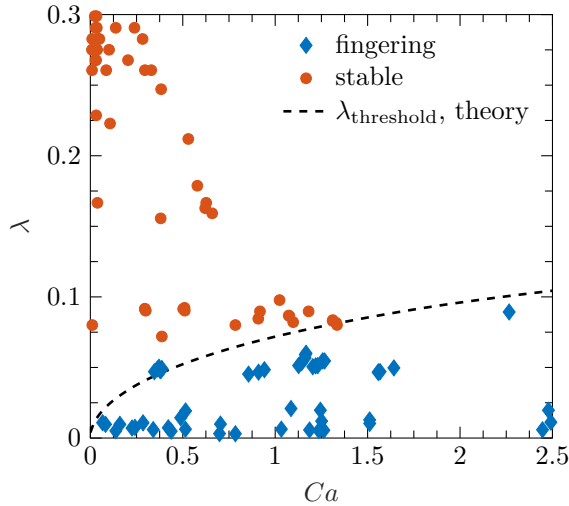


Figure 5.11: Nomogram for the outcomes of liquid bridge stretching for various values of λ and capillary number Ca . The threshold for bridge finger formation is obtained from the full computations for $Re = 0$ of $\lambda_{\text{threshold}}$, corresponding to the condition $N_{\text{max}} = 5$. The approximate solution (5.24) is also shown on the graph, but it is indistinguishable from the results of full computations for $Ca < 1$. Reprinted from [21] under CC BY 4.0.

In figure 5.11, the outcomes of the liquid bridge stretching (stable receding of the meniscus without finger formation or the emergence of apparent finger formation) are shown for various values of λ and Ca . It is not always easy to determine the outcome at the limiting cases near the threshold conditions. A finger formation is identified in this study if more than five periods of the interface waves can be observed. The condition $N_{\text{max}} = 5$ is used as a criterion for selecting the experiments leading to finger formation. This criterion also allows theoretical prediction of the threshold value $\lambda_{\text{threshold}}$ for given capillary and Reynolds numbers. As shown in figure 5.5, the influence of the Reynolds number on the number of the fingers is minor, and, to a first approximation, the threshold value $\lambda_{\text{threshold}}$ is a function only of Ca . For small capillary numbers, the threshold value of λ can be estimated using the approximate solution:

5 Fingering Instability of the Stretching Bridge

(5.21)

$$\lambda_{\text{threshold}} \approx 0.076\sqrt{Ca}, \quad Ca \ll 1, \quad Re = 0. \quad (5.24)$$

It is interesting to note that in the limit $Re = 0$, the same scaling as in (5.24), namely $\lambda_{\text{threshold}} \sim \sqrt{Ca}$, corresponds also to a certain amplitude $G_{\text{threshold}} \approx 1.7\delta_0$ of the shape perturbations $\delta(y, t)$, where δ_0 is the initial shape disturbance. This relation can be obtained from (5.22). Since the initial disturbance δ is very small, the perturbations of the amplitude $G_{\text{threshold}}$ cannot be resolved with the optical system. Note, however, that $G_{\text{threshold}}$ characterizes the amplitude of the perturbations at the predicted time $\tau = \tau_*$, corresponding to the maximum number of fingers. This amplitude continues to grow nearly exponentially in time. This is why in the cases close to the threshold, the fingers can be recognised at times slightly larger than τ_* and thus at radii close to $R/R_0 \approx 0.8$, as shown, for example, for the case $Ca = 0.29$ in figure 5.4.

Therefore, both conditions, a certain number of fingers, and a certain amplitude of the disturbances can be used as conditions for the observable generation of fingers.

5.4 Conclusion

In this study, the pattern formation in a liquid bridge stretched by an accelerating substrate is investigated experimentally and modeled theoretically. The maximum number of fingers is measured for a large range of liquid viscosities, gap widths, and substrate accelerations.

The finger formation process is studied using linear stability analysis for small perturbations of the liquid bridge shape. The theory accounts for the viscous stresses, capillary forces, and inertial effects. The model is developed for a single-sided accelerated substrate. It allows calculations of the amplitude of a specific wavelength on the bridge surface over time as long as $\lambda \ll 1$ and the two-dimensional approximation applies to the flow field. Consequently, a prediction is derived for the number of fingers. The agreement with observations is good, despite the fact that no adjustable parameters have been introduced into the model. The prediction is, however, only applicable if no cavitation occurs. For experimental cases where cavitation occurs, the theory overestimates the number of fingers.

A criterion $\lambda_{\text{threshold}} \approx 0.076\sqrt{Ca}$ has been obtained for the onset of

finger instability. The finger formation assumed a certain number of observable fingers. For lower numbers $N_{\max} < 5$, the instability is perceived as the loss of the asymmetric shape, but not as finger formation. For $N_{\max} < 1$ the flow should be stable.

An alternative condition for finger formation, namely the threshold value for the amplitude of perturbations, leads to the same scaling for the threshold conditions: $\lambda_{\text{threshold}} \sim \sqrt{Ca}$ [45].

6 Pinch-Off Time

In this chapter, the dynamics of the liquid bridge stretching leading to its pinch-off are investigated. Experiments on a fast bridge stretching and pinch-off are performed with the aim to extend the existing semi-empirical model [96] valid for very viscous liquids. The focus lies on describing the pinch-off behavior for smaller initial bridge heights for low and high viscous liquids. The interest for investigating much smaller liquid bridges for high stretching rates derives from printing applications with initial gap heights of only a few nm. For such applications, the knowledge of the pinch-off behavior is highly relevant for the process stability and optimization in order to improve the liquid transfer. The measurements involve different dimensionless initial gap heights with λ (ratio of initial bridge height to initial bridge diameter) and a wide range of accelerations. A semi-empirical model is developed to predict the pinch-off time. Parts of the following sections have been published in [22, 122].

6.1 Dynamics of a Stretched Liquid Bridge - Short times

The flow in the liquid bridge has already been thoroughly described in chapter 3. The phenomena considered in this chapter are shown in figures 3.1 and 3.2.

6.1.1 Governing Dimensionless Parameters

In the initial stage of the bridge stretching, when $D \gg H$ and the radius of curvature of the meniscus is comparable with the distance H , the diameter $D(t)$ of the bridge can be roughly estimated from the mass balance equation

$$D = D_0 \eta^{-1/2}, \quad \eta \equiv \frac{H}{H_0}, \quad (6.1)$$

6 Pinch-Off Time

where η is the dimensionless gap thickness. The experimental data on the middle bridge diameter is compared with the predictions (6.1) in figure. 3.10 and 3.11 for various accelerations and various liquid viscosities. The agreement between the predictions and the measurements is rather good. This agreement indicates that the deformation of the meniscus by the internal stresses or inertia is small in this stage. Such behaviour of the liquid bridge meniscus is observed only in the cases when the flow instability leading to the finger formation is not significant [55, 71–74].

At larger times, the evolution of the bridge diameter deviates from the predicted values in (6.1). This occurs because the inertial stresses in the stretched bridge become significant.

Balance of inertia and viscous forces One important property determining the dynamics of jet stretching is the ratio of the viscous and inertial terms, $\rho U_{\text{substrate}} R / \mu$. It is obvious that since the moving substrate in our experiments accelerates, the role of the inertial terms can increase in time. The inertia-to-viscosity ratio can be expressed as a function of the dimensionless gap thickness η accounting for the kinematic condition $H = H_0 + at^2/2$

$$\frac{\rho U_{\text{substrate}} R}{\mu} = 2 \sqrt{\frac{\eta - 1}{\eta}} Re, \quad \eta > 1. \quad (6.2)$$

where the Reynolds number, defined as

$$Re \equiv \frac{\rho a^{1/2} \lambda^{1/2} R_0^{3/2}}{\mu}, \quad (6.3)$$

and determines therefore the threshold distance $\eta = \eta_\mu^*$ at which the magnitudes of the viscous and inertial stresses are comparable. The distance η_μ can be estimated from (6.2) for high value of the Reynolds number

$$\eta_\mu^* - 1 \sim Re^{-2}, \quad \text{if } Re \gg 1. \quad (6.4)$$

At small Reynolds numbers, $Re \ll 1$, the effect of the viscous stresses is dominant during the entire stretching process since the value of $(\eta - 1)/\eta$ approaches the unity as $\eta \rightarrow \infty$. In these experiments, only the cases $Re \gg 1$ are considered. For example, for all three cases of water stretching shown in figure 3.1, the duration of the initially viscosity dominated

6.2 Dynamics of a Long Liquid Bridge and Jet - Long Times

period is of the order of microseconds. Therefore, the bridge stretching is governed by inertia and surface tension.

At a distance between the substrates exceeding η_μ , the flow in the stretching jet is governed mainly by inertial forces.

Balance of inertia and capillary forces At a certain time instant t_σ the substrate velocity $U_{\text{substrate}} = at$ can exceed the capillary velocity V_σ of the wave propagating along the liquid bridge. Since the capillary velocity determines the speed of propagation of the information about the substrate motion, at larger times ($t > t_\sigma$), the bridge stretching is no longer influenced by the substrate motion.

The velocity of the capillary wave along the liquid bridge can be estimated as

$$V_\sigma \sim \left(\frac{\sigma}{\rho D} \right)^{1/2} = \left(\frac{\sigma \lambda}{\rho H_0} \right)^{1/2} \eta^{1/4}. \quad (6.5)$$

An expression for time $t = [2H_0(\eta - 1)/a]^{1/2}$, obtained from the kinematics of the substrate, moving with the constant acceleration, and the condition $V_\sigma = U_{\text{substrate}}$, is

$$\frac{\eta - 1}{\eta^{1/2}} \sim \frac{\lambda \sigma}{2\rho a H_0^2}, \quad \eta > 1. \quad (6.6)$$

If the right-hand side is much smaller than unity (or in other words if the Weber number is much larger than the unity), the dimensionless distance $\eta = \eta_\sigma^*$ at which the jet starts to stretch freely by inertia is expressed in the asymptotic form

$$\eta_\sigma^* - 1 \sim We^{-1}, \quad We \equiv \frac{\rho a H_0^2}{\lambda \sigma}. \quad (6.7)$$

6.2 Dynamics of a Long Liquid Bridge and Jet - Long Times

At long times, when the length of the liquid bridge is much larger than its diameter, the dynamics of the flow can be described well by a quasi

6 Pinch-Off Time

one-dimensional mass and momentum balance [26]

$$\rho\pi R^2(u_{,t} + uu_{,z}) + F_{,z} = 0, \quad (6.8)$$

$$2R_{,t} + 2uR_{,z} = 0. \quad (6.9)$$

where $R(z, t)$ and $u(z, t)$ are the radius and axial velocity of the jet, which both depend on the axial coordinate z and time t .

The force $F(z, t)$ applied to the jet cross-section accounts for the viscous stresses, the axial component of the surface tension force and the term associated with the Young-Laplace pressure jump

$$F = 3\mu\pi R^2 u_{,z} + \frac{2\pi\sigma R}{(1 + R_{,z}^2)^{3/2}} - \pi R^2 \sigma \kappa, \quad (6.10)$$

$$\kappa = \frac{1 + R_{,z}^2 - RR_{,zz}}{(1 + R_{,z}^2)^{3/2}}. \quad (6.11)$$

At long times the jet stretching is governed by inertial forces. In this stage, a large part of the bridge is stretched as a nearly cylindrical axisymmetric jet.

The asymptotic solution for very fast jet stretching [89]

$$u = \frac{z}{t + \tau}, \quad R = R_0 \frac{\chi}{\sqrt{t + \tau}}, \quad (6.12)$$

exactly satisfies the balance equations (6.10), (6.11). Here τ and χ are some constants which are determined by the initial stage of the bridge stretching, $R_0 = D_0/2$ is the initial jet radius.

Matching the long-time solution with the solution from equation 6.1 for the initial bridge deformation at the dimensionless distance $\eta = \eta^*$ yields

$$\chi = \left[\frac{H_0}{2a(\eta^* - 1)} \right]^{1/4}, \quad \tau = -\frac{(\eta^* - 2)\sqrt{H_0}}{\sqrt{2a}\sqrt{\eta^* - 1}} \quad (6.13)$$

In the present analysis two possible instants for switching to the inertial stretching regime corresponding to η^* are considered, η_σ^* and η_μ^* , discussed in §6.1.

Inertial stretching at long times for higher Reynolds numbers $Re \gg 1$

If the Reynolds number is very high, $Re > We^{1/2}$, the value of η_μ can

be smaller than the value of η_σ . In this case the transition from the initial to the inertial stretching regimes is governed by the liquid viscosity. Substituting η_μ for η_σ in (6.13) and using the expressions (6.4) and (6.12) we obtain

$$R \sim \frac{\lambda^{1/2} R_0^2 \sqrt{\rho}}{\sqrt{\mu} \sqrt{t + \tau}}. \quad (6.14)$$

Inertial stretching at long times for higher Weber numbers, $We \gg 1$
 Substitution of expressions (6.13) in equations (6.10) and (6.12) yields with the help of (6.7) the expression for the jet radius R

$$R \sim \frac{R_0 H_0^{3/4} \rho^{1/4}}{\sigma^{1/4} \lambda^{1/4} \sqrt{t + \tau}}. \quad (6.15)$$

The predicted evolution of the radius R in expression (6.15) does not depend on the substrate acceleration a or the liquid viscosity if the Weber number is much larger than unity. This result is in good agreement with earlier observations in [96]. The linear dependence of the term $1/R^2$ on time predicted in (6.15) is confirmed by the experimental data, shown in figure 6.1.

Let us introduce the radius and time in dimensionless form

$$\tilde{R} = \frac{R}{R_0}, \quad \tilde{t} = \sqrt{\frac{\sigma}{8\rho D_0}}. \quad (6.16)$$

Equation (6.15) with the help of (6.16) yields the following remote asymptotic solution for the jet radius $\tilde{R} \sim t^{-1/2}$. As can be seen in figure 6.2 the value \tilde{R}^{-2} is proportional to \tilde{t} and the data for various Reynolds numbers lie very close to the same straight line.

Nevertheless, the coefficient of proportionality depends significantly on the initial relative gap width λ . This dependence is illustrated in figure 6.3. The influence of the λ value on the evolution of the jet radius is most significant at the early stages of the liquid bridge stretching. In this study, this influence is determined empirically by fitting the experimental data. The resulting expression is written in the form

$$\tilde{R} \sim \lambda^{0.9} \tilde{t}^{-1/2}. \quad (6.17)$$

6 Pinch-Off Time

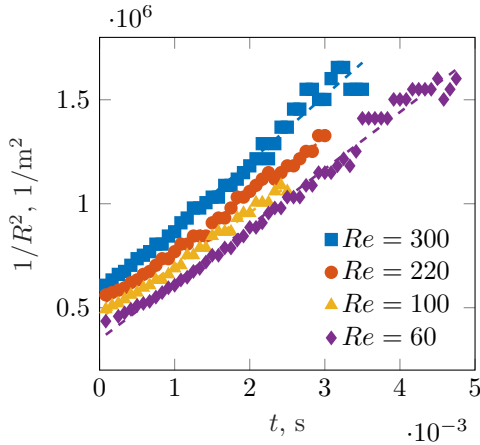


Figure 6.1: Evolution of the value $1/R^2$ as a function of time t for various Reynolds numbers. In all the cases the values of the Weber numbers are high. The substrate acceleration is 180 m/s^2 . The liquids are Gly10, Gly20, Gly40, Gly50 described in Table 2.2. Reprinted from [22] under CC BY 4.0.

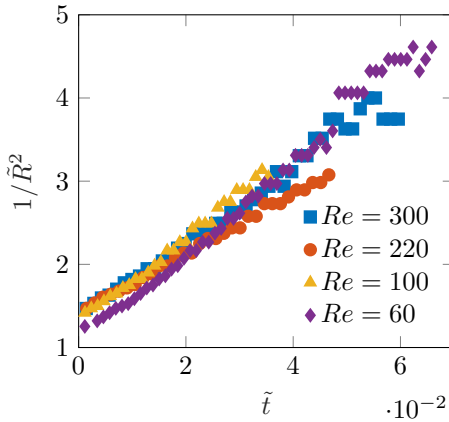


Figure 6.2: Relation of the dimensionless term built on the basis of the jet radius, $1/\tilde{R}^2$ and dimensionless time \tilde{t} for various Reynolds numbers. Reprinted from [22] under CC BY 4.0.

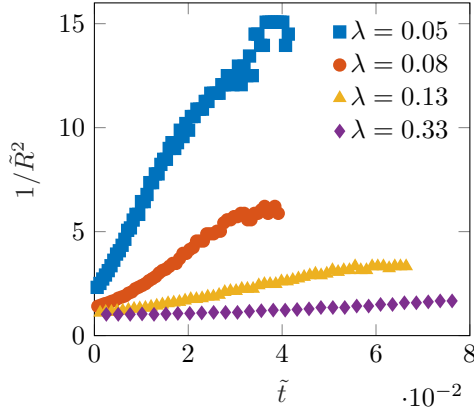


Figure 6.3: Relation of the dimensionless term built on the basis of the jet radius, $1/\tilde{R}^2$ and dimensionless time \tilde{t} for various dimensionless gap widths λ . Reprinted from [22] under CC BY 4.0.

6.3 Modelling the Pinch-Off Time

The values of the pinch-off time for smaller values of λ are shown in Figs. 6.4 and 6.5 as a function of the substrate acceleration a for various liquid viscosities and various values of λ , respectively. The pinch-off time reduces with increasing substrate acceleration but reaches some plateau value for very high substrate accelerations. Moreover, for all accelerations, the pinch-off time increases significantly for higher liquid viscosities. Similar behaviour has been observed recently in [96] for larger values of $\lambda > 0.45$.

Let us consider the pinch-off near the meniscus formed at the solid substrate. The shape of the meniscus is determined mainly by force produced by the jet stretching. The expression for the viscous part of this force, obtained with the help of (6.10) and (6.12) is

$$F_\mu = 3\pi\mu R^2 u_{,z} = \frac{3\pi\mu R_0^2 \chi^2}{(t + \tau)^2}. \quad (6.18)$$

It was shown in [126] that the pinch-off time corresponds to the instant when the viscous force F_μ is comparable with the capillary force σR_U .

6 Pinch-Off Time

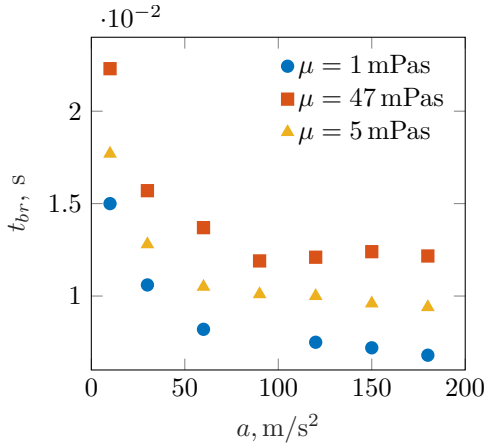


Figure 6.4: Liquid bridge pinch-off times in s as a function of acceleration in m/s^2 for deionised water 1 mPas, 50 % glycerol-water mixture 5 mPas and 80 % glycerol-water mixture 47 mPas with a dimensionless height of $\lambda = 0.2$. Reprinted from [22] under CC BY 4.0.

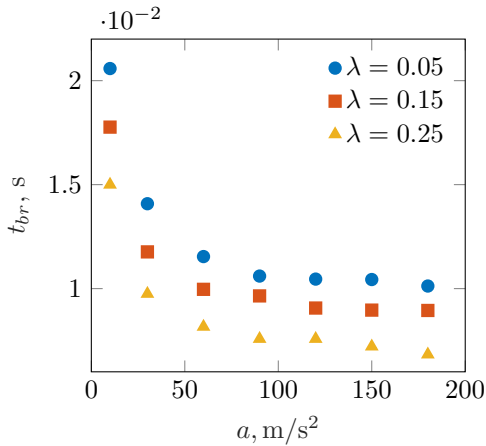


Figure 6.5: Liquid bridge pinch-off times in s as a function of acceleration in m/s^2 different dimensionless heights $\lambda 0.05$, $\lambda 0.15$ and $\lambda 0.25$ for deionised water. Reprinted from [22] under CC BY 4.0.

The pinch-off time is therefore scaled as

$$t_{\text{br}} + \tau \sim \left[\frac{\mu R_0^2 \chi^2}{\sigma R_U} \right]^{1/2}. \quad (6.19)$$

In most of the cases considered in this study, $\tau \ll t_{\text{br}}$ and can be neglected.

Estimating the parameters of the jet stretching at long times from (6.13), equation (6.19) leads to the following expression for the pinch-off time for high viscosity liquid bridges

$$t_{\text{br}} \sim T_\mu \equiv \frac{\lambda^{1/2} \mu^{1/2} \rho^{1/4} R_0^{5/4}}{\sigma^{3/4}}, \quad Re < 1. \quad (6.20)$$

The predicted scale for the pinch-off time does not depend on the substrate acceleration. The timescale (6.20) has been obtained in [96] for relatively high values of the dimensionless gap thickness λ and high viscosity liquids.

For low viscosity liquid bridges $Re \gg 1$, the evolution of the liquid radius is described by expression (6.14). In this case the condition (6.19) yields

$$t_{\text{br}} \sim T_\sigma \equiv \frac{\lambda^{1/2} R_0^{3/2} \rho^{1/2}}{\sigma^{1/2}}, \quad Re \gg 1. \quad (6.21)$$

In figure 6.6 the scaled pinch-off time t_{br}/T_σ is plotted as a function of the Reynolds number. It can be clearly seen that for $Re > 10$ this ratio approaches a constant, $t_{\text{br}}/T_\sigma \approx 3.0$.

For lower values of the Reynolds numbers the viscosity starts to play a more important role and the data for t_{br}/T_σ deviates from the plateau value. For small Reynolds numbers the pinch-off time is scaled well by T_μ defined in (6.20), as demonstrated by the experiments in [96]. In comparison to the measurement performed by [96], shown in red squares in figure 6.6, it is clearly visible that at $Re < 10$ the pinch-off times depart from $t_{\text{br}}/T_\sigma \approx 3.0$ and are no longer predictable with the timescale of T_σ . Measurements from [96] for $Re > 10^2$ confirm our T_σ , and our measurements for $Re < 10$ overlap with the experimental data from [96] for similar Re .

6 Pinch-Off Time

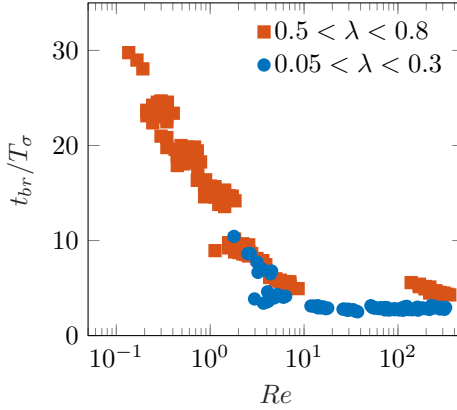


Figure 6.6: The scaled pinch-off time t_{br}/T_σ for different Re and dimensionless heights $0.05 < \lambda < 0.3$ in blue circles and from [96] for $0.5 < \lambda < 0.8$ in red squares. Reprinted from [22] under CC BY 4.0.

6.4 Conclusion

In this section, the kinematics and pinch-off of a single liquid bridge stretched by an accelerating substrate are investigated using a high-speed video system. The main feature compared to previous studies [96] is the relatively thin initial width of the gap between the substrates. This case is relevant to many industrial applications.

The results show that several regimes of bridge stretching can be identified. For high viscous liquids and relatively high dimensionless heights λ , associated with the relatively low Reynolds numbers (since the velocity of the meniscus propagation is inversely proportional to $\sqrt{\lambda}$), the flow is influenced by the viscosity effects. The pinch-off time in these cases is scaled well by viscous time T_μ . This scaling agrees very well with the experimental results [96].

For low viscous liquids and smaller dimensionless heights λ , the time scale is defined mainly by surface tension. In our experiments, the pinch-off time is scaled very well by T_σ if the Reynolds number is much larger than unity.

The new time scale model for smaller bridges allows liquid bridge pinch-

off to be predicted for processes more similar to the geometry of gravure scales in industrial printing applications.

7 Conclusion and Outlook

In the present study, the liquid bridge expansion with high constant accelerations is investigated for different liquid properties and different geometric form conditions. Although the phenomena have been studied for more than a hundred years, the occurring phenomena, especially on an industrially relevant short time and small length scale, are still not fully understood physically.

In this study, the flow in a thin liquid bridge between two substrates generated by the accelerated downward movement of the lower substrate is experimentally investigated and theoretically modeled. The novelty of this study is the combined investigation of high stretching rates at small form factors. In the performed parameter studies, accelerations up to 180 m/s^2 and initial bridge heights of $50 \text{ }\mu\text{m}$ are presented.

An experimental system has been developed to create liquid bridges with initially very small heights and to study their stretching under high accelerations from different perspectives.

Various phenomena occurring during the bridge expansion are experimentally investigated and theoretically modeled in this work. The modeling begins with cavitation events that form within the liquid bridge during bridge expansion. Then, the occurrence threshold and the number of finger patterns at the liquid surface are measured and modeled for a wide range of liquid viscosities, gap widths, and substrate accelerations. Finally, the pinch-off behavior of liquid bridges is investigated in more detail. Although the three phenomena occur on different scales, they are all relevant for industrial processes. The leading actors are always the viscous forces, inertial forces, and surface forces. Throughout all experimental investigations of this study, the time scales were so short that dewetting is negligible.

The investigation starts by deriving the pressure at the substrate surface with the geometry of the liquid bridge from the silhouette measurements. From those, a threshold estimation for the occurrence of cavitation

7 Conclusion and Outlook

events is presented. It can be remarked that next to the cavitation, transient cavitation can also be observed. The estimated pressure can explain the sequence of occurrence of each phenomenon. The transient cavitation phenomenon has already been observed in several other studies, but it was not considered a transitional phenomenon between cavitation events and experiments without cavitation. The transient cavitation phenomenon is particularly sensitive to parameter changes, particularly to the liquid bridge height, and is observed only in a small corridor of parameters. Furthermore, the bubble profile during cavitation is examined, and linear growth and nonlinear contraction are observed. This nonlinear contraction results from the stretching influence on the cavitation bubble. It is shown that cylindrical bubble geometries are produced by stretching motion.

Next, the development of finger patterns is investigated in detail. The formation of finger instabilities through small disturbances of the liquid bridge surface is derived utilizing a pressure estimation along the middle circumference of the bridge and a linear stability analysis. The prediction allows determining amplitudes of a particular wavelength over time as long as $\lambda \ll 1$. From this, a forecast for the number of fingers is derived and validated. The occurrence is predicted in dependency of a modified Ca number.

In the last part of the thesis, the pinch-off behavior of liquid bridge expansions is investigated. The moment of pinch-off can be identified by employing a force balance in the meniscus region. Compared to previous studies, the main novelties are the relatively thin initial width of the gap between the substrates and lower liquid viscosity. The results show that several regimes of bridge elongation can be identified. The results can be estimated for a regime with high viscous liquids and relatively large dimensionless heights λ , combined with the relatively low Reynolds numbers by T_μ . In comparison, low viscous liquids and smaller dimensionless form factors can be represented by T_σ if the Reynolds number is much larger than one. The prediction of the pinch-off time is consistent with its own experimental and literature data.

This work's main findings allow making new theoretical predictions for different phenomena that arise, especially for smaller bridge heights. However, in comparison with printing processes, it is noticeable that other processes such as non-Newtonian liquids, evaporation, or structured surfaces make the process much more complex and that these results cannot be

applied directly. Nevertheless, phenomenological similarities can be seen, for example, in the appearance of finger patterns. Therefore, the findings gained in this study may help to better understand finger formation in printing processes in the future. The results of this work narrow the gap between the generic investigation of liquid bridges with high viscosities and low accelerations towards lower viscosities and higher accelerations. The latter is important for industrial applications such as ice crystal icing in aircraft engines at low viscosity or printing electronic components.

To better represent the industrial application with the generic experiment, the liquids' properties, especially non-Newtonian liquid properties, must be investigated in subsequent studies. Deviating rheology models can have new influences on the phenomena presented here and lead to new insights into the processes. Furthermore, the interaction of several bridges, especially under the influence of the doctor blade and the printing plates, has to be investigated in the future. The doctoring process plays an important role, especially when investigating the interaction of multiple liquid bridges. This will allow insights into processes regarding comparable conditions with similar physical boundary conditions between the generic stretching experiments and industrial printing processes.

Bibliography

- [1] D. Jarrahbashi, W. A. Sirignano, P. P. Popov, and F. Hussain, “Early spray development at high gas density: Hole, ligament and bridge formations,” *Journal of Fluid Mechanics*, vol. 792, pp. 186–231, 2016.
- [2] B. Ambravaneswaran and O. A. Basaran, “Effects of insoluble surfactants on the nonlinear deformation and breakup of stretching liquid bridges,” *Physics of Fluids*, vol. 11, no. 5, pp. 997–1015, 1999.
- [3] P. Marmottant and E. Villermaux, “On spray formation,” *Journal of Fluid Mechanics*, vol. 498, pp. 73–111, 2004.
- [4] J. M. Gordillo and S. Gekle, “Generation and breakup of Worthington jets after cavity collapse. Part 2. Tip breakup of stretched jets,” *Journal of Fluid Mechanics*, vol. 663, pp. 331–346, 2010.
- [5] A. P. Gaylard, K. Kirwan, and D. A. Lockerby, “Surface contamination of cars: A review,” *Proceedings of the Institution of Mechanical Engineers, Part D: Journal of Automobile Engineering*, vol. 231, no. 9, pp. 1160–1176, 2017.
- [6] C. Xu, Z. Zhang, J. Fu, and Y. Huang, “Study of pinch-off locations during drop-on-demand inkjet printing of viscoelastic alginate solutions,” *Langmuir*, vol. 33, no. 20, pp. 5037–5045, 2017.
- [7] T. K. Kololuoma, M. Tuomikoski, T. Makela, J. Heilmann, T. Haring, J. Kallioinen, J. Hagberg, I. Kettunen, and H. K. Kopola, “Towards roll-to-roll fabrication of electronics, optics, and optoelectronics for smart and intelligent packaging,” in *Emerging Optoelectronic Applications*, vol. 5363. SPIE, 2004, pp. 77 – 85.
- [8] W. Gao, H. Ota, D. Kiriya, K. Takei, and A. Javey, “Flexible electronics toward wearable sensing,” *Accounts of Chemical Research*, vol. 52, no. 3, pp. 523–533, 2019.

Bibliography

- [9] R. Abbel, Y. Galagan, and P. Groen, “Roll-to-roll fabrication of solution processed electronics,” *Advanced Engineering Materials*, vol. 20, no. 8, p. 1701190, 2018.
- [10] J. Willmann, D. Stocker, and E. Dörsam, “Characteristics and evaluation criteria of substrate-based manufacturing. Is roll-to-roll the best solution for printed electronics?” *Organic Electronics*, vol. 15, no. 7, pp. 1631–1640, 2014.
- [11] D. R. Gamota, P. Brazis, K. Kalyanasundaram, and J. Zhang, *Printed organic and molecular electronics*. Springer Science & Business Media, 2013.
- [12] C. Bodenstern, “Untersuchung des Tampondrucks und dessen Kantengenauigkeit für die Anwendung in der gedruckten Elektronik,” Ph.D. dissertation, Technische Universität Darmstadt, Darmstadt, Germany, 2020.
- [13] S. Griesheimer, “Farbspaltungsphänomene von Druckfarben an strukturierten Oberflächen am Beispiel des Flexodrucks,” Ph.D. dissertation, Technische Universität Darmstadt, Darmstadt, Germany, 2014.
- [14] J. Schäfer, I. V. Roisman, H. M. Sauer, and E. Dörsam, “Millisecond fluid pattern formation in the nip of a gravure printing machine,” *Colloids and Surfaces A: Physicochemical and Engineering Aspects*, vol. 575, pp. 222–229, 2019.
- [15] S. Kumar, “Liquid transfer in printing processes: liquid bridges with moving contact lines,” *Annual Review of Fluid Mechanics*, vol. 47, pp. 67–94, 2015.
- [16] T. P. Bartkus, J.-C. Tsao, and P. M. Struk, “Analysis of experimental ice accretion data and assessment of a thermodynamic model during ice crystal icing,” *SAE Technical Paper*, no. 2019-01-2016, 2019.
- [17] J. Banke, “Airplane plus heat plus ice equals mystery,” NASA Aeronautics Research Mission Directorate, Topics: Aeronautics, 2017, Accessed: 15th September 2020. [Online]. Available: https://www.nasa.gov/topics/aeronautics/features/ice_mystery.html

- [18] H. E. Addy and J. P. Veres, “An overview of NASA engine ice-crystal icing research,” SAE Technical Paper, Tech. Rep., 2011.
- [19] NASA Video. Theory of Ice Crystal Engine Icing. Accessed: 25th September 2020. [Online]. Available: https://youtu.be/_ps7-9KfMEc?t=29
- [20] *Media Usage Guidelines*, NASA, Accessed: 25th September 2020. [Online]. Available: <https://www.nasa.gov/multimedia/guidelines/index.html>
- [21] S. Brulin, I. V. Roisman, and C. Tropea, “Fingering instability of a viscous liquid bridge stretched by an accelerating substrate,” *Journal of Fluid Mechanics*, vol. 899, 2020.
- [22] S. Brulin, C. Tropea, and I. V. Roisman, “Pinch-off of a viscous liquid bridge stretched with high Reynolds numbers,” *Colloids and Surfaces A: Physicochemical and Engineering Aspects*, vol. 587, p. 124271, 2020.
- [23] J. Plateau, “The figures of equilibrium of a liquid mass,” *The Annual Report of the Smithsonian Institution*, pp. 338–369, 1864.
- [24] J. Stefan, “Versuche über die scheinbare Adhäsion,” *Annalen der Physik*, vol. 230, no. 2, pp. 316–318, 1875.
- [25] L. Rayleigh, “On the instability of jets,” *Proceedings of the Royal Society A – Mathematical, Physical and Engineering Sciences*, vol. 10, pp. 4–13, 1878.
- [26] A. L. Yarin, *Free liquid jets and films: hydrodynamics and rheology*. Longman & Wiley, 1993.
- [27] E. Villermaux, “Fragmentation,” *Annual Review of Fluid Mechanics*, vol. 39, pp. 419–446, 2007.
- [28] J. Eggers and E. Villermaux, “Physics of liquid jets,” *Reports on Progress in Physics*, vol. 71, no. 3, p. 036601, 2008.
- [29] J. Eggers, “Nonlinear dynamics and breakup of free-surface flows,” *Reviews of Modern Physics*, vol. 69, no. 3, p. 865, 1997.
- [30] R. M. Schulkes, “Dynamics of liquid jets revisited,” *Journal of Fluid Mechanics*, vol. 250, pp. 635–650, 1993.

Bibliography

- [31] D. T. Papageorgiou, “On the breakup of viscous liquid threads,” *Physics of Fluids*, vol. 7, no. 7, pp. 1529–1544, 1995.
- [32] F. Parveen, S. Josset, C. Briens, and F. Berruti, “Effect of size and density on agglomerate breakage in a fluidized bed,” *Powder Technology*, vol. 231, pp. 102–111, 2012.
- [33] D. Rossetti, X. Pepin, and S. J. Simons, “Rupture energy and wetting behavior of pendular liquid bridges in relation to the spherical agglomeration process,” *Journal of Colloid and Interface Science*, vol. 261, no. 1, pp. 161–169, 2003.
- [34] P. Darabi, T. Li, K. Pougatch, M. Salcudean, and D. Grecov, “Modeling the evolution and rupture of stretching pendular liquid bridges,” *Chemical Engineering Science*, vol. 65, no. 15, pp. 4472–4483, 2010.
- [35] Y. Chen, W. Gao, C. Zhang, and Y. Zhao, “Three-dimensional splitting microfluidics,” *Lab Chip*, vol. 16, no. 8, pp. 1332–1339, 2016.
- [36] Y. Chen, X. Liu, and M. Shi, “Hydrodynamics of double emulsion droplet in shear flow,” *Applied Physics Letters*, vol. 102, no. 5, p. 051609, 2013.
- [37] T. Sridhar, V. Tirtaatmadja, D. Nguyen, and R. Gupta, “Measurement of extensional viscosity of polymer solutions,” *Journal of Non-Newtonian Fluid Mechanics*, vol. 40, no. 3, pp. 271–280, 1991.
- [38] G. H. McKinley and T. Sridhar, “Filament-stretching rheometry of complex fluids,” *Annual Review of Fluid Mechanics*, vol. 34, no. 1, pp. 375–415, 2002.
- [39] L. E. Rodd, T. P. Scott, J. J. Cooper-White, and G. H. McKinley, “Capillary break-up rheometry of low-viscosity elastic fluids,” *Applied Rheology*, vol. 15, pp. 12–27, 2004.
- [40] R. Kröger, S. Berg, A. Delgado, and H. Rath, “Stretching behaviour of large polymeric and Newtonian liquid bridges in Plateau simulation,” *Journal of Non-Newtonian Fluid Mechanics*, vol. 45, no. 3, pp. 385–400, 1992.
- [41] R. Kröger and H. Rath, “Velocity and elongation rate distributions in stretched polymeric and Newtonian liquid bridges,” *Journal of Non-Newtonian Fluid Mechanics*, vol. 57, no. 2-3, pp. 137–153, 1995.

- [42] J. Eggers, “Universal pinching of 3D axisymmetric free-surface flows,” *Physical Review Letters*, vol. 71, pp. 3458–3460, 1993.
- [43] L. Vincent, L. Duchemin, and S. Le Dizès, “Forced dynamics of a short viscous liquid bridge,” *Journal of Fluid Mechanics*, vol. 761, pp. 220–240, 2014.
- [44] S. Dodds, M. S. Carvalho, and S. Kumar, “The dynamics of three-dimensional liquid bridges with pinned and moving contact lines,” *Journal of Fluid Mechanics*, vol. 707, pp. 521–540, 2012.
- [45] M. S. Plesset and A. Prosperetti, “Bubble dynamics and cavitation,” *Annual Review of Fluid Mechanics*, vol. 9, no. 1, pp. 145–185, 1977.
- [46] C. E. Brennen, *Cavitation and bubble dynamics*. Cambridge University Press, 2014.
- [47] W. Heller, “Hydrodynamische Effekte unter besonderer Berücksichtigung der Wasserqualität und ihre Messverfahren,” Ph.D. dissertation, Technische Universität Dresden, Dresden, Germany, 2005.
- [48] C. Creton and M. Ciccotti, “Fracture and adhesion of soft materials: a review,” *Reports on Progress in Physics*, vol. 79, no. 4, p. 046601, 2016.
- [49] W. F. Busse, “Physics of rubber as related to the automobile,” *Journal of Applied Physics*, vol. 9, no. 7, pp. 438–451, 1938.
- [50] F. L. Yezley, “Adhesion of neoprene to metal,” *Industrial & Engineering Chemistry*, vol. 31, no. 8, pp. 950–956, 1939.
- [51] A. Gent and P. Lindley, “Internal rupture of bonded rubber cylinders in tension,” *Proceedings of the Royal Society of London. Series A. Mathematical and Physical Sciences*, vol. 249, no. 1257, pp. 195–205, 1959.
- [52] A. Gent and D. Tompkins, “Surface energy effects for small holes or particles in elastomers,” *Journal of Polymer Science Part A-2: Polymer Physics*, vol. 7, no. 9, pp. 1483–1487, 1969.
- [53] J. M. Ball, “Discontinuous equilibrium solutions and cavitation in nonlinear elasticity,” *Philosophical Transactions of the Royal Society of London. Series A, Mathematical and Physical Sciences*, vol. 306, no. 1496, pp. 557–611, 1982.

Bibliography

- [54] S. B. Hutchens, S. Fakhouri, and A. J. Crosby, “Elastic cavitation and fracture via injection,” *Soft Matter*, vol. 12, no. 9, pp. 2557–2566, 2016.
- [55] J. Nase, D. Derks, and A. Lindner, “Dynamic evolution of fingering patterns in a lifted Hele-Shaw cell,” *Physics of Fluids*, vol. 23, no. 12, p. 123101, 2011.
- [56] S. Poivet, F. Nallet, C. Gay, and P. Fabre, “Cavitation-induced force transition in confined viscous liquids under traction,” *Europhysics Letters*, vol. 62, no. 2, pp. 244–250, Apr. 2003.
- [57] H. Hang-Sheng and R. Abeyaratne, “Cavitation in elastic and elastic-plastic solids,” *Journal of the Mechanics and Physics of Solids*, vol. 40, no. 3, pp. 571–592, 1992.
- [58] C. Fond, “Cavitation criterion for rubber materials: a review of void-growth models,” *Journal of Polymer Science Part B: Polymer Physics*, vol. 39, no. 17, pp. 2081–2096, 2001.
- [59] O. Lopez-Pamies, “Onset of cavitation in compressible, isotropic, hyperelastic solids,” *Journal of Elasticity*, vol. 94, no. 2, p. 115, 2009.
- [60] S. Poivet, F. Nallet, C. Gay, J. Teisseire, and P. Fabre, “Force response of a viscous liquid in a probe-tack geometry: fingering versus cavitation,” *The European Physical Journal E*, vol. 15, no. 2, pp. 97–116, 2004.
- [61] P. G. Saffman and G. I. Taylor, “The penetration of a fluid into a porous medium or Hele-Shaw cell containing a more viscous liquid,” *Proceedings of the Royal Society of London. Series A. Mathematical and Physical Sciences*, vol. 245, no. 1242, pp. 312–329, 1958.
- [62] K. V. McCloud and J. V. Maher, “Experimental perturbations to Saffman-Taylor flow,” *Physics Reports*, vol. 260, no. 3, pp. 139–185, 1995.
- [63] S. Mora and M. Manna, “Saffman-Taylor instability for generalized Newtonian fluids,” *Physical Review E*, vol. 80, no. 1, p. 016308, 2009.

- [64] K. J. Mly, F. Boger, J. Feder, T. Jssang, and P. Meakin, “Dynamics of viscous-fingering fractals in porous media,” *Physical Review A*, vol. 36, no. 1, p. 318, 1987.
- [65] J. R. de Bruyn, P. Habdas, and S. Kim, “Fingering instability of a sheet of yield-stress fluid,” *Physical Review E*, vol. 66, no. 3, p. 031504, 2002.
- [66] T. Maxworthy, “Experimental study of interface instability in a Hele-Shaw cell,” *Physical Review A*, vol. 39, no. 11, p. 5863, 1989.
- [67] C.-W. Park, S. Gorell, and G. Homsy, “Two-phase displacement in Hele-Shaw cells: experiments on viscously driven instabilities,” *Journal of Fluid Mechanics*, vol. 141, pp. 275–287, 1984.
- [68] L. Schwartz, “Stability of Hele-Shaw flows: The wetting-layer effect,” *The Physics of Fluids*, vol. 29, no. 9, pp. 3086–3088, 1986.
- [69] L. Paterson, “Radial fingering in a Hele-Shaw cell,” *Journal of Fluid Mechanics*, vol. 113, pp. 513–529, 1981.
- [70] T. Ward, “Capillary-pressure driven adhesion of rigid-planar surfaces,” *Journal of Colloid and Interface Science*, vol. 354, no. 2, pp. 816–824, 2011.
- [71] M. B. Amar and D. Bonn, “Fingering instabilities in adhesive failure,” *Physica D: Nonlinear Phenomena*, vol. 209, no. 1-4, pp. 1–16, 2005.
- [72] E. O. Dias and J. A. Miranda, “Determining the number of fingers in the lifting Hele-Shaw problem,” *Physical Review E*, vol. 88, no. 4, p. 043002, 2013.
- [73] M. J. Shelley, F.-R. Tian, and K. Wlodarski, “Hele-Shaw flow and pattern formation in a time-dependent gap,” *Nonlinearity*, vol. 10, no. 6, p. 1471, 1997.
- [74] S. Sinha, S. K. Kabiraj, T. Dutta, and S. Tarafdar, “Radially interrupted viscous fingers in a lifting Hele-Shaw cell,” *The European Physical Journal B-Condensed Matter and Complex Systems*, vol. 36, no. 3, pp. 297–300, 2003.

Bibliography

- [75] S. H. Spiegelberg and G. H. McKinley, “Stress relaxation and elastic decohesion of viscoelastic polymer solutions in extensional flow,” *Journal of Non-Newtonian Fluid Mechanics*, vol. 67, pp. 49–76, 1996.
- [76] O. A. Fadoul and P. Coussot, “Saffman–Taylor instability in yield stress fluids: Theory–experiment comparison,” *Fluids*, vol. 4, no. 1, p. 53, 2019.
- [77] P. H. Anjos, E. O. Dias, and J. A. Miranda, “Inertia-induced dendriticlike patterns in lifting Hele-Shaw flows,” *Physical Review Fluids*, vol. 2, no. 1, p. 014003, 2017.
- [78] H. A. Stone, “Philip Saffman and viscous flow theory,” *Journal of Fluid Mechanics*, vol. 409, pp. 165–183, 2000.
- [79] L. Rayleigh, “Analytic solutions of the Rayleigh equation for linear density profiles,” *Proceedings of the London Mathematical Society*, vol. 14, pp. 170–177, 1883.
- [80] G. I. Taylor, “The instability of liquid surfaces when accelerated in a direction perpendicular to their planes. I,” *Proceedings of the Royal Society of London. Series A. Mathematical and Physical Sciences*, vol. 201, no. 1065, pp. 192–196, 1950.
- [81] A. Lindner, P. Coussot, and D. Bonn, “Viscous fingering in a yield stress fluid,” *Physical Review Letters*, vol. 85, no. 2, p. 314, 2000.
- [82] J. Plateau, “I. Experimental and theoretical researches on the figures of equilibrium of a liquid mass withdrawn from the action of gravity. –Third series,” *The London, Edinburgh, and Dublin Philosophical Magazine and Journal of Science*, vol. 14, no. 90, pp. 1–22, 1857.
- [83] G. Mason, “An experimental determination of the stable length of cylindrical liquid bubbles,” *Journal of Colloid and Interface Science*, vol. 32, no. 1, pp. 172–176, 1970.
- [84] R. Gillette and D. Dyson, “Stability of fluid interfaces of revolution between equal solid circular plates,” *The Chemical Engineering Journal*, vol. 2, no. 1, pp. 44–54, 1971.

- [85] A. Sanz and I. Martinez, “Minimum volume for a liquid bridge between equal disks,” *Journal of Colloid and Interface Science*, vol. 93, no. 1, pp. 235–240, 1983.
- [86] M. J. Russo and P. H. Steen, “Instability of rotund capillary bridges to general disturbances: experiment and theory,” *Journal of Colloid and Interface Science*, vol. 113, no. 1, pp. 154–163, 1986.
- [87] L. A. Slobozhanin and J. M. Perales, “Stability of liquid bridges between equal disks in an axial gravity field,” *Physics of Fluids A: Fluid Dynamics*, vol. 5, no. 6, pp. 1305–1314, 1993.
- [88] J. Meseguer and A. Sanz, “Numerical and experimental study of the dynamics of axisymmetric slender liquid bridges,” *Journal of Fluid Mechanics*, vol. 153, pp. 83–101, 1985.
- [89] I. Frankel and D. Weihs, “Stability of a capillary jet with linearly increasing axial velocity (with application to shaped charges),” *Journal of Fluid Mechanics*, vol. 155, pp. 289–307, 1985.
- [90] R. Kröger, S. Berg, A. Delgado, and H. Rath, “Stretching behavior of large polymeric and Newtonian liquid bridges in Plateau simulation,” *Journal of Non-Newtonian Fluid Mechanics*, vol. 45, p. 385, 1992.
- [91] X. Zhang, R. Padgett, and O. Basaran, “Nonlinear deformation and breakup of stretching liquid bridges,” *Journal of Fluid Mechanics*, vol. 329, pp. 207–245, 1996.
- [92] Y.-C. Liao, E. I. Franses, and O. A. Basaran, “Deformation and breakup of a stretching liquid bridge covered with an insoluble surfactant monolayer,” *Physics of Fluids*, vol. 18, no. 2, p. 022101, 2006.
- [93] O. E. Yildirim and O. A. Basaran, “Deformation and breakup of stretching bridges of Newtonian and shear-thinning liquids: comparison of one- and two-dimensional models,” *Chemical Engineering Science*, vol. 56, no. 1, pp. 211–233, 2001.
- [94] S. Dodds, “Stretching and slipping liquid bridges: liquid transfer in industrial printing,” Ph.D. dissertation, University of Minnesota, 2011.

Bibliography

- [95] S. Dodds, M. Carvalho, and S. Kumar, “Stretching liquid bridges with moving contact lines: The role of inertia,” *Phys. Fluids*, vol. 23, p. 092101, 2011.
- [96] C. M. Weickgenannt, I. V. Roisman, and C. Tropea, “Pinch-off of a stretching viscous filament and drop transport,” *New Journal of Physics*, vol. 17, no. 8, p. 083059, 2015.
- [97] *Manual Linear Drive*, A-Drive Technology GmbH, September, 10th, 2020. [Online]. Available: http://www.a-drive.de/download/adrive_image_en.pdf
- [98] N.-S. Cheng, “Formula for the viscosity of a glycerol- water mixture,” *Industrial & Engineering Chemistry Research*, vol. 47, no. 9, pp. 3285–3288, 2008.
- [99] I. I. Adamenko, L. A. Bulavin, V. Ilyin, S. A. Zelinsky, and K. O. Moroz, “Anomalous behavior of glycerol–water solutions,” *Journal of Molecular Liquids*, vol. 127, no. 1-3, pp. 90–92, 2006.
- [100] P. J. Linstrom and W. G. Mallard, *Thermophysical Properties of Fluid Systems, NIST Standard Reference Database No. 69*, National Institute of Standards and Technology, 2018. [Online]. Available: <http://webbook.nist.gov>
- [101] T. F. Young and W. D. Harkins, “Surface tension data for certain pure liquids between 0 and 360 °C and for all types of solutions at all temperatures,” *International Critical Tables*, vol. 4, p. 446, 1928.
- [102] A. Pfennig, W. Schabel, and H. Wolf, “Properties of multicomponent fluid mixtures,” in *VDI Heat Atlas*. Springer, 2010, pp. 513–550.
- [103] T. Young, “III. An essay on the cohesion of fluids,” *Philosophical Transactions of the Royal Society*, vol. 95, pp. 65–87, 1805.
- [104] P.-G. De Gennes, F. Brochard-Wyart, and D. Quéré, *Capillarity and wetting phenomena: drops, bubbles, pearls, waves*. Springer Science & Business Media, 2013.
- [105] S. Wilson, “A note on the measurement of dynamic contact angles,” *Journal of Colloid and Interface Science*, vol. 51, no. 3, pp. 532–534, 1975.

- [106] M. Hartmann and S. Hardt, “Stability of evaporating droplets on chemically patterned surfaces,” *Langmuir*, vol. 35, no. 14, pp. 4868–4875, 2019.
- [107] Hamilton, “Hamilton Needle 7105 Product Sheet,” Accessed: 10th September 2020. [Online]. Available: <https://www.hamiltoncompany.com/laboratory-products/product-specs/53126>
- [108] D. M. Campana and M. S. Carvalho, “Liquid transfer from single cavities to rotating rolls,” *Journal of Fluid Mechanics*, vol. 747, pp. 545–571, 2014.
- [109] C. Tropea and A. L. Yarin, *Springer Handbook of Experimental Fluid Mechanics*. Springer Science & Business Media, 2007.
- [110] Photron, “Photron SA-X2,” Accessed: 12th July 2019. [Online]. Available: https://photron.com/wp-content/uploads/2019/12/SA-X2_19.12.17_compressed.pdf
- [111] PCO, “pco.edge 5.5,” Accessed: 18th April 2020. [Online]. Available: https://www.pco.de/fileadmin/user_upload/pco-product_sheets/pco.edge_55_data_sheet.pdf
- [112] *Telecentric Lense Image*, Opto Engineering, Accessed: 1st October 2020. [Online]. Available: https://www.opto-e.com/media/timthumb.php?src=media/company/bitc_tech_perspective.jpg&w=1200
- [113] *Datasheet of Lens Model TC16M192*, Opto Engineering, Accessed: 15th September 2020. [Online]. Available: <https://www.opto-e.de/produkte/tz-objektiv-fur-sehr-grosse-detektoren-TC16M192>
- [114] *Datasheet of Lens Model TC16M009*, Opto Engineering, Accessed: 15th September 2020. [Online]. Available: <https://www.opto-e.de/produkte/tz-objektiv-fur-sehr-grosse-detektoren-TC16M009>
- [115] D. Li and J. Tian, “An accurate calibration method for a camera with telecentric lenses,” *Optics and Lasers in Engineering*, vol. 51, no. 5, pp. 538–541, 2013.
- [116] Navitar, “High mag zoom and fixed lenses.” [Online]. Available: <https://navitar.com/products/imaging-optics/high-magnification-imaging/12x-zoom/>

Bibliography

- [117] D. Biole, M. Wang, and V. Bertola, “Assessment of direct image processing methods to measure the apparent contact angle of liquid drops,” *Experimental Thermal and Fluid Science*, vol. 76, pp. 296–305, 2016.
- [118] J. Canny, “A computational approach to edge detection,” *IEEE Transactions on Pattern Analysis and Machine Intelligence*, vol. PAMI-8, no. 6, pp. 679–698, 1986.
- [119] B. D. Lucas, T. Kanade *et al.*, “An iterative image registration technique with an application to stereo vision,” in *Proceedings 7th International Joint Conference on Artificial Intelligence*. Vancouver, British Columbia, 1981.
- [120] B. D. Lucas, “Generalized image matching by the method of differences,” Ph.D. dissertation, Carnegie-Mellon University, 1984.
- [121] T. Zhang and C. Y. Suen, “A fast parallel algorithm for thinning digital patterns,” *Communications of the ACM*, vol. 27, no. 3, pp. 236–239, 1984.
- [122] S. Brulin, I. V. Roisman, and C. Tropea, “Breakup of a stretching liquid bridge,” in *International Conference in Aerospace for Young Scientists*, 2017.
- [123] S. Brulin, I. V. Roisman, and C. Tropea, “Dewetting behaviour of liquid bridges stretched by an accelerated plate,” in *Triennial International Conference on Liquid Atomization and Spray Systems*, 2010.
- [124] I. V. Roisman, “Dynamics of inertia dominated binary drop collisions,” *Physics of Fluids*, vol. 16, no. 9, pp. 3438–3449, 2004.
- [125] S. Jegust, “Optische Volumenbestimmung aufgebrochener Flüssigkeitsbrücken,” Bachelor Thesis, 22th May 2018.
- [126] C. M. Weickgenannt, “Rapid stretching of liquid bridges by an accelerated plate,” Ph. D. Thesis, Technische Universität Darmstadt, Darmstadt, Germany, 2015.
- [127] H. Chen, T. Tang, and A. Amirfazli, “Effects of surface wettability on fast liquid transfer,” *Physics of Fluids*, vol. 27, no. 11, p. 112102, 2015.

- [128] S. Dodds, M. d. S. Carvalho, and S. Kumar, “Stretching and slipping of liquid bridges near plates and cavities,” *Physics of Fluids*, vol. 21, no. 9, p. 092103, 2009.
- [129] E. Dussan, “On the spreading of liquids on solid surfaces: static and dynamic contact lines,” *Annual Review of Fluid Mechanics*, vol. 11, no. 1, pp. 371–400, 1979.
- [130] L. Tanner, “The spreading of silicone oil drops on horizontal surfaces,” *Journal of Physics D: Applied Physics*, vol. 12, no. 9, p. 1473, 1979.
- [131] O. Voinov, “Hydrodynamics of wetting,” *Fluid Dynamics*, vol. 11, no. 5, pp. 714–721, 1976.
- [132] R. L. Hoffman, “A study of the advancing interface. I. Interface shape in liquid-gas systems,” *Journal of Colloid and Interface Science*, vol. 50, no. 2, pp. 228–241, 1975.
- [133] L. D. Landau and E. M. Lifshitz, *Fluid Mechanics*. Pergamon Press, 1959, (transl. J. B. Sykes & W. H. Reid).
- [134] H. K. Moffatt, “Viscous and resistive eddies near a sharp corner,” *Journal of Fluid Mechanics*, vol. 18, no. 1, pp. 1–18, 1964.
- [135] D. Anderson and S. Davis, “Two-fluid viscous flow in a corner,” *Journal of Fluid Mechanics*, vol. 257, pp. 1–31, 1993.
- [136] P. Gaskell, M. Savage, J. Summers, and H. Thompson, “Modelling and analysis of meniscus roll coating,” *Journal of Fluid Mechanics*, vol. 298, pp. 113–137, 1995.
- [137] J. Bohr, S. Brunak, and T. Nørretranders, “Viscous trees and voronoi-structure formation in expanding systems,” *Europhysics Letters*, vol. 25, no. 4, p. 245, 1994.
- [138] E. O. Dias and J. A. Miranda, “Wavelength selection in Hele-Shaw flows: A maximum-amplitude criterion,” *Physical Review E*, vol. 88, no. 1, p. 013016, 2013.
- [139] J. Meyer, “Zur Kenntnis des negativen Druckes in Flüssigkeiten,” *Zeitschrift für Elektrochemie und angewandte physikalische Chemie*, vol. 17, no. 17, pp. 743–745, 1911.

Bibliography

- [140] E. Limpert, W. A. Stahel, and M. Abbt, “Log-normal distributions across the sciences,” *BioScience*, vol. 51, no. 5, pp. 341–352, 2001.
- [141] W. Xu, I. Tzanakis, P. Srirangam, S. Terzi, W. Mirihanage, D. Eskin, R. Mathiesen, A. Horsfield, and P. Lee, “In situ synchrotron radiography of ultrasound cavitation in a molten al-10cu alloy,” in *TMS 2015 144th Annual Meeting & Exhibition*. Springer, 2015, pp. 61–66.
- [142] S. Brulin, J. Schäfer, I. V. Roisman, and E. Dörsam, “Analysis of contact line behaviour during liquid bridge stretching and its effect on residual volumes after break-up,” in *10th International Conference on Multiphase Flow*, 2019.
- [143] S. Chandrasekhar, *Hydrodynamic and hydromagnetic stability*. Courier Corporation, 2013.
- [144] B. Qian and K. S. Breuer, “The motion, stability and breakup of a stretching liquid bridge with a receding contact line,” *Journal of Fluid Mechanics*, vol. 666, pp. 554–572, 2011.

List of Figures

1.1	Examples of printed electronics. (a) A roll-to-roll manufacturing process PolyIC, Germany. (b) A temperature sensor Thin Film Electronics ASA, Norway. (c) An active matrix backplane circuit; the inset is an optical micrograph of a typical transistor. Reprinted from [15] with permission of Annual Reviews, Inc.	2
1.2	Ice accretion on a stator blade. Due to elevated temperatures inside the jet engine, a thin film of liquid water can form, allowing the accumulation of additional ice crystals. Reprinted from [19] according to the NASA Media Guidelines [20].	4
2.1	Sketch of the measurement set-up with data connections and the sensor system used.	14
2.2	Sketch of the kinematics of a printing cylinder.	15
2.3	Sketch of the measurement set-up including the alignment systems in isometric view.	16
2.4	Sketch of the measurement set-up including optical paths in side view. Adapted from [21] under CC BY 4.0.	17
2.5	Validation of the linear drives stretching rate. Comparing the position of the linear drive carriage with the ideal position for each acceleration.	18
2.6	Validation of the linear drives stretching rate. Comparing the accelerations determined from each position curve through a polynomial fit and their respective 95% confidence intervals.	19
2.7	Comparing the experimentally determined dynamic viscosity with the prediction based on [98] for <i>Gly</i> 10 up to <i>Gly</i> 80.	22
2.8	Contact angle measurement of distilled water applied to aluminium substrate.	23
2.9	Interferometric measurement of a glass substrates surface after several measurement series.	26

List of Figures

2.10 Showing a liquid bridge profile from top. The measurements are performed with 5 μl of deionised water before a) and after alignment b). 28

2.11 Comparison of the lenses: a), two images are shown taken by a standard entocentric optical system. On the left, the inside of a tube is apparent, revealing the typical entocentric perspective errors. On the right side, the screw thread is not resolved properly and is partially blurry; b), two images from a telecentric lens system from *Opto Engineering Srl.* are used. On the left side, only the frontal profile of the tube is visible without any inner features due to the parallel ray beams. On the right side, the screw threads are resolved properly and can easily be tracked without any perspective distortions. Reprinted from [112] with permission of *Opto Engineering Srl.* 29

2.12 Side image taken from a bridge stretching measurement. In a) the image is shown before any post processing is performed. In b) the tracked contact angles and contour of the liquid bridge are used to display the contact angles and the best fitting curvature to the bridge contour. 31

2.13 Side view image of bridge stretching after pinch-off at both sides. In a) the ROI of a raw image is shown, in b) the four different labels for top, middle, bottom and background are apparent. 32

2.14 Top-view during finger formation of a *Gly80* during liquid bridge stretching. In a) the ROI of a raw image is shown in b) the tracked finger contour and effective radius R_{eff} are highlighted. 34

2.15 Top-view of finger formation of *Gly80* after pinch-off. In a) the ROI of a raw image is depicted and in b) the segmented finger pattern with its respective skeletonized structure is shown. Reprinted from [21] under CC BY 4.0. 35

3.1 Stretching of liquid bridges consisting of 5 μl of deionized water with an acceleration of 10 m/s^2 in the first row, 90 m/s^2 in the second row and 180 m/s^2 in the third row. Reprinted from [22] under CC BY 4.0. 38

3.2	Stretching of liquid bridges consisting of 5 μl of <i>Gly50</i> mixture with an acceleration of 10 m/s^2 in the first row, 90 m/s^2 in the second row and 180 m/s^2 in the third row. Reprinted from [22] under CC BY 4.0.	40
3.3	Evolution of the curvature and reciprocal height ratio for <i>Gly80</i> , $\lambda = 0.3$ and different accelerations. The data points are from the constant curvature section. Reprinted from [123] under CC BY 4.0.	42
3.4	Evolution of the liquid bridge curvature radius r_c during expansion. Showing a larger curvature radius at the beginning for t_1 an decreasing curvature radius due to necking for t_2 and increasing curvature radius as a result of the increasing vertical substrate distance for t_3 . This is only valid during the first phase of the liquid bridge stretching.	43
3.5	Evolution of the midpoint diameter comparing different viscosities and $\lambda = 0.09$ with an acceleration 180 m/s^2 in the lower curve array and for 10 m/s^2 in the upper curve array. Reprinted from [22] under CC BY 4.0.	44
3.6	Evolution of the midpoint diameter comparing non-dimensional initial bridge geometries $\lambda = 0.3$ in the lower curve array and for $\lambda = 0.09$ in the upper curve array for substrate accelerations 180 m/s^2 and different viscosities. Reprinted from [22] under CC BY 4.0.	45
3.7	Evolution of contact line diameter of <i>Gly80</i> comparing substrate accelerations 30, 60 and for 180 m/s^2 for $\lambda = 0.3$ in the upper curve array and $\lambda = 0.09$ in the lower curve array. Reprinted from [123] under CC BY 4.0.	46
3.8	Evolution of the contact line diameter to midpoint diameter ratio up to pinch-off of the liquid bridge. The measurements were performed with <i>Gly80</i> and 180 m/s^2 for different λ values. Adapted from [123] under CC BY 4.0.	48
3.9	Evolution of the midpoint diameter and the inverse height derived from mass continuity, see equation (3.2). Measurements were performed with <i>Gly80</i> , 180 m/s^2 for different parameters of λ . Adapted from [123] under CC BY 4.0.	49

List of Figures

3.10 Initial jet stretching. The diameter ratio as a function the height ratio H/H_0 for a substrate acceleration of $a = 180 \text{ m/s}^2$ and initial gap thickness $\lambda = 0.05$ for different viscosities. The experimental data are compared with the theoretical predictions from eq. 6.1. Adapted from [123] under CC BY 4.0. 50

3.11 Evolution of the diameter of a liquid bridge. The scaled bridge middle diameter D_M/D_0 as a function of the dimensionless gap width H/H_0 for various substrate accelerations. The curve corresponds to the predictions based on (3.4). Adapted from [21] under CC BY 4.0. 51

3.12 Top-view of the liquid bridge stretching shown pinned contact line, residual film, and moving inner meniscus. The measurement was performed with a dimensionless height of $\lambda = 0.0151$, with *Gly80* and an acceleration of 180 m/s^2 . 52

3.13 Sketch of the residual layer evolution at four time steps $t_1 < t_2 < t_3 \ll t_4$. The contact line stays pinned up to t_3 and starts move until t_4 . An apparent meniscus angle forms at the contracting residual layer. 53

3.14 Side view of meniscus deformation during liquid bridge stretching performed with telecentric optical system. The shown stretching measurement was performed with $\lambda = 0.0171$, *Gly80* and an acceleration of 180 m/s^2 54

3.15 Sequence of the bottom views of the liquid bridge. The time associated with the finger formation (approximately 10^{-1} milliseconds) is two order of magnitude smaller than the time at which the dewetting process becomes notable, at approximately 20 milliseconds. Contact angles for the hydrophobic substrates are $\theta \approx 110^\circ$ for *Gly50* and *Gly80*. Reprinted from [21] under CC BY 4.0. 55

3.16 Showing the contact line evolution of two dewetting measurements. Measurment with $\theta = 110^\circ$ was performed with $\lambda = 0.0164$ and for $\theta = 40^\circ$ with $\lambda = 0.0111$. Both times *Gly80* was used and the substrate acceleration was 180 m/s^2 . 56

3.17 Comparison of the evolution of the contact line diameter $D_U/D_{U,0}$ with circle markers on the left scale vs. meniscus angle θ with square markers on the right scale. The experiments were performed with *Gly80*, 180 m/s^2 and $\lambda = 0.18$. Reprinted from [123] under CC BY 4.0. 57

3.18	Comparison of the evolution of the contact line diameter $D_U/D_{U,0}$ with circle markers on the left scale vs. meniscus angle θ with square markers on the right scale. The experiments were performed with Gly80, 180 m/s ² and $\lambda = 0.09$. Reprinted from [123] under CC BY 4.0.	58
3.19	Evolution of meniscus angle of Gly80 comparing substrate accelerations 30, 60 and 180 m/s ² for $\lambda = 0.3$. The dashed line indicates the measured receding meniscus angle. Reprinted from [123] under CC BY 4.0.	59
3.20	Evolution of the capillary number $Ca_{CL} = U\mu\sigma^{-1}$ and the related meniscus angles. Measurements were performed with Gly80 and a dimensionless height $\lambda = 0.1$. Reprinted from [123] under CC BY 4.0.	60
3.21	A sketch of a liquid bridge from a side view and from top view at two different stages t_1, t_2 . A cylindrical frame of reference is used at the symmetry axis (r, z) . The relevant diameters for the following analysis are: D_U, D_M and the effective diameter D_{eff} . The top view is shown for t_1 at which the finger instability starts to form and t_2 with a pronounced finger pattern. A Cartesian frame of reference is used at the instability front at $t_1 (x, y)$. Adapted from [21] under CC BY 4.0.	61
4.1	Top view on emerging and disappearing cavitation due to bridge stretching. Experiments were performed with <i>Gly60</i> , $\lambda = 4.77 \times 10^{-3}$ on glass substrates and a constant stretching rate of 150 m/s ²	68
4.2	Top view on the cavitation events due to bridge stretching. Experiments were performed with <i>Gly80</i> , $\lambda = 4 \times 10^{-5}$ on glass substrates and a constant stretching rate of 150 m/s ²	69
4.3	Side view of measurement with pronounced cavitation. Back cutting of finger formation leads to separation of liquid bridges. Measurement was performed with <i>Gly80</i> , $\lambda = 4 \times 10^{-5}$ and $a = 180$ m/s ²	70
4.4	Top view on the cavitation due to the bridge stretching. Experimental measurements were performed with <i>Gly80</i> , $\lambda = 1.3 \times 10^{-4}$ on glass substrates and a constant stretching rate of 180 m/s ²	71

List of Figures

4.5	Predicted pressure evolution close to the substrate for the fluid <i>Gly80</i> with acceleration of 180 m/s^2 and different dimensionless heights of $\lambda = 0.025$ for no cavitation, $\lambda = 0.0012$ for transient cavitation and $\lambda = 0.0010$ with cavitation. The experimentally determined inception point is displayed in the form of a marker.	73
4.6	Predicted pressure evolution close to the substrate for the fluid <i>Gly50</i> with varying accelerations between $90\text{--}180 \text{ m/s}^2$ and different dimensionless heights $\lambda = 0.004$ for no cavitation, $\lambda = 0.004$ for transient cavitation and $\lambda = 0.001$ with cavitation. The experimentally determined inception point is displayed in the form of a marker.	75
4.7	Evolution of the largest bubble diameter with transient cavitation events are shown. The shown measurements were performed with different liquids <i>Gly50</i> and <i>Gly60</i> , different accelerations, 150 and 180 m/s^2 and with the same dimensionless height of $\lambda = 4.5 \times 10^{-4}$. The starting point of each bubble growth event is set to $t = 0 \text{ ms}$	76
4.8	Evolution of the largest bubble diameter with transient cavitation events are shown. The shown measurements were performed with the liquids <i>Gly50</i> and <i>Gly60</i> , accelerations 150 and 180 m/s^2 and with the same dimensionless height of $\lambda = 4.5 \times 10^{-4}$. Additionally, the bridge height over time is included as area plot for the substrate accelerations $150\text{--}180 \text{ m/s}^2$ and the mean extremum pressure time t_{p*} is shown.	77
4.9	Histogram of the bubble inception times of the transient cavitation events. Additionally a logarithmic distribution fit is added with a mean of $\mu = 1.29 \times 10^{-3}$ and standard deviation $s = 9.15 \times 10^{-4}$	78
4.10	Sketch of cylindrical bubble formation during an cavitation event.	80
4.11	Bubble growth of transient cavitation measurements. The dashed line show the ideal growth rate of a cylindrical bubble. Here $\tau_{b,\text{max}}$ is the experimentally determined dimensionless time instant of the maximum bubble diameter. $\tau_{b,\text{inc}}$ represents the measured dimensionless inception times of the beginning of the bubble growth phase.	82

5.1	Evolution of the diameter of a liquid bridge. Side views of a Gly80 bridge stretched with constant acceleration of 180 m/s^2 . The initial gap is $20 \mu\text{m}$ and the gap-to-diameter ratio is $\lambda = 0.02$. Reprinted from [21] under CC BY 4.0. .	86
5.2	Top view of the receding interface due to bridge stretching under various experimental conditions: a) liquid <i>Gly50</i> , substrate acceleration $a = 180 \text{ m/s}^2$, relative gap width $\lambda = 0.03$; b) <i>Gly50</i> , $a = 180 \text{ m/s}^2$, $\lambda = 0.006$; c) <i>Gly50</i> , $a = 10 \text{ m/s}^2$, $\lambda = 0.06$; d) <i>Gly80</i> , $a = 10 \text{ m/s}^2$, $\lambda = 0.03$. Contact angles are $\theta \approx 40^\circ$ for <i>Gly50</i> and <i>Gly80</i> on the glass substrate. Reprinted from [21] under CC BY 4.0. . .	87
5.3	Dimensionless amplitude of the radius perturbations $\ln(G/\delta_0)$ as a function of the dimensionless wave numbers ξ for various time instants τ , computed by numerical integration of (5.13). a) $Ca = 2.45, Re = 0.005, \lambda = 0.0059$, b) $Ca = 0.704, Re = 0.0026, \lambda = 0.0099$, c) $Ca = 0.0663, Re = 0.0252, \lambda = 0.0109$ and d) $Ca = 0.5109, Re = 0.034, \lambda = 0.0902$. Reprinted from [21] under CC BY 4.0.	93
5.4	The number of fingers N_f as a function of the liquid bridge radius R observed in three different experiments. The measurements were performed with $\lambda \approx 0.01$ and $Re \approx 0.1$. Reprinted from [21] under CC BY 4.0.	95
5.5	Scaled maximum number of the observed fingers $N_{\max}\lambda/Ca^{1/2}$ as a function of the Reynolds number. Reprinted from [21] under CC BY 4.0.	96
5.6	Computational results of $N_{\max}\lambda$ as a function of the capillary number Ca for various Reynolds numbers Re . Comparison with theoretical predictions based on the approximate solution. Reprinted from [21] under CC BY 4.0. . .	97
5.7	The values of the scaled pressure gradient at the meniscus interface $p_{0,r}/\Pi$ as a function of dimensionless time τ for various values of the Reynolds number Re . The scale for the pressure gradient, Π , is defined in (5.23). Reprinted from [21] under CC BY 4.0.	97

List of Figures

5.8	Comparison of the measured and theoretically predicted maximum number of fingers N_{\max} . The experiments accompanied by cavitation are marked by circles. The static contact angle of the measurements marked as diamonds, rectangles and circles is $\theta_{static} = 40^\circ$, while that of the measurements marked as triangle is $\approx \theta = 110^\circ$. The straight dashed line corresponds to perfect agreement between experiment and theory. Reprinted from [21] under CC BY 4.0.	99
5.9	Example of the void formation during liquid bridge stretching. The liquid is <i>Gly80</i> . The other experimental parameters are: $a = 180 \text{ m/s}^2$, $H_0 = 60 \mu\text{m}$, $\lambda = 0.006$. Reprinted from [21] under CC BY 4.0.	100
5.10	Example of the transient cavitation. Several voids are formed in the central part of the liquid bridge and then disappear. The liquid is <i>Gly80</i> . The other experimental parameters are: $a = 10 \text{ m/s}^2$, $H_0 = 53 \mu\text{m}$, $\lambda = 0.006$. Reprinted from [21] under CC BY 4.0.	100
5.11	Nomogram for the outcomes of liquid bridge stretching for various values of λ and capillary number Ca . The threshold for bridge finger formation is obtained from the full computations for $Re = 0$ of $\lambda_{\text{threshold}}$, corresponding to the condition $N_{\max} = 5$. The approximate solution (5.24) is also shown on the graph, but it is indistinguishable from the results of full computations for $Ca < 1$. Reprinted from [21] under CC BY 4.0.	101
6.1	Evolution of the value $1/R^2$ as a function of time t for various Reynolds numbers. In all the cases the values of the Weber numbers are high. The substrate acceleration is 180 m/s^2 . The liquids are <i>Gly10</i> , <i>Gly20</i> , <i>Gly40</i> , <i>Gly50</i> described in Table 2.2. Reprinted from [22] under CC BY 4.0.	110
6.2	Relation of the dimensionless term built on the basis of the jet radius, $1/\tilde{R}^2$ and dimensionless time \tilde{t} for various Reynolds numbers. Reprinted from [22] under CC BY 4.0.	110
6.3	Relation of the dimensionless term built on the basis of the jet radius, $1/\tilde{R}^2$ and dimensionless time \tilde{t} for various dimensionless gap widths λ . Reprinted from [22] under CC BY 4.0.	111

6.4	Liquid bridge pinch-off times in s as a function of acceleration in m/s^2 for deionised water 1 mPas, 50 % glycerol-water mixture 5 mPas and 80 % glycerol-water mixture 47 mPas with a dimensionless height of $\lambda = 0.2$. Reprinted from [22] under CC BY 4.0.	112
6.5	Liquid bridge pinch-off times in s as a function of acceleration in m/s^2 different dimensionless heights $\lambda 0.05$, $\lambda 0.15$ and $\lambda 0.25$ for deionised water. Reprinted from [22] under CC BY 4.0.	112
6.6	The scaled pinch-off time t_{br}/T_σ for different Re and dimensionless heights $0.05 < \lambda < 0.3$ in blue circles and from [96] for $0.5 < \lambda < 0.8$ in red squares. Reprinted from [22] under CC BY 4.0.	114

List of Tables

2.1	Experimentally determined contact angles on quartz glass, sapphire glass and polished aluminium substrates with their 95% confidence interval.	24
2.2	Evaluated liquid properties for $T = 15^\circ, T = 25^\circ$ and $T = 35^\circ$ according to the methods described in §2.1.2.	25